

学位論文

Evolution of ice giants in and outside the solar system
(太陽系および太陽系外における巨大氷惑星の進化)

平成27年12月博士（理学）申請

東京大学大学院理学系研究科

地球惑星科学専攻

黒崎 健二

December, 15, 2015

Contents

1	General Introduction	1
1.1	Interior structure of giant planet in our solar system	2
1.2	The evolution of close-in extrasolar planets	7
1.3	The atmospheric structure of giant planets	10
1.4	Purpose of this dissertation	12
2	Impact of the condensable composition in the atmosphere on the thermal evolution of ice giants	14
2.1	Introduction	14
2.2	Model description	18
2.2.1	Interior structure	19
2.2.2	Atmospheric structure	20
2.2.3	Thermal evolution	22
2.2.4	Abundance in atmosphere and interior	23
2.2.5	Opacities of hydrogen-helium	23
2.2.6	Opacities of H ₂ O, NH ₃ , and CH ₄	24
2.2.7	Equations of state	25
2.2.8	Condensation curves	32
2.3	Numerical procedure	33
2.4	Results	34
2.4.1	Atmospheric structure	35
2.4.2	Effect on the thermal evolution	36
2.5	Discussion	47

2.5.1	Validity of the assumptions I: the effect of the super-adiabatic lapse rate	48
2.5.2	Validity of the assumptions II: the effect of the cloud	50
2.5.3	Validity of the assumptions III: comparison to the today's atmospheric compositions	51
2.5.4	Validity of the assumptions IV: the continuity between the interior and atmosphere	51
2.5.5	Validity of the assumptions V: the model of the atmosphere	58
2.5.6	The evolution of Neptune	58
2.5.7	Implications for the origin of Uranus	59
2.6	Conclusions	63
3	Effect of photo-evaporative mass loss on masses and radii of ice giants	65
3.1	Introduction	65
3.2	Numerical models	68
3.2.1	Interior structure	68
3.2.2	Thermal evolution	70
3.2.3	Equation of state (EOS)	70
3.2.4	Atmospheric model	71
3.2.5	Mass loss	72
3.2.6	Transit radius	74
3.2.7	Numerical procedure	76
3.3	Mass evolution	78
3.3.1	Examples of mass evolution	78
3.3.2	Dependence on the initial planet's luminosity	79
3.3.3	Dependence on the initial water mass fraction	81
3.3.4	Dependence on the semi-major axis	85
3.3.5	Expected Populations	86
3.4	Implications for distributions of observed exoplanets	86
3.5	Summary	91
4	Conclusions	97

Acknowledgment	97
A Theory: Basic physics of the planetary interior structure and the thermal evolution	99
A.1 Interior structure for the polytropic model	99
A.2 The Virial theorem	102
A.3 The impact of the initial luminosity on the analytical thermal evolution of the planet	106
B Derivation of K_{tide}	110
C EOS data table	113
D Analytical formula for the chord optical depth of the isothermal plane-parallel atmosphere	116
E Analytical formula for the chord optical depth of the isothermal spheric symmetric atmosphere	119
F Atmospheric model for Chapter 3	121

Abstract

The aim of this dissertation is to evaluate the impacts of internal compositional distributions on the thermal evolution and the bulk composition's evolution of ice giants. This dissertation is composed of three parts. In chapter 1, general introduction of this dissertation is described. In chapter 2, the evolution of an ice giant in a long-period orbit is described. We deal with the thermal evolution of the ice giants in the solar system Uranus and Neptune and discuss their origins. In chapter 3, the evolution of an ice giant in a short-period orbit, namely water-rich sub/super-Earths, is described. We deal with the thermal and mass evolution of water-rich planets outside the solar system. We reveal the relationships among masses, radii, and semi-major axes of water-rich super-Earths and also sub-Earths that have undergone photo-evaporative mass loss. Through those two parts, we investigate the impact of condensation or evaporation of water on the evolution of ice giants in long-period, low-temperature or short-period, high-temperature environments.

Though Uranus and Neptune are similar in the mass and radius, the former is significantly fainter than the latter. As previous theoretical studies of thermal evolution of the ice giants demonstrated, the faintness of Uranus cannot be explained by simple three-layer models that are composed of a H/He-dominated envelope, an ice mantle and a rocky core. Namely, the observed effective temperature of Uranus is lower than theoretically predicted (e.g., Hubbard & MacFarlane 1980, Fortney et al., 2011; Nettelmann et al., 2013). Since the speed of the thermal evolution is determined by how efficiently the planetary atmosphere radiates energy, the evolution of the atmospheric structure is important. If the atmosphere contains ice materials such as water, ammonia and methane, those materials are condensed and removed from the atmosphere during the cooling. In this study, we quantify the impact of the condensation of ice components in the atmosphere on the thermal evolution to explain the current luminosity of Uranus. To do so, we simulate the thermal cooling of the ice giants, based on three layer models with a relatively ice-component-rich, H/He-dominated envelope on top of a water mantle that surrounds a rocky core. We demonstrate that the effect of the condensation makes the

timescale of the thermal cooling of the planet shorter by an order of magnitude than in the case without condensation. Such accelerated cooling is shown to be fast enough to explain the current faintness of Uranus. We also discuss the factors that would have caused the difference in current luminosity between Uranus and Neptune.

Recent progress in transit photometry opened a new window to the interior of ice giants. From measured radii and masses, we can infer constraints on planetary internal compositions. It has been recently revealed that ice giants orbiting close to host stars (i.e., hot super-Earths) are diverse in composition. This diversity is thought to arise from diversity in volatile content. The stability of the volatile components is to be examined, because hot super-Earths, which are exposed to strong irradiation, undergo photo-evaporative mass loss. While several studies investigated the impact of photo-evaporative mass loss on hydrogen-helium envelopes, there are few studies as to the impact on water-vapor envelopes, which we investigate in this study. To obtain theoretical prediction to future observations, we also investigate the relationships among masses, radii, and semi-major axes of water-rich super-Earths and also sub-Earths that have undergone photo-evaporative mass loss. We simulate the interior structure and evolution of highly-irradiated sub/super-Earths that consist of a rocky core surrounded by a water envelope, taking into account mass loss due to the stellar XUV-driven energy-limited hydrodynamic escape. We find that the photo-evaporative mass loss has a significant impact on the evolution of hot sub/super-Earths. With a widely-used empirical formula for XUV flux from typical G-stars and the heating efficiency of 0.1 for example, the planets of less than 3 Earth masses orbiting 0.03 AU have their water envelopes completely stripped off. We then derive the threshold planetary mass and radius below which the planet loses its water envelope completely as a function of the initial water content and find that there are minimums of the threshold mass and radius. We constrain the domain in the parameter space of planetary mass, radius, and the semi-major axis in which sub/super-Earths never retain water envelopes in 1-10 Gyr. This would provide an essential piece of information for understanding the origin of close-in, low-mass planets. The current uncertainties in stellar XUV flux and its heating efficiency, however, prevent us from deriving robust conclusions. Nevertheless, it seems to be a robust conclusion that Kepler planet candidates contain a significant number of rocky sub/super-Earths.

This dissertation investigates the impact of the distribution of condensable constituents on the thermal evolution and the bulk composition's evolution of the ice giants. Long-period ice giants experienced the thermal evolution and the condensation of water, ammonia, and methane in the atmosphere simultaneously. Short-period ice giants experienced the thermal evolution and mass loss simultaneously. Though the effects of condensation and mass loss remove the water or other volatiles from the atmosphere, those effects leave the trails on the evolution and observations of the ice giants. Those results will give essential insights to understand the relationship between origins and observations of planetary systems.

Chapter 1

General Introduction

Our solar system has four giant planets, Jupiter, Saturn, Uranus and Neptune. Jupiter and Saturn were found prehistorically, while Uranus and Neptune were found by Herschel and Watson (1781) and Le Verrier (1846), respectively. Giant planets are also discovered in extra-solar systems. Mayor and Queloz (1995) discovered the first Jupiter-mass object around a solar-type star. The planet, 51 Peg b, is the first discovered extra-solar planet (or exoplanet) around a main sequence star, while Struve (1952) indicated that exoplanets around the star could be found from the radial velocity of the host stars. Since the first exoplanet 51 Pegasi b was discovered in 1995 (Mayor and Queloz 1995), 1977 exoplanets have been found until today (exoplanet.eu, 2015/11/5). There are several observation methods for detecting exoplanets, the radial velocity measurement, transit measurement, astrometry, gravitational microlensing and direct imaging. Given the measured masses and radii, we can infer the internal bulk compositions of the exoplanets, which give crucial constraints to their origins. Indeed, we have gained deep insight into the origin of the solar-system giant planets from the knowledge of the interior structure of the planets.

The planetary structure is composed of mainly two parts, the interior structure and the atmospheric structure. The interior structure is related to the bulk composition of the planet that is closely related to the evolution and origin of the planet. In § 1.1, the theory of the giant planets in our solar system is described. The basic theory of interior structures of Uranus and Neptune is common with that of Jupiter and Saturn (hereafter the gas giants). The basic theory of interior structure is applied to the exoplanets. Since those planets are located in close to the host (hereafter close-in exoplanets), they are in

high-temperature and strong X-ray and extra ultra-violet (hereafter XUV) environment. In § 1.2, studies of mass loss and thermal evolution of close-in exoplanets are described. To understand the planetary structure, the atmospheric structure is also important. The interior structure of the planet can not be observed directly, while the atmospheric compositions and temperature structures can be observe. Since atmospheres of gas giants and ice giants are connected to their own interior continuously, understanding the atmospheric structure is essential to understand the entire structure and evolution of the planet. In § 1.3, studies of the atmospheric structure of water-rich planet are described. Lastly, we summarize the aim of this dissertation in § 1.4.

1.1 Interior structure of giant planet in our solar system

The giant planets account for 99.5 % of the total mass of the planets and the other small bodies in our solar system (Stevenson, 1982). If we want to discuss the formation of the solar system, it is important to understand where and when the giant planets were formed. To understand the origins of giant planets, it is essential to know what giant planets are mainly composed of and what are the ages of giant planets. For understanding the compositions and evolutions of giant planets, it is important to investigate the planetary interior structure. The main topic in this dissertation is ice giants. However, the theory of the interior structure has been improved by studies on Jupiter and Saturn. That is, to understand the interior structure of ice giants, it is necessary to understand that of gas giants.

The interior structure of the giant planets in the solar system has been investigated by many authors since the twentieth century. Zapolsky and Salpeter (1969) was a pioneer in studying the relation between the planetary mass M_p and the planetary radius R_p . The planetary mass-radius relationship is important to discuss the bulk composition. In their study, equations of state were assumed to be simple ones that were derived from the Thomas-Ferimi-Dirac equations by Salpeter and Zapolsky (1967). They simulated the structure of spherically symmetric planets in hydrostatic equilibrium and uniform in composition. They found that there is the maximum radius of a planet with a given

uniform composition. That is because the dominant force that governs the structure differs depending on the planetary mass: For relatively low-mass planets, the gravitational force is small compared with the electrostatic solid state force such as the Colomb force, which means that the material is not compressed enough to increase the density ρ , so that $R_p \propto M_p^{1/3}$. In contrast, for higher-mass planets, the electrons are free because pressure ionization and the electrostatic forces are small compared with the Fermi pressure and with gravitational force, namely, the material is compressed by the gravitational force, so that $R_p \propto M_p^{-1/3}$. The mass at the maximum radius depends on the planetary composition and its equation of state. Thus the planetary mass-radius relationship can never be predicted without considering the property of materials. They also found that Jupiter and Saturn were composed mainly of hydrogen and helium, and estimated the mass fraction of hydrogen X to be 0.82 for Jupiter and 0.73 for Saturn. According to their modeling, Uranus and Neptune were not mainly composed of hydrogen and helium due to their large mean density compared to Jupiter and Saturn. That is, Uranus and Neptune could possess more heavy elements than Jupiter and Saturn. Those heavy elements are included in the form of cores. Podolak and Cameron (1974) simulated the planetary interior structure considering a central core composed of heavy elements and showed that the interior of Jupiter and Saturn was not uniform in composition and likely had more than $10M_{\oplus}$ heavy element cores.

The thermal evolution of Jupiter was studied by Grossman et al. (1972) and Graboske et al. (1975). Grossman et al. (1972) calculated the evolution of a stellar object of mass $0.001M_{\odot}$ (\sim Jupiter mass) composed of pure hydrogen to ascertain whether a gravitational contraction model for substellar mass objects was applicable to gas giant planets. Then, they concluded that the qualitative behavior agreed with the standard stellar evolutionary picture; gas giants behave like pre-main-sequence low-mass stars, and then rapidly goes over to a configuration like a white dwarf which indicate that the planetary radius slightly decreases and the planetary luminosity decreases. They also indicated that it was reasonable for the interior of gas giants to be approximated by adiabatic fluid models. The turbulent motion transports enormous flux of energy in a very compressible gas, which is stratified in density, pressure, temperature and gravity over many powers of ten. Böhm-Vitense (1958) described the convective transport of

energy as an exchange of energy between hotter and cooler layers in a dynamically unstable region through the exchange of macroscopic mass elements, which is so-called the mixing-length theory and is widely used to describe the thermal transport in the stellar interior (Kippenhahn and Weigert, 1990). Gough and Weiss (1976) discussed the stellar evolution using the mixing-length theory for a convective envelope and showed that the temperature structure of the convective envelope was able to be described by the adiabatic lapse rate. That is, if we want to calculate the temperature structure of convective zone, that can be described by the adiabatic lapse rate. This approximation is widely used in the thermal evolution of the planet (e.g. Graboske et al. (1975); Guillot et al. (1995)). Namely, the dominant equations for gas giants are the same as stars without hydrogen burnings and the luminosity of gas giants can be explained by the released energy due to the gravitational contraction of the planet that has adiabatic interior structure.

Hubbard (1977) studied the cooling of Jupiter, assuming that Jupiter had fully convective interior and lost its primordial heat which had been reserved in the convective interior since Jupiter had formed. That cooling model was based on the energy balance equation, namely, the planet's interior heat was lost by the planet's luminosity. The planet's interior temperature structure is determined by its interior heat. Given that the planet's interior is fully adiabatic, the planet's temperature structure can be determined by the planet's entropy which is determined by the planetary atmospheric condition. When the planet loses its interior heat via its luminosity, the planet's entropy decreases. He found that the Jovian total cooling time derived by that model was in good agreement with the age of the solar system. Note that he assumed Jovian interior was chemically homogeneous and its interior structure had not changed throughout the evolution. Graboske et al. (1975) used the accurate thermodynamic properties for hydrogen and helium, while Hubbard (1977) used that for only metallic hydrogen and ignored the molecular hydrogen. The discrepancy between Graboske et al. (1975) and Hubbard (1977) is due to the treatment of thermodynamic properties. Thus, it is important for the gas giant's thermal evolution to evaluate the planet's entropy correctly.

The internal compositional distribution of gas giants has a significant effect on the planetary evolution as follows. While the Jovian thermal evolution could be explained by the cooling model that assumes the interior is chemically homogeneous, that is not

the case with Saturn. Pollack et al. (1977) calculated the gravitational contraction of a homogeneous interior model for Saturn and found that Saturn emitted more energy in addition to the loss of primordial heat. A possible mechanism is heat output due to the downward migration of helium in the metallic-hydrogen region, which was supported by the observed depletion of helium in Saturn's atmosphere (Hanel et al., 1981). A study about the Saturnian evolution, considering chemically inhomogeneous interior structure (that is, the composition and the entropy change as a function of the radius of a mass shell inside the planet), was recently done by Fortney and Hubbard (2003). They demonstrated that provided helium was free to migrate down to the planet's core, the released potential energy was large enough to extend the Saturn's cooling time so as to match the age of the solar system. Another explanation for the Saturn's luminosity is that the delay in evolution is due to the chemically inhomogeneous interior structure, the effect of which may be important for other giant planets such as Jupiter, Uranus, Neptune and exoplanets. The chemically inhomogeneous interior provides a compositional gradient which affects the efficiency of thermal transport via convection. Leconte and Chabrier (2013) calculated the thermal evolution of Saturn considering the layered convection generated by compositional gradients. The layered convection is a structure of convection which is consisted of uniformly mixed convective layers separated by thin diffusive interfaces characterized by a steep jump in the mean molecular weight. The layered convection has a great impact on the thermal transport by convection and changes the thermal evolution timescale of the planet. They found that the layered convection could explain the Saturn's present luminosity without any additional energy source, such as helium sedimentation described above. Though there are uncertainties for mechanisms maintaining the compositional gradient structure, evolution of layers, and the number of layers (Nettelmann et al., 2015; Vazan et al., 2015; Kurokawa and Inutsuka, 2015), that effect should be important for other giant planets such as Uranus, Neptune and exoplanets.

Here we summarize understanding of the thermal evolution derived by studies of gas giants. The thermal evolution of gas giants can be described by a simple model of gravitational contraction with fully convective interior structure.

Since the ice giants Uranus and Neptune have hydrogen-helium envelopes, they should

have been formed before the protoplanetary disk disappeared. Observations suggest that the lifetime of a protoplanetary disk is on the order of ≤ 10 Myr (e.g. Haisch et al. (2001); Hernández et al. (2007)). If we assume that the initial luminosity L_{init} of an ice giant was equivalent to the gravitational energy due to the accretion of planetesimals, we can estimate the accretion timescale τ_{acc} (Podolak et al., 1991). We can write the gravitational energy as $\frac{GM_p}{R_p}$ and the accretion rate as $\frac{dM}{dt} \simeq \frac{M_p}{\tau_{\text{acc}}}$, where M_p is the planetary mass, R_p is the planetary radius, $G(= 6.67 \times 10^{-8} \text{ dyn cm}^2 \text{ g}^{-2})$ is the gravitational constant. We can estimate $L_{\text{init}} = \frac{GM_p}{R_p} \frac{M_p}{\tau_{\text{acc}}}$ and then we can rewrite

$$\tau_{\text{acc}} = \frac{GM_p^2}{R_p L_{\text{init}}}. \quad (1.1)$$

Then we can derive the initial luminosity as follows (Podolak et al., 1991),

$$L_{\text{init}} = 6 \times 10^{26} \left(\frac{M_p}{M_U} \right)^2 \left(\frac{R_p}{R_U} \right)^{-1} \left(\frac{\tau_{\text{acc}}}{100 \text{ Myr}} \right)^{-1} \text{ erg s}^{-1}, \quad (1.2)$$

where M_U is the mass of Uranus ($= 8.68 \times 10^{28} \text{ g}$), R_U is the radius of Uranus ($= 2.56 \times 10^9 \text{ cm}$). We can find that L_{init} is greater than the present luminosities of Uranus ($= 3.4 \pm 3.8 \times 10^{21} \text{ erg s}^{-1}$) and Neptune ($= 3.3 \pm 0.35 \times 10^{22} \text{ erg s}^{-1}$) by several orders of magnitude (Pearl and Conrath, 1991).

Uranus and Neptune contain more heavy elements than Jupiter and Saturn (e.g. Hubbard and Macfarlane (1980)), as mentioned above. Their constituents are thought to be ice components such as water, methane and ammonia (e.g. Stevenson (1982)). Although Uranus and Neptune are similar in mass and radius, Uranus is observationally known to be less luminous than Neptune (e.g. Podolak et al. (1991); Hubbard et al. (1995)). Pioneering works for thermal evolutions of Uranus and Neptune were done by Hubbard (1978) and Hubbard and Macfarlane (1980). Hubbard (1978) simulated the thermal evolution of Uranus and Neptune by a simple model that is a scaled model of Jupiter, while Hubbard and Macfarlane (1980) did so by assuming three layered model and using equation of states for hydrogen-helium, ice, and rock composition. Hubbard and Macfarlane (1980) concluded that initial temperatures and luminosities for Uranus and Neptune were not substantially higher than the present values, though Hubbard

(1978) concluded that thermal emissions of Uranus and Neptune are consistent with recent infrared observations when the initial luminosities were substantially higher than the present values. That is because the heat capacity for ice compositions that Hubbard (1978) adopted was underestimated compared to what Hubbard and Macfarlane (1980) adopted. The initial planetary luminosity that pioneering studies predicted were too faint to maintain the consistency with the formation scenario (Podolak et al., 1991) and the state-of-the-art heat capacity and equation of state were essential to evaluate the thermal evolution timescale.

Fortney et al. (2011) recently investigated the thermal evolution, taking into account the radiative-convective atmosphere grid models to determine the upper boundary conditions for the interior structure. They found that planets had longer cooling times compared to the previous works, because of higher atmospheric opacities. Moreover, to the equation of state of water developed from the quantum molecular dynamics simulations (French et al., 2009), their Neptune model matched the observed effective temperature and planet’s gravitational field constraints. However, Uranus was far cooler than their calculations predicted. That is, if we construct the formation scenario of ice giants, the initial luminosity of Neptune was high due to the accretion energy, while that of Uranus was low if the initial luminosities were the same values. Hence, evolutionary models that previous studies showed cannot explain the difference of the present luminosities of Uranus and Neptune as long as each initial luminosity was assumed to be different. However, to be consistent with the formation scenario, the initial luminosity of Uranus and Neptune was high enough to explain that their formation timescale (e.g. Bodenheimer and Pollack (1986); Podolak et al. (1991); Pollack et al. (1996)). Therefore, we investigate the thermal evolution process of Uranus whose initial luminosity was high.

1.2 The evolution of close-in extrasolar planets

Because of capability limitations in observational techniques, available data concerning exoplanets are only orbital period, planetary mass, radius and so on. From measured mass and radius, we can obtain the mean density of an exoplanet. The mean density is related to the planet’s composition, which provides an important constraint to the

planet's origin.

Compositions of exoplanets are inferred by comparing observational and theoretical mass-radius relationships of exoplanets. The theoretical mass-radius relationships were derived by many authors. Most of the exoplanets that we know currently are close to their host star, their semi-major axes being typically $\lesssim 0.1\text{AU}$. Although previous models of exoplanet's structure are based on the knowledge of the solar system (e.g. Stevenson (1982); Hubbard and Macfarlane (1980); Fortney et al. (2011)), the environment of exoplanets should be rather different from those of our solar system planets, because effects of tidal heating and irradiation from the host star are important for these close-in exoplanets.

As mentioned above, recent progress in observation techniques has enabled us to find exoplanets with relatively small masses and/or radii compared to hot-Jupiters. These small exoplanets are called hot-Neptunes or super-Earths. The mass-radius relationships for solid planets were derived by Sotin et al. (2007), Seager et al. (2007), Grasset et al. (2009), and Valencia et al. (2010). These models are based on the knowledge as to the terrestrial planets in our solar system. If only the planetary mass and radius are available, we are unable to determine the planet's composition uniquely. Moreover, Adams et al. (2008) examined the influence of the hydrogen-helium envelope on the planetary radius and demonstrated that adding a gas envelope equivalent to 0.1-10% of the mass of a solid planet causes its radius to increase by 5-60% from its gas-free value.

To remove such degeneracy in composition, we may make use of constraints from planetary evolution. Since close-in planets are strongly irradiated by host stars, these planets are exposed to strong X-ray and ultraviolet (hereafter XUV). Because of that, close-in planets possibly experienced atmospheric escape. Indeed, Vidal-Madjar et al. (2003) observed the evaporating atmosphere of the hot-Jupiter HD209458 b. Atmospheric escape can also occur for close-in super-Earths. Lammer et al. (2013) calculated the hydrodynamic escape for close-in super-Earths. They found that super-Earths experienced the hydrodynamic escape.

To survey the composition and origin of close-in exoplanets, the thermal evolution and mass loss are important. Valencia et al. (2010) studied the interior structure and mass loss of the super-Earth CoRoT-7b. They found that CoRoT-7 b could not posses

massive hydrogen-helium envelope because of the intense irradiation and its small size. A similar study for the Kepler-11 five-super-Earth system was done by Lopez et al. (2012) and they discussed compositions of Kepler-11 b-f and their origin. That is, the amount of hydrogen-helium envelope of CoRoT-7b and Kepler-11 planets were restricted by the mass loss and the mass loss plays an important role in determining close-in planets' compositions.

Mass loss has a significant impact on the distribution for the mass-semimajor axis or radius-semimajor axis of close-in exoplanets (Owen and Wu, 2013; Lopez and Fortney, 2013; Kurokawa and Nakamoto, 2014). They calculated the mass loss evolution of short-period planets composed of a rocky core surrounded by a hydrogen-helium envelope and found that the mass loss evolution could explain the observed correlation between the separation and mass (radius, density) of the planets detected until the paper was published. They concluded that the mass loss of a planet changes its bulk composition from its birth. That is, the observed mass and radius of a planet can not be connected to the formation scenario without considering the evolution after the planet was formed. To discuss the thermal evolution and the mass loss is essential for understanding the planet when it was formed. If we consider the mass loss as an energy-limited hydrodynamic escape, the mass loss rate \dot{M} is a function of the planetary mean density (see Chap. 3 for more detail). Since the planetary mean density infers the planetary bulk composition, to understand the impact of mass loss on the planetary mass and radius is important for understanding the origin and evolution of the planet. Hence, we investigate the stability of the envelope of the close-in ice giant against photo-evaporation. If we want to estimate the mass loss rate, we have to estimate the planetary mean density. Since the planetary mean density changes by the age, to estimate the entropy of the planet is also important, which is related to the time evolution. The entropy of the planet is determined by the atmospheric structure. Therefore, understanding of atmospheric structure of ice giants is essential.

1.3 The atmospheric structure of giant planets

When emission and transmission spectra from a planet are observed, those include information of the atmospheric structure and composition. The atmospheric structure of a giant planet controls the thermal emission from the interior, which is essential to estimate the cooling timescale and to compare the observation of atmospheric composition and the present thermal emission. That is, the atmospheric structure is important for both of the planetary evolution and observation of the planet, which is essential to characterize the planet. Giant planets' atmospheres are mainly composed of hydrogen and helium.

The atmospheric structure is essential to determine the entropy of the planet. Since the radiative-convective boundary and the outward flux from the planet is determined by the atmospheric structure, the atmospheric structure could constrain the timescale the thermal evolution. Moreover, if the planetary atmosphere is not mainly composed of hydrogen molecules, the atmospheric structure would be changed.

The atmospheric structure is composed of a radiative region atop a convective region. If the planetary entropy is determined by the condition of the bottom of the atmosphere, the net flux through the atmosphere is determined by the atmospheric structure. The main constituents of the present ice giants' atmospheres is hydrogen and helium. However, the ice giants' atmospheres when it was formed may have been composed of mainly volatiles which include hydrogen, helium, water, ammonia, methane, carbon monoxide and other constituents that are in gas phase. Moreover, the atmosphere of close-in water-rich super-Earths is mainly composed of water molecule. To understand the structure that composed mainly of water, the Earth's atmospheric structure is a good reference. That is, to understand the atmospheric structure of terrestrial planets is useful to understand that of ice giants whose atmospheres are mainly composed of condensable constituents which indicate water, ammonia, and methane. In this study, we indicate condensable constituents are water, ammonia, and methane.

The atmosphere of the terrestrial planets, especially Earth, is controlled by the behavior of water molecules. If the water is condensed in the atmosphere, the latent heat warms up the surroundings and the temperature gradient changes. The saturation vapor pressure has a dominant effect on the temperature-pressure relation in the atmosphere.

The outward flux from the top of the atmosphere is fixed as long as the water in the atmosphere is condensed around the photosphere where the optical thickness of infrared radiation is on the order of unity (e.g. Ingersoll (1969); Komabayasi (1967); Nakajima et al. (1992)). Abe and Matsui (1988) studied the atmospheric properties of the impact-generated atmosphere composed of H₂O and CO₂. The amount of the atmosphere is more than 200 bars and the optical thickness is larger than unity. They found that the surface temperature decreases due to the cooling of the planet when the energy flux is less than $1.50 \times 10^5 \text{ erg s}^{-1} \text{ cm}^{-2}$ ($= 150 \text{ W m}^{-2}$). This energy flux is quite large, comparing to the present luminosity of Uranus. If we assume the planetary radius is equal to the present radius of Uranus R_U , the planetary luminosity is $L_p = 4\pi R_U^2 F = 1.2 \times 10^{25} \text{ erg s}^{-1}$ which means that the Kelvin-Helmholtz timescale, which describes the timescale of the contraction of the planet, is $\tau_{\text{KH}} = \frac{GM_U^2}{2R_U L_p} \sim 3 \times 10^8 \text{ year}$.

The present atmospheric structure of the ice giants is summarized here. Observations by Earth-based and Earth-orbital telescopes, and Voyager 2 spacecraft suggest that the atmosphere of Uranus is enriched in heavy elements relative to solar composition. The atmosphere is mainly composed of hydrogen, helium, methane, and hazes composed of hydrocarbons. Observations also suggest that the helium mole fraction is $15.2 \pm 3.3 \%$ (0.262 ± 0.048 by mass fraction), which, within the uncertainties, is the same as the value of the primitive solar nebula (0.27-0.28 by mass) derived from standard evolutionary model of the Sun (Fegley et al. (1991) and references therein). The atmosphere of Neptune is composed of hydrogen, helium, methane, HCN, CO, and hydrocarbons (e.g. C₂H₆, C₂H₂). (Bishop et al. (1995) and references therein) The atmospheric temperature structure of Uranus is calculated by Marley and McKay (1999). They found that internal heat fluxes $\leq 60 \text{ erg cm}^{-2} \text{ s}^{-1}$ were inconsistent with the observed tropospheric temperature profile. The internal flux was about $80 \text{ erg cm}^{-2} \text{ s}^{-1}$, which was derived from the best-fitting model throughout the troposphere.

There is the hint for discussing what determines the timescale of the thermal evolution. The ice giants have potentially a lot of condensable constituents in their interior. If mole fractions of volatiles in the atmosphere are fixed at the present values, volatiles in the atmosphere were not be saturated through the planetary evolution. When the planetary atmosphere were mainly composed of condensable constituents, excess volatiles

in the atmosphere were removed due to the condensation. However, excess condensable constituents warm the atmosphere due to the latent heat, which in turn have an influence on the thermal evolution history of the planet. Therefore, mole fractions of volatiles when the planet formed are important issue to understand the origin and evolution of ice giants.

1.4 Purpose of this dissertation

Through this dissertation, we investigate the evolution of the ice giants in the solar system and beyond. In our solar system, the present luminosity of Uranus is too faint to explain if it was formed within the age of our solar system as described above in § 1.1. Constraining the evolutionary pass of Uranus is important to understand the formation scenario of our solar system. Outside our solar system, many close-in ice giants have been discovered. Since those ice giants are in high-temperature and strong X-ray and extreme UV environments, they experience the atmospheric escape and decrease their mass. The amount of condensable constituents that the planet possesses would be useful to constrain when and where the planet was formed. The evolution and bulk composition of ice giants are clues to connect the formation history and the planetary system. However, no systematic study is yet to be done for the stability of water envelopes.

The rest of this dissertation is composed of two parts. In chapter 2, the impact of the condensable constituents in the atmosphere on the thermal evolution of ice giants is investigated. We deal with the thermal evolution of cold ice giants in the solar system and discuss the origins of Uranus and Neptune. In chapter 3, the impact of photo-evaporative mass loss on masses and radii of water-rich sub/super-Earths is examined. Considering the thermal and mass evolution of ice giants outside the solar system, we investigate the relationships among the masses, radii, and semi-major axes of water-rich super-Earths and also sub-Earths that have undergone photo-evaporative mass loss. Through those two parts, we reveal the role of volatiles on the evolution of ice giants in long-period, low-temperature or short-period, high-temperature environments. Though some key volatile constituents cannot currently be detected directly by observations of atmospheres of ice giants in the solar system and beyond, they would act as tracers for constraining the origin and evolution of ice giants due to differences in their evolution history. If we can

determine those tracers, they would provide us useful information to reveal the origin of the planetary system.

Chapter 2

Impact of the condensable composition in the atmosphere on the thermal evolution of ice giants

2.1 Introduction

The interior structure of Uranus is thought to consist of three layers, a rocky core, an ice mantle and a hydrogen/helium-dominated envelope from inside out (e.g. Hubbard and Macfarlane (1980); Stevenson (1982); Fortney et al. (2011)). Observation done by Voyage 2 determined the effective temperature of Uranus to be 59.3 ± 0.8 K, which corresponded to the intrinsic luminosity of less than 7×10^{22} erg s⁻¹ (Pearl and Conrath, 1991). Previous studies (e.g. Hubbard and Macfarlane (1980); Fortney et al. (2011)) predicted the initial effective temperature $T_{\text{eff}} \sim 65\text{-}70$ K. However, such a low initial luminosity means that the formation timescale is longer than the age of solar system (Podolak et al., 1991). Thus, it is essential to understand the evolutionary track from a high luminosity state of Uranus that is consistent with the formation theory.

Here we show typical examples of a evolutionary track of planetary luminosity assuming low initial luminosities. Fig. 2.1 shows the time evolution of the ice giants for various initial luminosities. The initial luminosity is related to the accretion timescale (see Eq. (1.2) or Podolak et al. (1991)). Lines' colors represent the accretion timescales. We can find that if we assume the long accretion timescale, which means the low initial

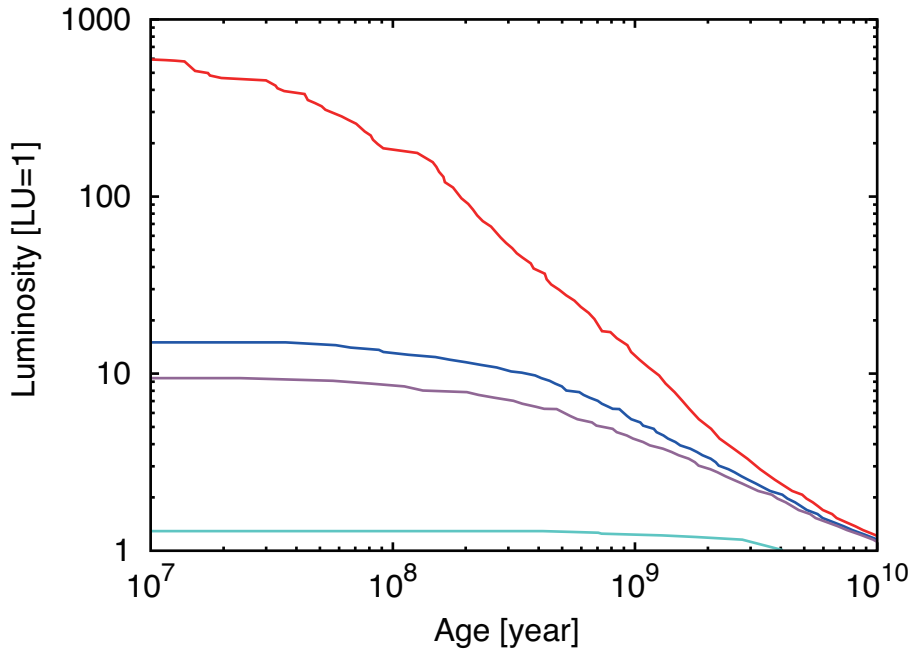


Figure 2.1: The time evolution of planetary luminosity with various initial luminosity. The luminosity and age are normalized by the present luminosity of Uranus $LU = 5.6 \times 10^{22} \text{ erg s}^{-1}$ and year, respectively. Lines' colors represent the initial luminosity. The red, blue, purple, and aqua blue represent $\tau_{\text{acc}} = 200 \text{ Myr}$, 4.6 Gyr, 13 Gyr, 500 Gyr, respectively. We assume $Z_0 = 0.3$, $Z_{\text{tot}} = 0.8$, and $Z_w = 0.5$, respectively. The condensation of ice compositions (water, ammonia, and methane) are ignored. See § 2.2 for the detail model description.

luminosity, the present luminosity of Uranus can be explained. However, to satisfy such the low initial luminosity, the accretion timescale is required to be longer than the age of our solar system. If we assume $\tau_{\text{acc}} < 10 \text{ Gyr}$, which is equivalent to the age of the universe, the difference among initial luminosities is eased after 5 Gyr.

The initial state of thermal evolution of Uranus is equivalent to the final state of formation. To understand the initial luminosity of Uranus, knowledge of formation theories are essential. The formation stage is divided by five parts (e.g. Bodenheimer and Pollack (1986); Pollack et al. (1996); Ikoma et al. (2000)). Below we review the formation processes of gas giants. (a) A core composed of the condensable constituents (rocky, water, ammonia, and other species) is formed due to the accretion of planetesimals. (2) When the core mass has grown to the one from a few tenth of an Earth mass, a gaseous envelope in hydrostatic equilibrium begins to form around the core. (b) The core whose mass is the one from a few ten Earth masses obtain a gaseous envelope in hydrostatic equilibrium.

(c) The core and envelope continue to grow until the crossover mass is reached. (d) When the core mass is reached the crossover mass, the envelope mass increases rapidly. This is so-called runaway accretion. At the same time, the planet produced a high luminosity which is caused by the gravitational contraction of the envelope. (e) Accretion of both core and envelope halts, and the planet contracts and cools. The thermal evolution of the planet is process (e). The initial condition of the thermal evolution is determined by process (d). However, the formation of ice giants does not follow the runaway accretion, namely process (d). Pollack et al. (1996) calculated the formation of Uranus and Neptune. They concluded that Neptune and Uranus contain 1–4 Earth mass of hydrogen-helium envelope with the remaining 10–16 Earth mass core. Thus, the accretion of hydrogen-helium envelope was halted before the runaway accretion occurred. They also found that the minimum luminosity during the formation phase was about 3×10^{26} erg s⁻¹ that was equivalent to $\tau_{\text{acc}} \sim 200$ Myr derived by Eq. (1.2). If we calculate the thermal evolution of Uranus from the high initial luminosity state, we can not explain the present luminosity of Uranus as shown above.

The thermal evolution of an ice giant has been described as a homogeneous evolution, which means the planetary interior is fully adiabatic and consisted of a compositionally homogeneous structure (Hubbard and Macfarlane, 1980; Fortney et al., 2011; Nettelmann et al., 2013). The luminosity of the ice giant decreases with time through the thermal emission from the planetary atmosphere. Hubbard and Macfarlane (1980) calculated the thermal evolution of Uranus and Neptune. They concluded that Uranus and Neptune did not have substantially high temperature interior and high luminosities when they were formed. Fortney et al. (2011) calculated the thermal evolution of Uranus and Neptune with the state-of-the-art equations of state and atmospheric model. They found that Neptune matched the measured effective temperature of the planet with the homogeneous model that also matched the current gravity field constraints of the planet. However they found that the present luminosity of Uranus was underluminous comparing to the numerical results.

The previous studies have proposed three ideas to solve that problem. The concept of the following ideas is that the primordial heat is reserved in the deep interior. One idea is that the super-ionic water layer is formed in the deep interior, which prevents the

transport of the heat from the deep interior. However, such a layer is formed too deep to reserve enough primordial heat within the deep interior (Nellis et al., 1988; Podolak et al., 1991). The second idea is that giant impact events deposited the impact energy into the thin shell to inhibit convection. The interior structure of proto-Uranus would be compositionally stably stratified. When proto-Uranus experienced a giant impact, the upper layer was heated and the impact energy was deposited. However, the crucial issue is how to partition the impact energy. To distribute the input energy into the thin outer shell of Uranus, it would require strict impact parameters. The last idea is that semi-convection or double diffusive convection prevents convective transport of heat in the planetary interior (Podolak et al., 1991). Uranus might have a thermodynamically stable interior that prevents convection due to compositional gradients. In this case, even when the outer envelope cooled, the deep interior did not cool efficiently (Stevenson, 1986; Nettelmann et al., 2013). The convection with compositional gradients, which is called semi-convection or double diffusive convection, is important to discuss the transport of the heat and constituents by convection in the deep interior. The transport property depends on the form of convection. In especially, the layer convection, which is separated by diffusive interface, prevents the thermal transport and delays the cooling (Radko, 2003; Rosenblum et al., 2011; Mirouh et al., 2012; Wood et al., 2013). The transport property of the layered convection depends on the layer thickness. It is still unclear whether there is an equilibrium layer thickness. The impact of the layered convection on the thermal evolution was examined for the cases of gas giants (Vazan et al., 2015; Kurokawa and Inutsuka, 2015; Nettelmann et al., 2015). However, the layered convection is hydrodynamically unstable for the large-scale-overturning convection. Efficient mixing due to the overturning convection may smooth out the compositional inhomogeneity in the planetary interior (Vazan et al., 2015; Kurokawa and Inutsuka, 2015). If the compositional inhomogeneity disappears, the planetary interior should be compositional homogeneity and the convective transport of heat is not prevented. Hence, this thesis propose another hypothesis to solve the thermal evolution of Uranus.

We assume that Uranus possessed a significant amount of condensable constituents in the atmosphere when it was formed. If ice materials are condensed, the lapse rate in the convective region of atmosphere is changed. The atmospheric temperature is raised due

to the latent heat of condensation compared to a dry adiabatic condition. In this study, we demonstrate the acceleration of cooling due to the condensation in the atmosphere when we assume a significant amount of condensable constituents.

In this study, we aim to find a self-consistent evolutionary track of Uranus whose initial condition is consistent with a core accretion scenario. We also discuss the factors that determine the difference between Uranus and Neptune in the present luminosity. Our study will be useful to discuss the consistency between the formation scenario and the observations of the ice giants.

The rest of this chapter is organized as follows. The basic equations and assumptions in this study adopted are described in § 2.2. The results of our calculations are described in § 2.4. The discussion of our study are described in § 2.5. Finally, the conclusions are described in § 2.5.

2.2 Model description

In this study, we simulate the evolution of the luminosity and radius of a planet that consists of hydrogen-helium, ice constituents (water, ammonia, and methane) and rock, including the effects of condensation in the atmosphere. The structure model is depicted in Fig. 2.2. The planet is assumed to consist of four layers in spherical symmetry and hydrostatic equilibrium; namely, from top to bottom, a hydrogen-helium-dominated atmosphere with water, ammonia, and methane, a hydrogen-helium-dominated envelope with water, a water mantle and a rocky core. At each interface, the pressure and temperature are continuous. We summarize the picture of the evolution of the ice giant as follows. With the thermal evolution, the atmosphere cools and the water, ammonia, and methane (hereafter we call condensable constituents) condenses. Then the atmospheric temperature structure can be affected by the latent heat due to the condensation of condensable constituents. We set the parameters the mole fraction of condensable constituents and its fraction of constituents. We investigate the effect of those parameters on the thermal evolution of the ice giants.

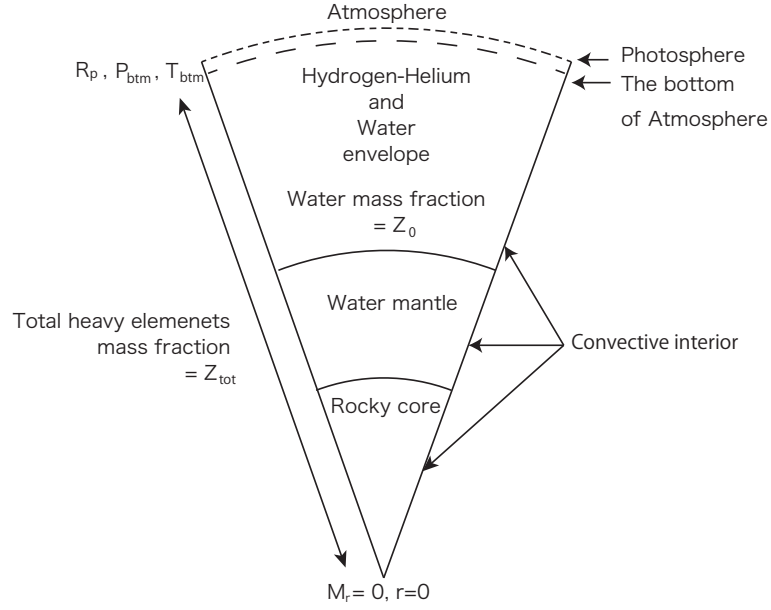


Figure 2.2: Model of the planetary structure in this study.

2.2.1 Interior structure

The assumptions for the interior structure are shown here.

- The planet has non-rotating, spherically symmetric, hydrostatic-equilibrium structure.
- The interior is three-layer structure that consists of a rocky core, a water mantle, and a hydrogen-helium-dominated envelope with water from inside out.
- The envelope, the water mantle, and the rocky core are fully convective and the convection is vigorous enough that the entropy S is constant in each layer.

The interior structure of the planet is determined by the differential equations (e.g. Kippenhahn and Weigert (1990)),

$$\frac{\partial P}{\partial M_r} = -\frac{GM_r}{4\pi r^4}, \quad (2.1)$$

$$\frac{\partial r}{\partial M_r} = \frac{1}{4\pi r^2 \rho}, \quad (2.2)$$

$$\frac{\partial T}{\partial M_r} = -\frac{GM_r T}{4\pi r^4 P} \nabla, \quad (2.3)$$

and the equation of state,

$$\rho = \rho(P, T) \quad (2.4)$$

where r is the planetocentric distance, M_r is the mass contained in the sphere with radius of r , P is the pressure, ρ is the density, T is the temperature, and $G(= 6.67 \times 10^{-8} \text{ dyn cm}^2 \text{ g}^{-2})$ is the gravitational constant. The symbol ∇ is the temperature gradient with respect to pressure, which means $\nabla = \frac{d \ln T}{d \ln P}$. We assume that the water envelope and rocky core are fully convective, and the convection is vigorous enough that the entropy S is constant; namely,

$$\nabla = \nabla_{\text{ad}}. \quad (2.5)$$

2.2.2 Atmospheric structure

The assumptions for the atmospheric structure are shown here.

- The atmosphere is one-dimensional radiative-convective equilibrium.
- The net flux is constant through the atmosphere.
- The atmosphere contains five molecules; hydrogen, helium, water, ammonia, and methane.
- Each molecule's distribution in the atmosphere is dominated by the saturation pressure of each molecule.
- The interface between the atmosphere and interior corresponds to the pressure of $P_{\text{btm}} = 100 \text{ bar}$.

The temperature-pressure relation in the stratosphere is determined by the analytical formula that was derived by Matsui and Abe (1986),

$$\sigma T^4 = F_0 \frac{\tau + 1}{2} + \frac{S_0 (\lambda + \alpha) + (\lambda - \alpha)\beta + (\alpha^2/\lambda - \lambda)(e^{-\alpha\tau} + \beta e^{\alpha t})}{4(1 + \alpha) + (1 - \alpha)\beta} \quad (2.6)$$

where τ and t are the normal optical depths for the long- and short-wave radiation fluxes, S_0 is the solar flux, F_0 is the thermal energy flux given at the base of the atmosphere, μ is the reflectivity of the short-wave radiation at the bottom of the atmosphere, ω is the

albedo for single scattering, $\lambda = \tau/t$, $\alpha = \sqrt{1-\omega}$, $\beta = \beta_0 e^{-2\alpha t}$, and $\beta_0 = [\mu(1+\alpha) - (1-\alpha)]/[(1+\alpha) - \mu(1-\alpha)]$. We introduce mean opacities κ_{th} and κ_{v} to describe τ and t . Subscripts "th" and "v" are opacities integrated by thermal and visible wavelength, respectively. In this study, we assume that the mean opacity for long-wavelength are described by the Rosseland mean opacities,

$$\frac{1}{\kappa_{\text{th}}} = \int_0^\infty \frac{1}{\kappa_\nu} \frac{dB_\nu(T_{\text{atm}})}{dT} d\nu \bigg/ \int_0^\infty \frac{dB_\nu(T_{\text{atm}})}{dT} d\nu, \quad (2.7)$$

where ν is the frequency, κ_ν is the opacity for ν , and B_ν is the Planck function. Then we represent $d\tau = \kappa_{\text{th}} dm$ where dm is a mass coordinate. The mean opacity for short-wavelength κ_{v} is quite unknown. In this calculation, we simply assume $\kappa_{\text{v}} = 0.1\kappa_{\text{th}}$. We assume $\omega = 1, \mu = 0$. Consequently, the temperature-pressure profile in the stratosphere is determined by

$$\sigma T^4 = F_0 \frac{\tau + 1}{2} + \frac{\sigma T_{\text{eq}}^4}{2} \left[1 + \frac{\kappa_{\text{th}}}{\kappa_{\text{v}}} + \left(\frac{\kappa_{\text{v}}}{\kappa_{\text{th}}} - \frac{\kappa_{\text{th}}}{\kappa_{\text{v}}} \right) e^{-\tau_{\text{v}}} \right], \quad (2.8)$$

where T_{eq} is the equilibrium temperature and $\sigma (= 5.67 \times 10^{-5} \text{ erg cm}^{-2} \text{ K}^{-4} \text{ s}^{-1})$ is the Stefan-Boltzmann constant. A comparison between the observations and our theoretical model is described in subsection 2.5.3. The position of photosphere (i.e. the optical depth is equal to unity) is important for the thermal evolution. As discussed below in subsection 2.5.3, using the Rosseland mean opacity is valid to determine the photosphere of the planet.

We assume the temperature-pressure relation in the tropopause is determined by the pseudo-moist adiabatic profile (Ingersoll, 1969; Atreya, 1986; Abe and Matsui, 1988). We set N numbers of species including j numbers of non-condensable species,

$$\frac{d \ln T}{d \ln P} = \left(\frac{\partial \ln T}{\partial \ln P} \right)_{\text{dry}} \frac{1 + \sum_{i=j+1}^N \frac{x_i}{1-x_i} \frac{d \ln p_i^*}{d \ln T}}{1 + \sum_{i=j+1}^N \frac{R_g}{C_p} \frac{x_i}{1-x_i} \frac{d \ln p_i^*}{d \ln T}}, \quad (2.9)$$

where $C_p = \sum_{i=1}^N x_i C_{p,i}$ is the mean heat capacity, p_i^* is the vapor pressure of the i -th condensable species ($i = j + 1, \dots, N$), respectively.

The radiation transfer equation is integrated using the Eddington approximation. The upward and downward radiation flux densities (F_{IR}^+ and F_{IR}^-) can be written as

$$F_{\text{IR}}^+(\tau) = \pi B(\tau) - \int_{\tau_b}^{\tau} \frac{d}{d\tau'} (\pi B(\tau')) \exp\left(-\frac{3}{2}(\tau' - \tau)\right) d\tau', \quad (2.10)$$

$$F_{\text{IR}}^-(\tau) = \pi B(\tau) - \int_0^{\tau} \frac{d}{d\tau'} (\pi B(\tau')) \exp\left(-\frac{3}{2}(\tau - \tau')\right) d\tau' - \pi B(0) \exp\left(-\frac{3}{2}\tau\right) \quad (2.11)$$

$$F_{\text{rad}} = F_{\text{IR}}^+ - F_{\text{IR}}^- - F_{\text{irr}}, \quad (2.12)$$

and

$$F_{\text{net}} = F_{\text{rad}} + F_c, \quad (2.13)$$

where F_c is the convective flux, F_{irr} is the direct solar flux. Note that $F_{\text{top}} = F_0 = F_{\text{IR}}^+(\tau = 0)$. We assume the net flux (2.13) is constant through the atmosphere and the convective flux F_c is equal to 0 in the stratosphere.

2.2.3 Thermal evolution

The thermal evolution of the planet is represented by the change of the entropy. That is, we can write the time evolution of entropy as

$$\frac{\partial L_r}{\partial M_r} = -T \frac{dS}{dt} \quad (2.14)$$

where M_r is the mass contained in a sphere of radius r , L_r is the luminosity in a sphere of radius r , T is the temperature, S is the entropy, and t is the time. We integrate Eq. 2.14 by the mass and obtain

$$L_p = - \left[\frac{dS_{\text{env}}}{dt} \int_{M_m}^{M_p} T dM_r + \frac{dS_m}{dt} \int_{M_c}^{M_m} T dM_r + \frac{dS_c}{dt} \int_0^{M_c} T dM_r \right], \quad (2.15)$$

where L_p is the planetary luminosity, S_{env} is the entropy of the envelope, S_m is the entropy of the mantle, S_c is the entropy of the core, M_c is the mass of the core, M_m is the mass of the mantle, respectively. L_p is written as

$$L_p = 4\pi R_p^2 F_{\text{top}}, \quad (2.16)$$

where R_p is the planetary radius and F_{top} is the outgoing flux from the top of the atmosphere.

2.2.4 Abundance in atmosphere and interior

We set the parameters for mass fractions of ice and rock. Here we define

$$Z_{\text{tot}} = \frac{W_e + W_m + R}{H + W_e + W_m + R}, \quad (2.17)$$

$$Z_0 = \frac{W_e}{H + W_e}, \quad (2.18)$$

$$Z_w = \frac{W_e + W_m}{W_e + W_m + R}, \quad (2.19)$$

where Z_{tot} is the total heavy elements mass fraction of the planet, Z_0 is the heavy element mass fraction in the envelope, Z_w is the water mass fraction in the heavy element, H is the hydrogen-helium mass in the envelope over planetary mass, W_e is the water mass in the envelope over the planetary mass, W_m is the water mass in the mantle over the planetary mass, R is the rocky core mass over the planetary mass, respectively. Note that $H + W_e + W_m + R = 1$. We assume the atmospheric mass fraction $M_a \sim 0$. That is,

$$H = 1 - Z_{\text{tot}} \quad (2.20)$$

$$W_e = \frac{Z_0}{1 - Z_0}(1 - Z_{\text{tot}}) \quad (2.21)$$

$$W_m = Z_w \cdot Z_{\text{tot}} - \frac{Z_0}{1 - Z_0}(1 - Z_{\text{tot}}) \quad (2.22)$$

$$R = (1 - Z_w) \cdot Z_{\text{tot}} \quad (2.23)$$

We assume $Z_w = 0.5$.

2.2.5 Opacities of hydrogen-helium

The opacities for hydrogen and helium are due to the collision induced absorption and Rayleigh scattering. We assume the mass fractions for hydrogen and helium are 75 % and 25 % respectively. We use the data table for the opacity for hydrogen-helium calculated by Freedman et al. (2008). The density and temperature range are from $\rho = 2.5 \times 10^{-12}$ to 10 g cm^{-3} and from $T = 10^2$ to 10^4 K , respectively.

2.2.6 Opacities of H₂O, NH₃, and CH₄

We calculate the line profiles for H₂O, NH₃, and CH₄ by use of HITRAN 2012 database (Rothman et al., 2013). We calculate the Rosseland mean opacity from line profiles whose temperature and pressure range are $P = 100, 10, 1, 0.1, 10^{-2}, 10^{-3}, 10^{-4}$ bar, and $T = 70, 100, 200, 300, 400, 500, 600, 700, 800, 900$ K, respectively.

The calculation method of line profiles is based on Rothman et al. (1998). In following descriptions, h, c, k_B , and c_2 are the Planck constant, speed of light, Boltzmann constant, and the second radiation constant ($c_2 = hc/k_B$), respectively. The spectral line intensity [$\text{cm}^{-1}/\text{molecule cm}^{-2}$] is defined here for a single molecule, which is a function of the spectral line transition frequency [cm^{-1}]. The transition between lower and upper states η and η' is accompanied by the emission or absorption of a photon of energy $E = \nu_{\eta\eta'}$. The line intensity $S_{\eta\eta'}$ is written by

$$S_{\eta\eta'}(T) = S_{\eta\eta'}(T_{\text{ref}}) \frac{Q(T_{\text{ref}})}{Q(T)} \frac{\exp(-c_2 E_{\eta}/T)}{\exp(-c_2 E_{\eta}/T_{\text{ref}})} \frac{1 - \exp(-c_2 \nu_{\eta\eta'}/T)}{1 - \exp(-c_2 \nu_{\eta\eta'}/T_{\text{ref}})}, \quad (2.24)$$

where T is the temperature, T_{ref} is the reference temperature ($T_{\text{ref}} = 296$ K), Q is the partition function, E_{η} is the lower state energy of the transition, and $\nu_{\eta\eta'}$ is the spectral line transition frequency, respectively. In our calculations, we use $\nu_{\eta\eta'} = E_{\eta'} - E_{\eta}$. Data of $S_{\eta\eta'}(T_{\text{ref}})$ and E_{η} for a frequency ν are tabulated in the HITRAN data table. The partition function $Q(T)$ is calculated by TIPS code developed by Fischer et al. (2003). Using the line intensities, we can calculate the cross section for $k_{\eta\eta'}(\nu, T, p)$ by use of the Voigt-profile

$$k_{\eta\eta'}(\nu, T, p) = S_{\eta\eta'} f_V(\nu - \nu_{\eta\eta'}), \quad (2.25)$$

where f_V is the Voigt-profile function, and p is the pressure. The Voigt-profile is described by the Lorentz profile f_L and Doppler profile f_D as

$$f_V(\nu - \nu_{\eta\eta'}) = \int_{-\infty}^{\infty} f_L(\nu' - \nu_{\eta\eta'}) f_D(\nu - \nu') d\nu', \quad (2.26)$$

where

$$f_L(\nu - \nu_{\eta\eta'}) = \frac{\alpha_L}{\pi[(\nu - \nu_{\eta\eta'})^2 + \alpha_L^2]} \quad (2.27)$$

$$f_D(\nu - \nu_{\eta\eta'}) = \frac{1}{\alpha_D \pi^{1/2}} \exp \left[-\frac{(\nu - \nu_{\eta\eta'})^2}{\alpha_D^2} \right]. \quad (2.28)$$

The doppler width α_D is described by $\alpha_D = \nu_{\eta\eta'} \left(\frac{2k_B T}{mc^2} \right)^{1/2}$. The Lorentz half-width α_L is described by $\alpha_L = \alpha_L(p_{\text{ref}}, T_{\text{ref}}) \left(\frac{p}{p_{\text{ref}}} \right) \left(\frac{T}{T_{\text{ref}}} \right)^n$, where p_{ref} is the reference pressure ($p_{\text{ref}} = 1$ bar). Those parameters are tabulated in HITRAN database (Rothman et al., 2013). The Voigt profile is calculated by Kuntz (1997). Kuntz (1997) showed a implementation of Humlicek's algorithm for approximation the Voigt profile function. Humlicek's implementation has error at most 2×10^{-6} , which is correspond to the cutoff for the Voigt function. Thus, our calculations include the cutoff implicitly, which stems from the error of Humlicek's implementation. With the above methods, we can calculate the cross section $k_{\eta\eta'}(\nu)$. Then we can obtain the opacity $\kappa(\nu)$ as

$$\kappa(\nu) = \frac{k_{\eta\eta'}(\nu, T, p)}{M}, \quad (2.29)$$

where M is the mass of molecule. With Eq. 2.7 and $\kappa(\nu)$, we can obtain the Rosseland mean opacity. In this study, we calculated the mean opacity κ as

$$\kappa = x_H \kappa_H + x_{He} \kappa_{He} + x_{H_2O} \kappa_{H_2O} + x_{NH_3} \kappa_{NH_3} + x_{CH_4} \kappa_{CH_4} \quad (2.30)$$

where $x_H, x_{He}, x_{H_2O}, x_{NH_3}, x_{CH_4}$ are the mole fraction of hydrogen molecule, helium, water, ammonia, and methane, respectively.

2.2.7 Equations of state

In the high pressure regime, the ideal gas approximation is no longer valid. That is because the interaction of molecule is not negligible. In this study, we use the equation of state for H and He based on Saumon et al. (1995), which is derived by the thermodynamic model. Saumon et al. (1995) covers the range $2.10 < \log T(\text{K}) < 7.06$ and $4 < \log P(\text{dyn cm}^{-2}) < 19$ and includes partial dissociation and ionization caused by

both pressure and temperature effects.

We use the equation of state for H₂O, SESAME 7150 (Lyon and Johnson, 1992), which is derived by the thermodynamic model. SESAME 7150 covers the density range from $9.98 \times 10 \text{ g/cm}^{-7}$ to $4.99 \times 10^3 \text{ g/cm}^3$ and the temperature range from 0.00 K to $1.16 \times 10^9 \text{ K}$. I combine these two equations of state. For $1.00 \times 10^{-6} \text{ g/cm}^3 \leq \rho \leq 1.50 \times 10^1 \text{ g/cm}^3$ and $1.0 \times 10^3 \text{ K} \leq T \leq 2.4 \times 10^4 \text{ K}$,

We assume that the composition for the rocky core is the same as the mineralogical composition known for Earth. In the pressure regime corresponding to the upper mantle of Earth, the lower-pressure form is taken to be olivine (hereafter "ol") and the higher-pressure forms of olivine are wadsleyite [hereafter "wd"] and ringwoodite [hereafter "rw"]. In the higher pressure regime corresponding to the lower mantle of Earth, rw transforms to perovskite (hereafter "pv") and ferromagnesiowüstite (hereafter "fmw"), with an additional shell at high pressures when pv transforms to post-perovskite (hereafter ppv). We adopt the equations of state of rocks derived by Valencia et al. (2007), which uses Vinet EOS (Vinet et al., 1987);

$$P(x, 300) = 3K_0(x^{2/3} - x^{1/3}) \exp \left[\frac{3}{2}(K'_0 - 1)(1 - x^{-1/3}) \right] \quad (2.31)$$

where P is the pressure in GPa, $x = (\rho/\rho_0)^{-1/3}$ and K_0 and K'_0 is the isothermal bulk modulus and its first pressure derivative at a reference state—zero pressure and 300 K. Table 2.1 list parameters for Eq.(2.31) and Table 2.2 shows the condition of phase transitions.

Composition	ρ_0 (kg/m ³)	K_0 (GPa)	K'_0
ol	3347	126.8	4.274
wd+rw	3644	174.5	4.274
pv+fmw	4152	223.6	4.274
ppv+fmw	4270	233.6	4.524

Table 2.1: Parameters for Vinet EOS used in each shell of the model.

The envelope is mixed with hydrogen, helium, and water. We assume the equation of state satisfies the volume additive law (Saumon et al., 1995; Soubiran and Militzer,

Transition	Boundary
ol→ wd+rw	$T \geq 400P - 4287$
rw→ pv+fmw	$P \geq 22.6$ if $T > 1750\text{K}$ $T \geq 13573 - 500P$ if $T \leq 1750\text{K}$
pv+fmw→ppv+fmw	$T \geq 133P - 1392$

Table 2.2: Phase boundaries of constituent materials of the rocky core. P is in GPa and T is in kelvins.

2015),

$$\frac{1}{\rho(P, T)} = (1 - Z_0) \left(\frac{X}{\rho_H(P, T)} + \frac{Y}{\rho_{He}(P, T)} \right) + \frac{Z_0}{\rho_{H_2O}(P, T)}, \quad (2.32)$$

where ρ is the density for the mixture gas, Z_0 is the mass fraction for water in the envelope, and X and Y are the mass fractions of hydrogen and helium, respectively. ρ_H , ρ_{He} and ρ_{H_2O} are the densities of hydrogen, helium, and water, respectively. Note that the definition of X , Y , and Z are described by the mass fractions of hydrogen x_H , helium x_{He} and water x_W in the area of interest. We can represent

$$X = \frac{x_H}{x_H + x_{He}}, \quad (2.33)$$

$$Y = \frac{x_{He}}{x_H + x_{He}}, \quad (2.34)$$

$$Z = \frac{x_W}{x_H + x_{He} + x_W}. \quad (2.35)$$

In this study, we assumed $X = 0.75$ and $Y = 0.25$. Z is determined by the water mass fraction in the envelope Z_0 . Here we assumed $Z_0 = Z$. Since the behavior of ammonia and methane in the high-pressure and high-temperature are not well known, we assumed the equations of state, for ammonia and methane are substituted by that for water in the envelope in accordance with the previous research (Nettelmann et al., 2013). Here we deal with Z_0 as the sum of the water, ammonia, and methane.

Adiabatic profile and mixing entropies

We estimate the adiabatic temperature gradient of as

$$\nabla_{\text{ad}} = -\frac{\left(\frac{\partial \ln S}{\partial \ln P}\right)_T}{\left(\frac{\partial \ln S}{\partial \ln T}\right)_P} = -\frac{S_P}{S_T}, \quad (2.36)$$

where, $S_P = \left(\frac{\partial \ln S}{\partial \ln P}\right)_T$, $S_T = \left(\frac{\partial \ln S}{\partial \ln T}\right)_P$. The total entropy for m kinds of spices is written by

$$\frac{\bar{S}}{k_B} = \sum_{i=1}^m \frac{\bar{S}_i}{k_B} + \frac{\bar{S}_{\text{mix}}}{k_B}, \quad (2.37)$$

$$\frac{\bar{S}_{\text{mix}}}{k_B} = N \ln N - \sum_{i=1}^m N_i \ln N_i, \quad (2.38)$$

where \bar{S} is the total entropy par particle, N_i is the number density for i -th spices, k_B is the Boltzmann constant, \bar{S}_i is the entropy par particle for i -th spices, and $N = \sum_{i=1}^m N_i$. Soubiran and Militzer (2015) calculate the ab initio simulations of liquid water-hydrogen mixtures. They conclude that the thermodynamic behavior of water-hydrogen mixtures can be described by a ideal mixing approximation. Here we assumed that the mixing entropy is described by a ideal mixing formulation. In this study, we consider the equation of state including the hydrogen, helium, and oxygen atom. The equation of state mixed with the hydrogen, helium, and oxygen atom is written by

$$\begin{aligned} \frac{\bar{S}_{\text{mix}}}{k_B} = & (\mathcal{N}_{\text{H}} + \mathcal{N}_{\text{He}} + \mathcal{N}_{\text{H}_2\text{O}}) \ln(\mathcal{N}_{\text{H}} + \mathcal{N}_{\text{He}} + \mathcal{N}_{\text{H}_2\text{O}}) \\ & - N_{\text{H}_2} \ln N_{\text{H}_2} - N_{\text{H}} \ln N_{\text{H}} - N_{\text{H}^+} \ln N_{\text{H}^+} \\ & - N_{\text{H}_2\text{O}} \ln N_{\text{H}_2\text{O}} - N_{\text{OH}} \ln N_{\text{OH}} - N_{\text{OH}^-} \ln N_{\text{OH}^-} \\ & - N_{\text{O}} \ln N_{\text{O}} - N_{\text{O}^-} \ln N_{\text{O}^-} - N_{\text{O}^{2-}} \ln N_{\text{O}^{2-}} - N_{\text{O}_2} \ln N_{\text{O}_2} \\ & - N_{\text{He}} \ln N_{\text{He}} - N_{\text{He}^+} \ln N_{\text{He}^+} - N_{\text{He}^{2+}} \ln N_{\text{He}^{2+}} \\ & - N_{\text{e}} \ln N_{\text{e}}, \end{aligned}$$

where \mathcal{N} is the number of electron for each molecule, N is the number for each molecule

$$N = N^{\text{H}} + N^{\text{He}} + N^{\text{H}_2\text{O}}, \quad (2.39)$$

respectively. The number of each molecule is calculated by chemical reactions between H, He, O, and electrons. We can obtain the mixing entropy as

$$\begin{aligned} \frac{\bar{S}_{\text{mix}}}{k_B} &= \frac{\bar{S}_{\text{H-mix}}}{k_B} + \frac{\bar{S}_{\text{He-mix}}}{k_B} + \frac{\bar{S}_{\text{H}_2\text{O-mix}}}{k_B} \\ &+ \mathcal{N}_{\text{H}} \ln \left(1 + \frac{\mathcal{N}_{\text{He}}}{\mathcal{N}_{\text{H}}} + \frac{\mathcal{N}_{\text{H}_2\text{O}}}{\mathcal{N}_{\text{H}}} \right) + \mathcal{N}_{\text{He}} \ln \left(1 + \frac{\mathcal{N}_{\text{H}}}{\mathcal{N}_{\text{He}}} + \frac{\mathcal{N}_{\text{H}_2\text{O}}}{\mathcal{N}_{\text{He}}} \right) \\ &+ \mathcal{N}_{\text{H}_2\text{O}} \ln \left(1 + \frac{\mathcal{N}_{\text{H}}}{\mathcal{N}_{\text{H}_2\text{O}}} + \frac{\mathcal{N}_{\text{He}}}{\mathcal{N}_{\text{H}_2\text{O}}} \right) \\ &- N_{\text{H}_2}^{\text{H}} \ln \left(1 + \frac{N_{\text{H}_2\text{O}}^{\text{H}_2\text{O}}}{N_{\text{H}_2}^{\text{H}_2}} \right) - N_{\text{H}_2\text{O}}^{\text{H}_2\text{O}} \ln \left(1 + \frac{N_{\text{H}_2}^{\text{H}}}{N_{\text{H}_2\text{O}}^{\text{H}_2\text{O}}} \right) \\ &- N_{\text{H}}^{\text{H}} \ln \left(1 + \frac{N_{\text{H}_2\text{O}}^{\text{H}}}{N_{\text{H}}^{\text{H}}} \right) - N_{\text{H}_2\text{O}}^{\text{H}} \ln \left(1 + \frac{N_{\text{H}}^{\text{H}_2\text{O}}}{N_{\text{H}_2\text{O}}^{\text{H}}} \right) \\ &- N_{\text{H}^+}^{\text{H}} \ln \left(1 + \frac{N_{\text{H}_2\text{O}}^{\text{H}^+}}{N_{\text{H}^+}^{\text{H}}} \right) - N_{\text{H}_2\text{O}}^{\text{H}^+} \ln \left(1 + \frac{N_{\text{H}^+}^{\text{H}_2\text{O}}}{N_{\text{H}_2\text{O}}^{\text{H}^+}} \right) \\ &- N_e^{\text{H}} \ln \left(1 + \frac{N_e^{\text{H}}}{N_e^{\text{H}}} + \frac{N_e^{\text{H}_2\text{O}}}{N_e^{\text{H}}} \right) - N_e^{\text{He}} \ln \left(1 + \frac{N_e^{\text{H}}}{N_e^{\text{He}}} + \frac{N_e^{\text{H}_2\text{O}}}{N_e^{\text{He}}} \right) \\ &- N_e^{\text{H}_2\text{O}} \ln \left(1 + \frac{N_e^{\text{H}}}{N_e^{\text{H}_2\text{O}}} + \frac{N_e^{\text{He}}}{N_e^{\text{H}_2\text{O}}} \right). \end{aligned}$$

For given pressure P and temperature T ,

$$n_i^{\text{H}} = \frac{2\rho/m_{\text{H}}}{1 + 3X_{\text{H}_2} + X_{\text{H}}} X_i = \frac{\rho}{m_{\text{H}}} n_{\text{H}} X_i, \quad (2.40)$$

$$n_i^{\text{He}} = \frac{3\rho/m_{\text{He}}}{1 + 2X_{\text{He}} + X_{\text{He}^+}} X_i = \frac{\rho}{m_{\text{He}}} n_{\text{He}} X_i, \quad (2.41)$$

$$n_i^{\text{H}_2\text{O}} = \frac{\rho/m_{\text{H}_2\text{O}}}{2X_{\text{O}^{2-}} + X_{\text{O}^-} + X_{\text{OH}^-} - X_{\text{H}^+} + 1} X_i = \frac{\rho}{m_{\text{H}_2\text{O}}} n_{\text{H}_2\text{O}} X_i, \quad (2.42)$$

where $X_i = N_i/N$. We can obtain the mixing entropy as

$$\begin{aligned}
& \frac{\bar{S}_{\text{int-mix}}}{\rho k_B} \\
= & \frac{(1-Z)(1-Y)}{m_H} \ln \left(1 + \frac{m_H}{m_{He}} \frac{Y}{1-Y} \frac{n_{He}}{n_H} + \frac{m_H}{m_{H_2O}} \frac{Z}{(1-Z)(1-Y)} \frac{n_{H_2O}}{n_H} \right) \\
& + \frac{(1-Z)Y}{m_{He}} \ln \left(1 + \frac{n_H}{n_{He}} \frac{m_{He}}{m_H} \frac{1-Y}{Y} + \frac{n_{H_2O}}{n_{He}} \frac{m_{He}}{m_{H_2O}} \frac{Z}{(1-Z)Y} \right) \\
& + \frac{Z}{m_{H_2O}} \ln \left(1 + \frac{n_H}{n_{H_2O}} \frac{m_{H_2O}}{m_H} \frac{(1-Z)(1-Y)}{Z} + \frac{n_{He}}{n_{H_2O}} \frac{m_{H_2O}}{m_{He}} \frac{(1-Z)Y}{Z} \right) \\
& - \frac{(1-Z)(1-Y)}{m_H} X_{H_2}^H \ln \left(1 + \frac{n_{H_2O}}{n_H} \frac{m_H}{m_{H_2O}} \frac{Z}{(1-Z)(1-Y)} \frac{X_{H_2}^{H_2O}}{X_{H_2}^H} \right) \\
& - \frac{Z X_{H_2}^{H_2O}}{m_{H_2O}} \ln \left(1 + \frac{n_H}{n_{H_2O}} \frac{m_{H_2O}}{m_H} \frac{(1-Z)(1-Y)}{Z} \frac{X_{H_2}^H}{X_{H_2}^{H_2O}} \right) \\
& - \frac{(1-Z)(1-Y)}{m_H} X_H^H \ln \left(1 + \frac{n_{H_2O}}{n_H} \frac{m_H}{m_{H_2O}} \frac{Z}{(1-Z)(1-Y)} \frac{X_H^{H_2O}}{X_H^H} \right) \\
& - \frac{Z X_H^{H_2O}}{m_{H_2O}} \ln \left(1 + \frac{n_H}{n_{H_2O}} \frac{m_{H_2O}}{m_H} \frac{(1-Z)(1-Y)}{Z} \frac{X_H^H}{X_H^{H_2O}} \right) \\
& - \frac{(1-Z)(1-Y)}{m_H} X_{H^+}^H \ln \left(1 + \frac{n_{H_2O}}{n_H} \frac{m_H}{m_{H_2O}} \frac{Z}{(1-Z)(1-Y)} \frac{X_{H^+}^{H_2O}}{X_{H^+}^H} \right) \\
& - \frac{Z X_{H^+}^{H_2O}}{m_{H_2O}} \ln \left(1 + \frac{n_H}{n_{H_2O}} \frac{m_{H_2O}}{m_H} \frac{(1-Z)(1-Y)}{Z} \frac{X_{H^+}^H}{X_{H^+}^{H_2O}} \right) \\
& - \frac{(1-Z)(1-Y)}{m_H} X_e^H \ln \left(1 + \frac{m_H}{m_{He}} \frac{Y}{1-Y} \frac{n_{He}}{n_H} \frac{X_e^{He}}{X_e^H} + \frac{m_H}{m_{H_2O}} \frac{Z}{(1-Z)(1-Y)} \frac{n_{H_2O}}{n_H} \frac{X_e^{H_2O}}{X_e^H} \right) \\
& - \frac{(1-Z)Y}{m_{He}} X_e^{He} \ln \left(1 + \frac{n_H}{n_{He}} \frac{m_{He}}{m_H} \frac{1-Y}{Y} \frac{X_e^H}{X_e^{He}} + \frac{n_{H_2O}}{n_{He}} \frac{m_{He}}{m_{H_2O}} \frac{Z}{(1-Z)Y} \frac{X_e^{H_2O}}{X_e^{He}} \right) \\
& - \frac{Z}{m_{H_2O}} X_e^{H_2O} \ln \left(1 + \frac{n_H}{n_{H_2O}} \frac{m_{H_2O}}{m_H} \frac{(1-Z)(1-Y)}{Z} \frac{X_e^H}{X_e^{H_2O}} + \frac{n_{He}}{n_{H_2O}} \frac{m_{H_2O}}{m_{He}} \frac{(1-Z)Y}{Z} \frac{X_e^{He}}{X_e^{H_2O}} \right),
\end{aligned}$$

where we set

$$A = \frac{(1-Z)(1-Y)}{m_H} \quad (2.43)$$

$$f_{heh} = \frac{Y}{1-Y} \frac{m_H}{m_{He}} \quad (2.44)$$

$$f_{wh} = \frac{Z}{(1-Z)(1-Y)} \frac{m_H}{m_{H_2O}} \quad (2.45)$$

$$f_{whe} = \frac{Z}{(1-Z)Y} \frac{m_{He}}{m_{H_2O}} \quad (2.46)$$

$$n_{heh} = \frac{n_{He}}{n_H} \quad (2.47)$$

$$n_{wh} = \frac{n_{H_2O}}{n_H} \quad (2.48)$$

$$n_{whe} = \frac{n_{H_2O}}{n_{He}}, \quad (2.49)$$

and

$$\begin{aligned} \frac{\bar{S}_{\text{int-mix}}}{\rho A k_B} = & \ln(1 + f_{heh}n_{heh} + f_{wh}n_{wh}) + f_{heh} \ln\left(1 + \frac{1}{f_{heh}n_{heh}} + f_{whe}n_{whe}\right) \\ & + f_{wh} \ln\left(1 + \frac{1}{f_{wh}n_{wh}} + \frac{1}{f_{whe}n_{whe}}\right) \\ & - X_{H_2}^H \ln\left(1 + f_{wh}n_{wh} \frac{X_{H_2}^{H_2O}}{X_{H_2}^H}\right) - X_{H_2}^{H_2O} f_{wh} \ln\left(1 + \frac{1}{f_{wh}n_{wh}} \frac{X_{H_2}^H}{X_{H_2}^{H_2O}}\right) \\ & - X_H^H \ln\left(1 + f_{wh}n_{wh} \frac{X_H^{H_2O}}{X_H^H}\right) - X_H^{H_2O} f_{wh} \ln\left(1 + \frac{1}{f_{wh}n_{wh}} \frac{X_H^H}{X_H^{H_2O}}\right) \\ & - X_{H^+}^H \ln\left(1 + f_{wh}n_{wh} \frac{X_{H^+}^{H_2O}}{X_{H^+}^H}\right) - X_{H^+}^{H_2O} f_{wh} \ln\left(1 + \frac{1}{f_{wh}n_{wh}} \frac{X_{H^+}^H}{X_{H^+}^{H_2O}}\right) \\ & - X_e^H \ln\left(1 + f_{heh}n_{heh} \frac{X_e^{He}}{X_e^H} + f_{wh}n_{wh} \frac{X_e^{H_2O}}{X_e^H}\right) \\ & - X_e^{He} f_{heh} \ln\left(1 + \frac{1}{f_{heh}n_{heh}} \frac{X_e^H}{X_e^{He}} + f_{whe}n_{whe} \frac{X_e^{H_2O}}{X_e^{He}}\right) \\ & - X_e^{H_2O} f_{wh} \ln\left(1 + \frac{1}{f_{wh}n_{wh}} \frac{X_e^H}{X_e^{H_2O}} + \frac{1}{f_{whe}n_{whe}} \frac{X_e^{He}}{X_e^{H_2O}}\right) \end{aligned}$$

respectively. Hence, we can obtain the entropy as

$$S_{\text{mix}} = S_{H\text{-mix}} + S_{He\text{-mix}} + S_{H_2O\text{-mix}} + S_{\text{int-mix}}. \quad (2.50)$$

2.2.8 Condensation curves

The condensation curve is derived by the Clausius-Clapeyron equation. In this study, the condensation curve of H₂O is used derived by Nakajima et al. (1992) and those of NH₃ and CH₄ are used derived by Sánchez-Lavega et al. (2004). The condensation curve is written by

$$\ln P_V = \ln C + \frac{\mu}{R_g} \left[-\frac{L_0}{T} + \Delta\alpha \ln T + \frac{\Delta\beta}{2} T \right] \quad (2.51)$$

where P_V is the vapor pressure, T is the temperature, μ is the molecular weight, L_0 is the latent heat, and $R_g (= 8.31 \times 10^7 \text{ erg K}^{-1}\text{g}^{-1})$ is the universal gas constant. Parameters for Eq. (2.51) are listed in Table (2.3). Heat capacities of ice compositions are $4 R_g$,

Component	$\ln C$ (C in bars)	L_0 (J·g ⁻¹)	$\Delta\alpha$ (J·g ⁻¹ ·K ⁻¹)	$\Delta\beta/2$ (J·g ⁻¹ ·K ⁻²)	μ (g mole ⁻¹)
H ₂ O	27.967	2425.3	0	0	18.0
NH ₃	27.863	2016	-0.888	0	17.0
CH ₄	1.627	553.1	1.002	-4.1×10^{-3}	16.0

Table 2.3: Parameters for the condensation curves. Parameters for H₂O is derived by Nakajima et al. (1992). Parameters for NH₃ and CH₄ are derived by Sánchez-Lavega et al. (2004).

which are assumed the ideal gas approximation. The critical temperature in K and pressure in atm (T_c, P_c) of water, ammonia, and methane are (647.3, 217.6), (405.6, 111.3), and (190.6, 45.4), respectively (Reid et al., 1987). If the pressure is greater than the critical pressure, the molecule behave as a supercritical fluid. Then the condensation curve cannot be adopted. The water-hydrogen mixing ratios at high temperature (2000-6000 K) and high pressure (a few tens of GPa) was calculated using ab initio molecular dynamics simulations. The previous studies found that water was miscible in hydrogen (Wilson and Militzer, 2012; Soubiran and Militzer, 2015). Our model assumed that when water, ammonia, and methane molecule behave as supercritical fluids, those molecules are miscible with a hydrogen and helium. In this study, we assumed that the condensation curves for water, ammonia, and methane are extrapolated up to 100 bar.

2.3 Numerical procedure

In this subsection, we introduce the numerical procedure. To simulate the thermal evolution, we integrate Eq. (2.15) by the following procedure. Our model is consisted of three parts, the atmospheric structure, the interior structure, and the thermal evolution.

We assume the radiative-convective boundary height p_{ad} and F_{top} . The temperature-pressure profile is determined by Eq. (2.6) in the stratosphere and Eq. (2.9) in the troposphere respectively. Then we can determine the flux distributions for upward and downward by Eqs. (2.10), (2.11), (2.12), and (2.13). The radiative-convective boundary is determined by the divergence of the net flux for radiation. That is,

$$\frac{dF_{\text{rad}}}{d\tau} \sim \frac{F_{\text{rad}}^{i+1} - F_{\text{rad}}^i}{\tau_{i+1} - \tau_i} < 0 \implies \text{convective region}, \quad (2.52)$$

$$\frac{dF_{\text{rad}}}{d\tau} \sim \frac{F_{\text{rad}}^{i+1} - F_{\text{rad}}^i}{\tau_{i+1} - \tau_i} \geq 0 \implies \text{radiative region}. \quad (2.53)$$

where i is the number of grid of the atmosphere. We assume the bottom of the atmosphere is $P_{\text{btm}} = 100$ bar and the top of atmosphere is $P_{\text{top}} = 10^{-5}$ bar. We determine the self-consistent value of p_{ad} and F_{top} for a given atmospheric structure by an iterative method.

First we simulate two adiabatic interior models that are separated in time by a time interval Δt for the known $S_p(t)$ and an assumed $S_p(t + \Delta t)$, where S_p is the total entropy of the planet. The two structures should be integrated for two different values of the temperature at the bottom of atmosphere T_{btm} . To this end, we integrate Eqs. (2.1)-(2.5) inward from the bottom of the atmosphere ($P_{\text{btm}}, T_{\text{btm}}$) to the planetary center, using the fourth-order Runge-Kutta method. We then look for the solution that fulfills the inner boundary condition (i.e., $r = 0$ at $M_r = 0$) in an iterative fashion. Note that determining p_{ad} and F_{top} requires the gravity in the atmosphere (or the planetary radius R_p), which is obtained after the interior structure is determined. Thus, we have to find the solution in which the interior and atmospheric structures are consistent with each other also in an iterative fashion.

Then we calculate Δt from the second-order difference equation for Eq. (2.15), which

is written as

$$\Delta t = -\frac{1}{4\pi R_p^2(t+\Delta t)F_{\text{top}}(t+\Delta t) + 4\pi R_p(t)^2F_{\text{top}}(t)} \{ [\bar{S}_{\text{env}}(t+\Delta t) - \bar{S}_e(t)][\Theta_{\text{env}}(t+\Delta t) + \Theta_e(t)] + [\bar{S}_m(t+\Delta t) - \bar{S}_m(t)][\Theta_m(t+\Delta t) + \Theta_m(t)] + [\bar{S}_c(t+\Delta t) - \bar{S}_c(t)][\Theta_c(t+\Delta t) + \Theta_c(t)] \}, \quad (2.54)$$

where

$$\Theta_{\text{env}}(t) \equiv \int_{M_m}^{M_p} T(t) dM_r, \quad \Theta_m(t) \equiv \int_{M_c}^{M_m} T(t) dM_r, \quad \Theta_c(t) \equiv \int_0^{M_c} T(t) dM_r. \quad (2.55)$$

We have confirmed that our numerical code for the atmospheric structure reproduces well the p_{ad} and F_{top} values presented by Nakajima et al. (1992), given the infrared opacity $\kappa_{\text{th}} = 0.1 \text{ cm}^2 \text{ g}^{-1}$. Finally we have confirmed that our numerical code for the interior structure reproduces well the mass and radius relationship for super-Earths presented by Valencia et al. (2010).

We summarize parameters. Free parameter are the initial mole fraction of the ice (which includes H_2O , NH_3 , and CH_4) x_{btm} , the fraction of $\text{NH}_3/\text{H}_2\text{O}$, and $\text{CH}_4/\text{H}_2\text{O}$. In this study, we focus on the effect of x_{btm} , $\text{NH}_3/\text{H}_2\text{O}$, and $\text{CH}_4/\text{H}_2\text{O}$. We adjust Z_0 and Z_{tot} to satisfy the present radius of Uranus $R_U = 2.56 \times 10^9 \text{ cm}$ at the age of solar system. We assumed the planetary mass was the mass of Uranus $M_U (= 8.68 \times 10^{28} \text{ g})$, the equilibrium temperature $T_{\text{eq}} = 58.2 \text{ K}$ (Pearl and Conrath, 1991).

2.4 Results

Here we demonstrate the results of the calculations. Before showing the results, we summarize the assumptions and parameters in Table 2.4. We assumed the planetary mass was the mass of Uranus $M_U (= 8.68 \times 10^{28} \text{ g})$, the equilibrium temperature $T_{\text{eq}} = 58.2 \text{ K}$, $\text{NH}_3/\text{H}_2\text{O} = 0.135$, and $\text{CH}_4/\text{H}_2\text{O} = 0.05675$, which corresponds to a C/O value smaller by 0.1 than the solar composition. Since the planetary radius decreases with the time, we adjust Z_0 and Z_{tot} to satisfy the present radius of Uranus $R_U = 2.56 \times 10^9 \text{ cm}$ at the age of 5 giga years. Hence we set $Z_0 = 0.3$, $Z_{\text{tot}} = 0.8$, and $Z_w = 0.5$. Z_0 is equivalent to the mass fraction of metal in the outer envelope, which affects the gravitational moment.

Temperature	Mass	Z_0	Z_{tot}	NH ₃ /H ₂ O	CH ₄ /H ₂ O
58.2 K	M_U	0.3	0.8	0.135	0.05675

Table 2.4: Parameters we assumed in the calculation.

2.4.1 Atmospheric structure

We show the results of the atmospheric structure. Fig. 2.3 shows the atmospheric structure for $(P_{\text{btm}}, T_{\text{btm}}) = (100 \text{ bar}, 1000 \text{ K})$. We set 70 mol % of H₂O, 9.45 mol % of NH₃, and 3.97 mol % of CH₄. The atmospheric structure was composed of three parts; a dry convective region, a moist convective region, and a stratosphere from the bottom to the top. The lapse rate in the dry convective region was determined by the heat capacity of the ice components. That is, the lapse rate is described by a dry adiabatic lapse rate. When the atmosphere is cooled enough to condensate ice components, the lapse rate is changed due to the latent heat. In the case of Fig. 2.3, the condensed constituents are mainly water. Then the atmospheric temperature structure was determined by the moist adiabatic convection driven by the condensation of water. The stratosphere existed atop the moist convective region. Those atmospheric structure decide the outgoing flux from the top of the atmosphere.

As the bottom temperature is cooled, the main condensable constituents are gradually changed. Fig. 2.4 shows the atmospheric structure for various bottom temperatures. As the planet cools, the bottom temperature decreases. That is, those atmospheric structures represent the evolution of atmospheric structure. That affects the outgoing flux from the top of the atmosphere.

The outgoing flux from the top of the atmosphere (hereafter F_{top}) is determined by the atmospheric temperature-pressure structure. Fig. 2.5 shows the relationship between the F_{top} and the bottom temperature T_{btm} . This figure shows that the F_{top} becomes constant in particular temperature ranges. If the bottom temperature range is from 500 K to 1000 K, $F_{\text{top}} = 3.3 \times 10^5 \text{ erg s}^{-1}\text{cm}^{-2}$, which is a similar value with Komabayashi-Ingersoll limit of H₂O dominated atmosphere (Nakajima et al., 1992). That is because the atmospheric temperature structure is determined by the moist convection of water. The atmosphere's photosphere, which is equivalent to the optical depth of infrared wavelength is unity, is in the moist convective region. Therefore the F_{top} value is nearly constant while

the atmospheric structure is dominated by the moist convection due to the condensation of water. Hereafter we call such a flat F_{top} the radiation limit of water. The radiation limit also appears when the atmospheric composition is dominated by ammonia or methane.

As the bottom temperature decreases, F_{top} changes sharply when the bottom temperature reaches ~ 500 K. When the bottom temperature reaches ~ 400 K, the F_{top} value is nearly constant value again. That is because the atmospheric temperature-pressure structure is dominated by the moist convection due to the condensation of NH_3 . The F_{top} value is of the order of $10^4 \text{ erg s}^{-1}\text{cm}^{-2}$. This mechanism is same as the radiation limit of water and then we call such F_{top} as the radiation limit of ammonia.

The radiation limit of ammonia ceases when the bottom temperature is lower than ~ 300 K. Then the atmospheric structure is dominated by the condensation of CH_4 , which is the same as described above. However, if the atmosphere does not possess the sufficient amounts of condensable constituents to dominate the temperature-pressure structure by the moist adiabatic profile, the F_{top} value is not constant and the value decreases as the bottom temperature decreases.

Fig. 2.5 shows that F_{top} without the effect of the condensation is smaller than that with the effect of the condensation when T_{btm} is the same value. Since the dry adiabatic lapse rate is greater than the moist adiabatic lapse rate, photospheric temperature without the condensation is lower than that with the condensation. That difference in F_{top} should affect the planetary luminosity and the thermal evolution timescale.

2.4.2 Effect on the thermal evolution

In this subsection, we demonstrate the difference of the thermal evolution between without and with the condensation effect on the atmospheric structure. Fig. 2.6 shows the time evolution of the ice giant's luminosity. This figure indicates that the evolutionary track with the effect of the condensation has specific features compared to one without the condensation. The evolutionary track with the condensation shows a steplike evolution. The steps in the figure correspond to the radiation limits of condensable constituents. The timescale of thermal evolution becomes shorter than that without the condensation. As a result, the planetary luminosity decreased and reached the present luminosity of Uranus. On the other hand, the evolutionary track without the effect of the condensation did not

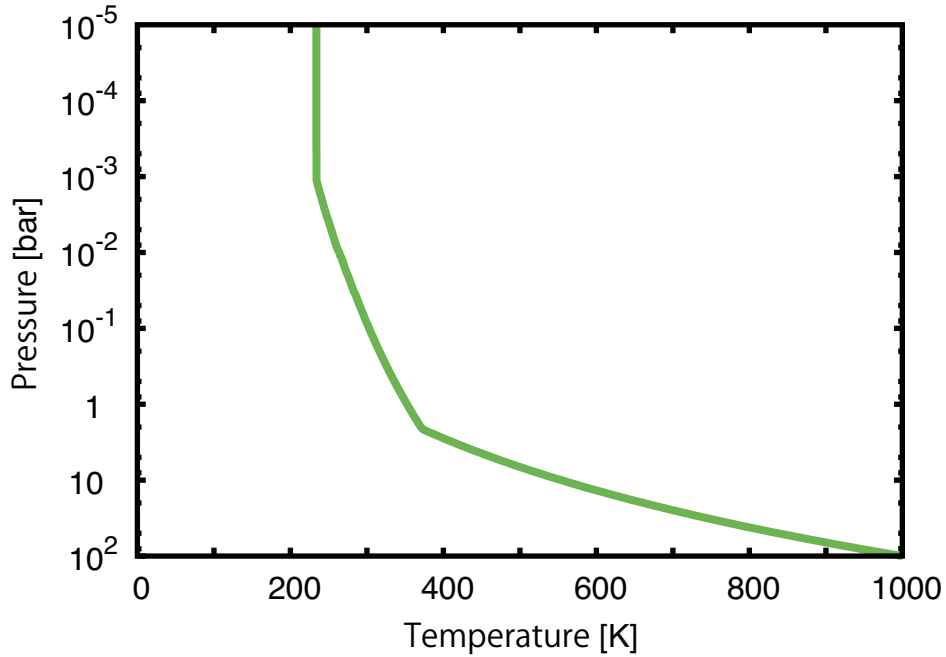


Figure 2.3: The temperature-pressure relation of atmosphere. We set 70 mol % of H_2O , 9.45 mol % of NH_3 , and 3.97 mol % of CH_4 , respectively. We assume $Z_{\text{tot}} = 0.8$, $Z_0 = 0.3$, and $Z_w = 0.5$. The bottom of atmosphere is $P = 100$ bar. Temperature at $P = 100$ bar is 1000 K. The equilibrium temperature is 58.2 K.

decrease enough to explain the present luminosity of Uranus within 5 gigayears. Figure 2.7 shows the elapsed time and the change of the total planetary entropy. We set $t = 0$ as the temperature at 100 bar is equal to 1000 K. We calculated the reduced rate of the total planetary entropy $(S_p(T_{\text{btm}} = 1000 \text{ K}) - S_p)/S_p(T_{\text{btm}} = 1000 \text{ K})$. We compared the decrease of the planetary entropy with and without the effect of condensable constituents in the atmosphere. We can find that the early stage of the evolution (namely within 10^8 years) is important for the thermal evolution of Uranus. The planetary entropy is quickly decreased compared to the result of without condensation. We conclude that the effect of the condensation is essential to describe the thermal evolution of Uranus.

Sensitivities to parameters: the initial content of ice constituents

We take different mole fractions of H_2O from 5 to 50 mol %. Fig. 2.8 shows the sensitivity of the initial content of ice compositions. For low water contents cases (dashed lines: 35 mol % or less), the luminosities at 4.6 Gyrs do not fall within the current luminosity range of Uranus even taking into account its errors. This in turn means that initial low

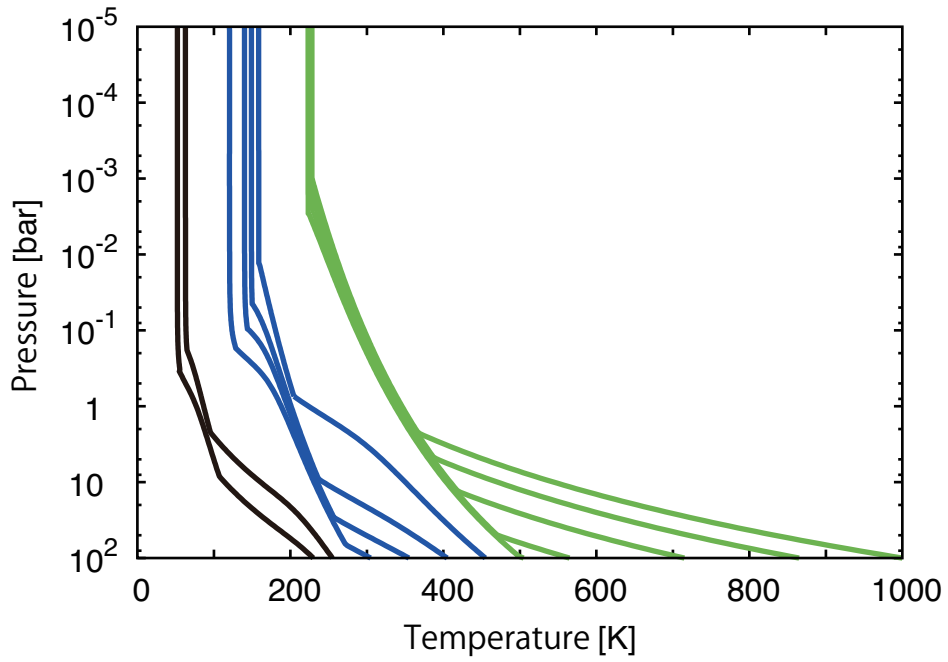


Figure 2.4: The temperature-pressure relation of atmosphere. We set 70 mol % of H_2O , 9.45 mol % of NH_3 , and 3.97 mol % of CH_4 , respectively. Line colors represent main compositions in the atmosphere. Green, blue, and black lines are H_2O , NH_3 , and CH_4 , respectively. We assume $Z_{\text{tot}} = 0.8$, $Z_0 = 0.3$, and $Z_w = 0.5$. The equilibrium temperature is 58.2 K.

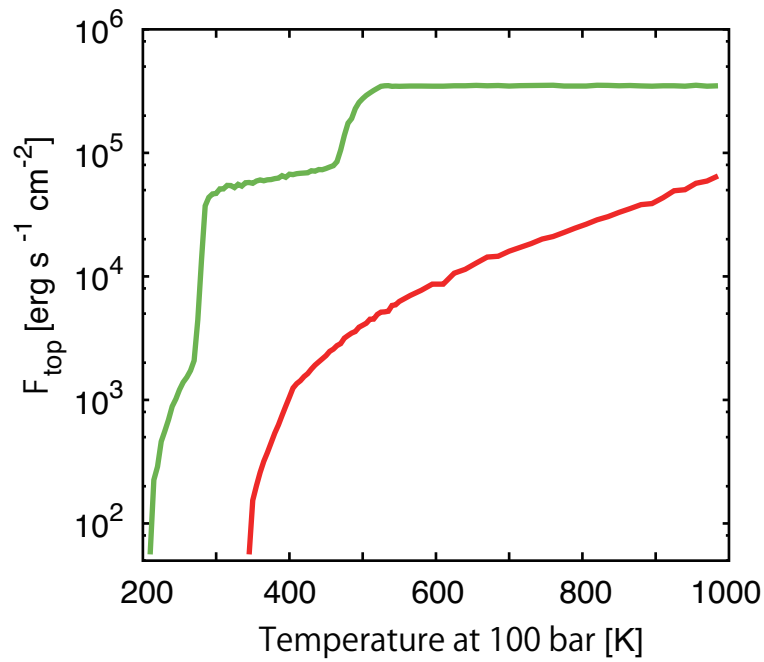


Figure 2.5: The relationship between the F_{top} and the temperature at 100 bar in the atmosphere. We set 70 mol % of H_2O , 9.45 mol % of NH_3 , and 3.97 mol % of CH_4 , respectively. The red line is the relationship without the effect of the condensation of H_2O , NH_3 , and CH_4 . The green line is the relationship with the effect of condensation of H_2O , NH_3 , and CH_4 . We assume $Z_{\text{tot}} = 0.8$, $Z_0 = 0.3$, and $Z_w = 0.5$. The equilibrium temperature is 58.2 K.

luminosities, e.g. 1.5 times the present values, are required to explain the current value. On the other hand, initial low luminosity is not required for high water content cases (solid lines). To explain the present luminosity of Uranus, the atmosphere is required to have possessed condensable constituents contents higher than 40 % in the atmosphere immediately after its formation, when Uranus started with in the high luminosity states (i.e., several hundreds times the present value). Figure 2.9 shows the relationship of the time and planetary luminosity that is followed backward in time from 4.6×10^9 years that is correspond to the age of solar system. The backward integration can be easy to understand those behaviors. We can find that the present luminosity of Uranus can explain if the atmosphere is allowed to possess condensable constituents contents higher than 40 % in the atmosphere.

Sensitivities to parameters: $\text{CH}_4/\text{H}_2\text{O}$, $\text{NH}_3/\text{H}_2\text{O}$

We investigate the sensitivities to the parameters of $\text{CH}_4/\text{H}_2\text{O}$ and $\text{NH}_3/\text{H}_2\text{O}$. In the above calculations, we assumed $\text{CH}_4/\text{H}_2\text{O} = 0.05675$, which was less than the solar C/O value, and $\text{NH}_3/\text{H}_2\text{O} = 0.135$, which was equal to the solar N/O. Figure 2.10 shows the evolution of the planetary luminosity assuming $\text{CH}_4/\text{H}_2\text{O} = 0.458$, which was equal to the solar C/O, and $\text{NH}_3/\text{H}_2\text{O} = 0.135$, which were equal to the solar N/O. We found that the thermal evolution timescale was longer than that for Fig. 2.8 at the same initial water mole fraction. That is because the condensation of methane prevented the cooling of the planet. If we want to explain the present luminosity of Uranus, the initial mole fraction of methane should be small. We also checked the effect of $\text{NH}_3/\text{H}_2\text{O}$. If we want to explain the present luminosity of Uranus, the initial $\text{NH}_3/\text{H}_2\text{O}$ should be larger than that of the solar N/O value according to the result of Fig 2.10. Fig. 2.11 shows the evolution of planetary luminosity assuming $\text{CH}_4/\text{H}_2\text{O} = 0.458$, which was equal to the solar C/O, and $\text{NH}_3/\text{H}_2\text{O} = 0.427$, which was $10^{0.5}$ times as large as the solar N/O. We can find that the thermal evolution timescale for $\text{NH}_3/\text{H}_2\text{O} = 0.427$ become shorter than that for the solar ratio of the $\text{NH}_3/\text{H}_2\text{O}$. That is, high $\text{NH}_3/\text{H}_2\text{O}$ and low $\text{CH}_4/\text{H}_2\text{O}$ are plausible to explain the present luminosity of Uranus.

Fig. 2.12 shows the $F_{\text{top}} - T_{\text{btm}}$ relations for $(\text{CH}_4/\text{H}_2\text{O}, \text{NH}_3/\text{H}_2\text{O}) = (0.135, 0.458)$. We also calculated the F_{top} without the effect of condensation. We can find that the

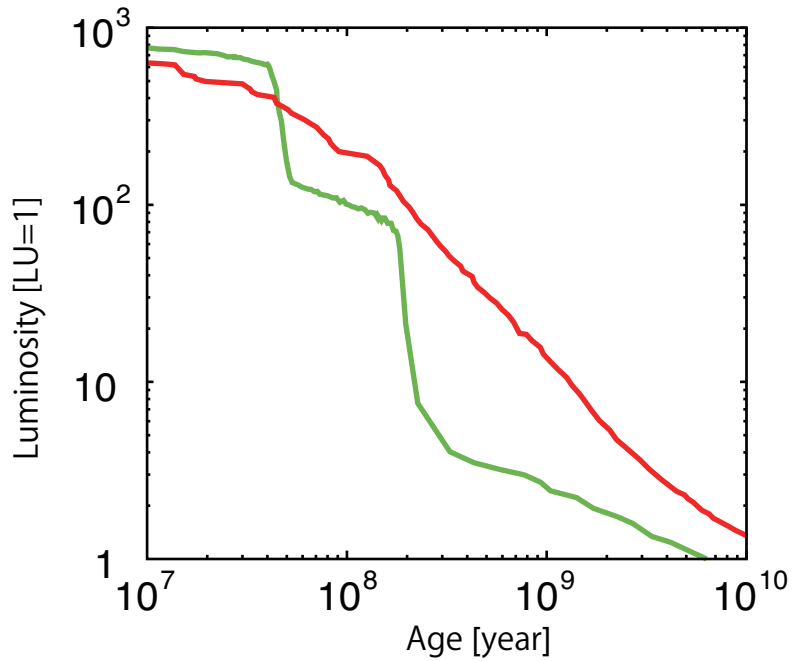


Figure 2.6: The time evolution of the planetary luminosity divided by the present luminosity of Uranus $LU = 5.6 \times 10^{22} \text{ erg s}^{-1}$. We set 70 mol % of H_2O , 9.45 mol % of NH_3 , and 3.97 mol % of CH_4 , respectively. The red line is the relationship without the effect of the condensation of H_2O , NH_3 , and CH_4 . The green line is the relationship with the effect of condensation of H_2O , NH_3 , and CH_4 . We assume $Z_{\text{tot}} = 0.8$, $Z_0 = 0.3$, and $Z_w = 0.5$. The equilibrium temperature is 58.2 K

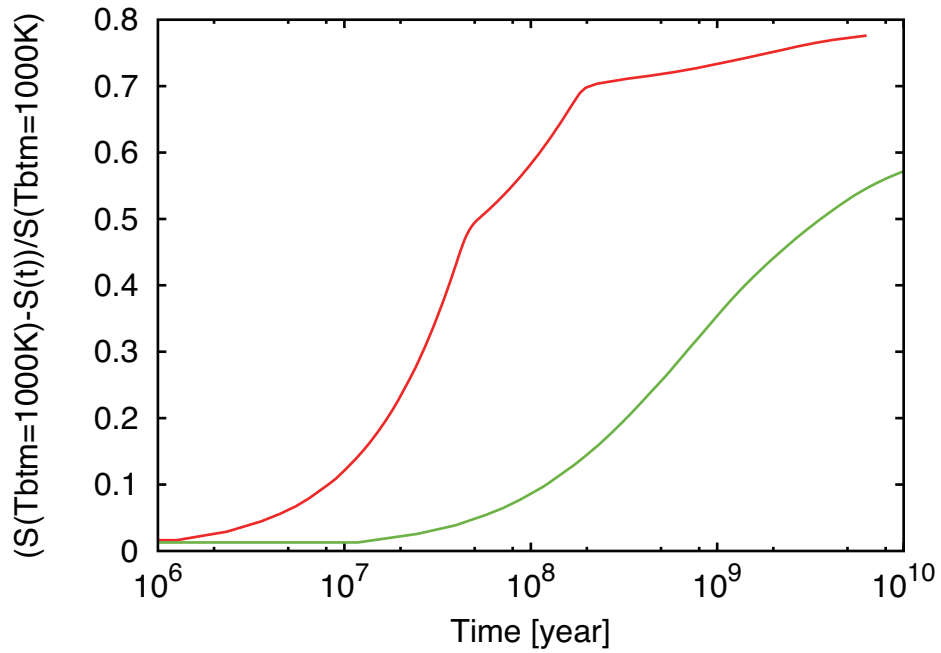


Figure 2.7: The time evolution of the planetary entropy. $t = 0$ represents the temperature at 100 bar 1000 K. We set 70 mol % of H_2O , 9.45 mol % of NH_3 , and 3.97 mol % of CH_4 , respectively. The red line is the relationship the effect of the condensation of H_2O , NH_3 , and CH_4 . The green line is the relationship without the effect of condensation of H_2O , NH_3 , and CH_4 . We assume $Z_{\text{tot}} = 0.8$, $Z_0 = 0.3$, and $Z_w = 0.5$. The equilibrium temperature is 58.2 K.

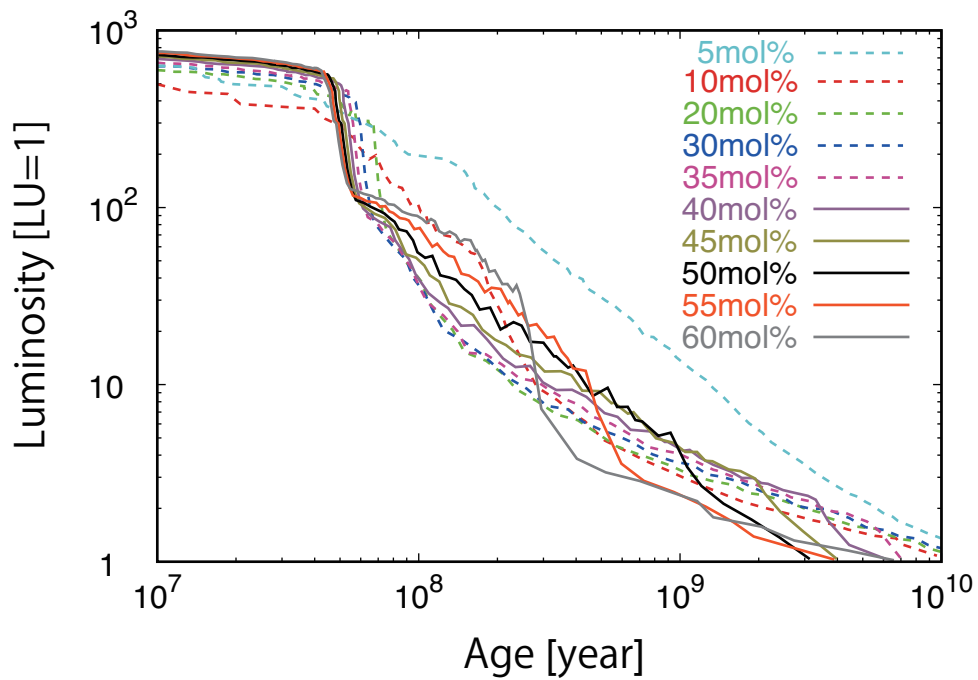


Figure 2.8: The time evolution of the planetary luminosity divided by the present luminosity of Uranus $LU = 5.6 \times 10^{22} \text{ erg s}^{-1}$. Line colors represent the initial mole fraction of H_2O . We set 5-60 mol % of H_2O . The initial fraction of $\text{NH}_3/\text{H}_2\text{O} = 0.135$ and $\text{CH}_4/\text{H}_2\text{O} = 0.05675$. We assume $Z_{\text{tot}} = 0.8$, $Z_0 = 0.3$, and $Z_w = 0.5$. The equilibrium temperature is 58.2 K.

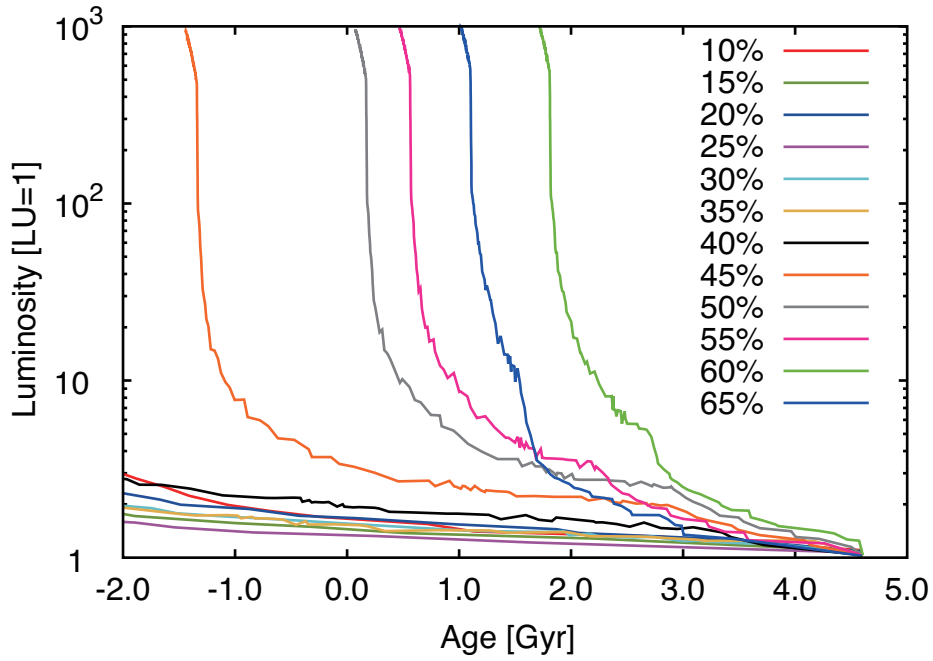


Figure 2.9: The time evolution of the planetary luminosity divided by the present luminosity of Uranus $LU = 5.6 \times 10^{22} \text{ erg s}^{-1}$. Line colors represent the initial mole fraction of H_2O . We set 10-65 mol % of H_2O . The initial fraction of $\text{NH}_3/\text{H}_2\text{O} = 0.135$ and $\text{CH}_4/\text{H}_2\text{O} = 0.05675$. We assume $Z_{\text{tot}} = 0.8$, $Z_0 = 0.3$, and $Z_w = 0.5$. The equilibrium temperature is 58.2 K. The evolutions is calculated backward from the age is 4.6×10^9 years.

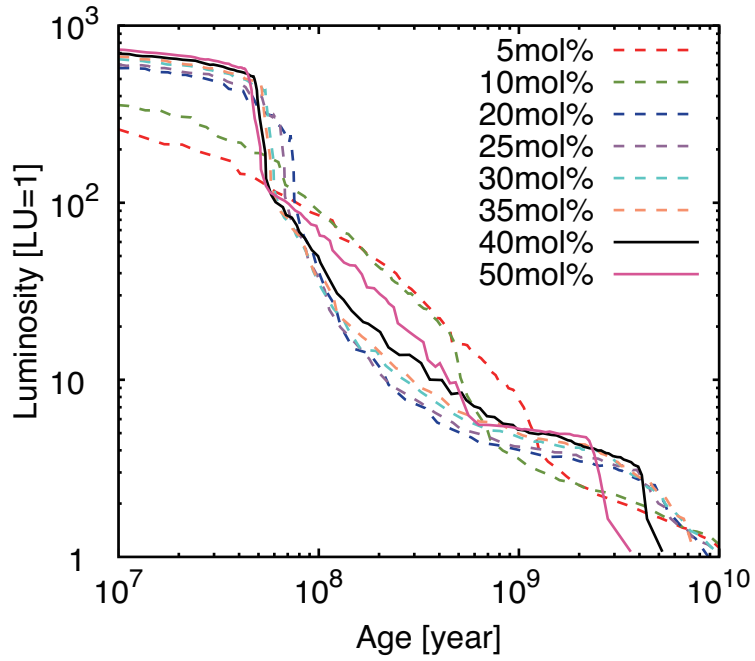


Figure 2.10: The time evolution of the planetary luminosity divided by the present luminosity of Uranus $LU = 5.6 \times 10^{22} \text{ erg s}^{-1}$. Line colors represent the initial mole fraction of H_2O . We set 5-50 mol % of H_2O . The initial fraction of $\text{NH}_3/\text{H}_2\text{O} = 0.135$ and $\text{CH}_4/\text{H}_2\text{O} = 0.05675$. We assume $Z_{\text{tot}} = 0.8$, $Z_0 = 0.3$, and $Z_w = 0.5$. The equilibrium temperature is 58.2 K.

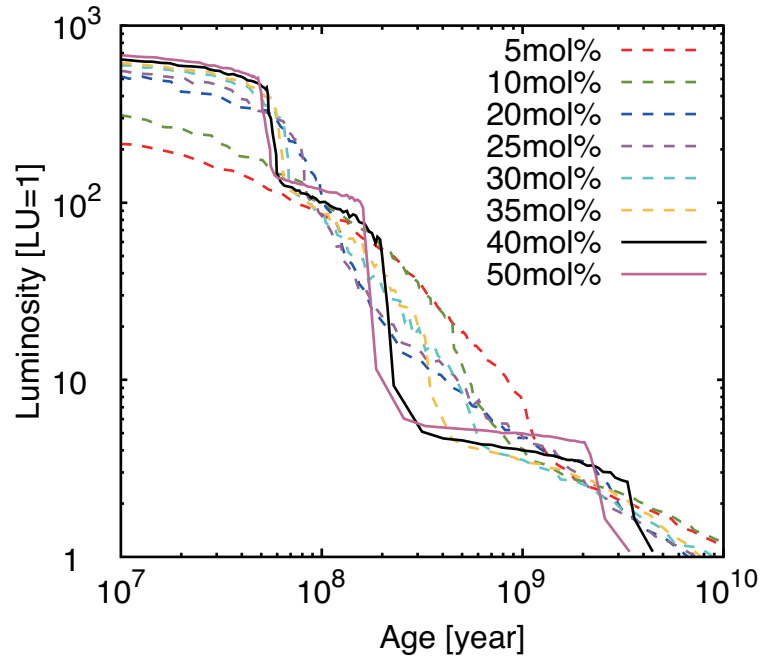


Figure 2.11: The time evolution of the planetary luminosity divided by the present luminosity of Uranus $LU = 5.6 \times 10^{22} \text{ erg s}^{-1}$. Line colors represent the initial mole fraction of H_2O . We set 5-60 mol % of H_2O . The initial fraction of $\text{NH}_3/\text{H}_2\text{O} = 0.135$ and $\text{CH}_4/\text{H}_2\text{O} = 0.05675$. We assume $Z_{\text{tot}} = 0.8$, $Z_0 = 0.3$, and $Z_w = 0.5$. The equilibrium temperature is 58.2 K.

F_{top} value depends on the molecular fraction of condensable species. As the condensable species increased, F_{top} also increased at the same bottom temperature. The upper limit of F_{top} is dominated by the temperature structure determined by the condensation of water, ammonia, and methane. If the atmospheric temperature structure is dominated by the condensation curve of water, ammonia, and methane, the temperature structure is fixed by the condensation curve and F_{top} is obeyed by that temperature structure.

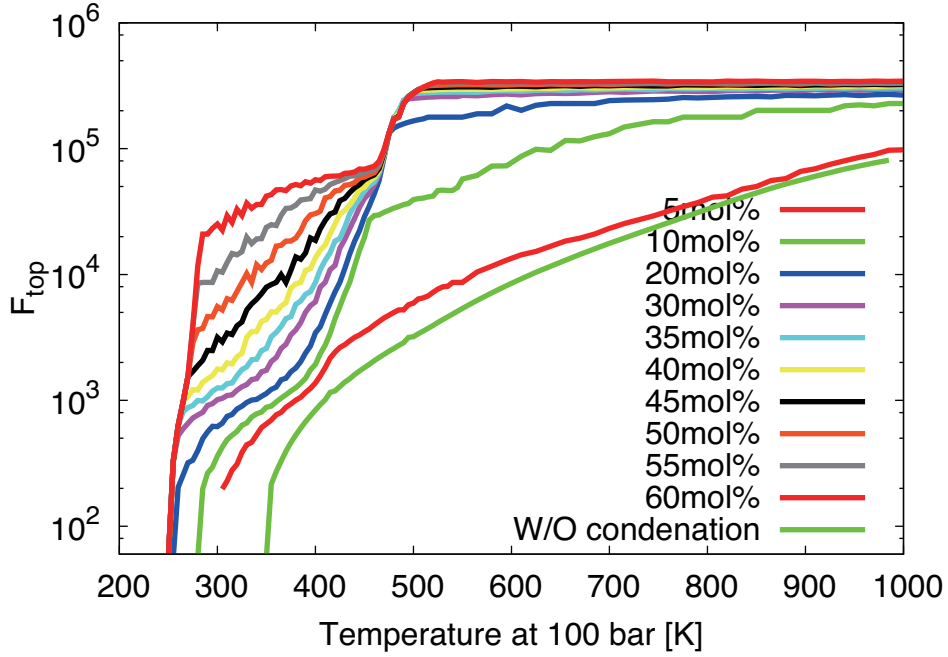


Figure 2.12: The relationship between the F_{top} and temperature at 100 bar. Line colors represent the initial mole fraction of H_2O . We set 5-50 mol % of H_2O . The initial fraction of $\text{NH}_3/\text{H}_2\text{O} = 0.458$ and $\text{CH}_4/\text{H}_2\text{O} = 0.05675$. We assume $Z_{\text{tot}} = 0.8$, $Z_0 = 0.3$, and $Z_w = 0.5$. The equilibrium temperature is 58.2 K

2.5 Discussion

In this subsection, we evaluate the validity of the assumptions and uncertainties of the model.

2.5.1 Validity of the assumptions I: the effect of the super-adiabatic lapse rate

We consider the effect of the super-adiabatic as the compositional gradient in the interior. That is, the temperature gradient in the interior is described as

$$\frac{d \ln T}{d \ln P} = \left(\frac{\partial \ln T}{\partial \ln P} \right)_{S,\mu} + \left(\frac{\partial \ln T}{\partial \ln S} \right)_{\mu,P} \frac{d \ln S}{d \ln P} + \left(\frac{\partial \ln T}{\partial \ln \mu} \right)_{P,S} \frac{d \ln \mu}{d \ln P}, \quad (2.56)$$

where T is the temperature, P is the pressure, S is the entropy, and μ is the mean molecular weight, respectively. Eq. (2.56) describes the true temperature gradient in the atmosphere considering the gradient of entropy and mean molecular weight.

A simple explanation for the super-adiabatic lapse rate is due to the compositional gradient, which is made by the condensation and sedimentation of condensable constituents. We assume that the entropy in the troposphere is constant and the thermodynamical properties is given from the ideal gas approximation. Then we can find Eq. (2.56) as

$$\frac{d \ln T}{d \ln P} = \left(\frac{\partial \ln T}{\partial \ln P} \right)_{S,\mu} + \frac{d \ln \mu}{d \ln P}. \quad (2.57)$$

However, the temperature gradient in the troposphere is determined by the efficiency of thermal transport by the convective motion. When the convection is not vigorous enough to transport the entropy from the deep interior, the temperature gradient in the troposphere cannot be described by the adiabatic lapse rate. Moreover, the thermal properties cannot be approximated by ideal gas in the high pressure region ($P \gtrsim 100$ bar). Thus, the non-ideal behavior for thermal properties of gas is also important near the bottom of the atmosphere. Since there are uncertainties to determine the super-adiabatic term, we deal with this term as a parameter and check its sensitivity of the evolutionary track of the ice giant. In this study, we evaluated the temperature gradient in the troposphere as

$$\frac{d \ln T}{d \ln P} = \left(\frac{\partial \ln T}{\partial \ln P} \right)_{S,\mu} + \delta \nabla, \quad (2.58)$$

where $\delta \nabla$ is the super-adiabatic gradient term. Fig. 2.13 shows the evolutionary track considering the super-adiabatic lapse rate. The red line is 0, the green line is 0.001, the

blue line is 0.01, and the purple line is 0.1. If the super-adiabatic term is less than 0.001, the impact on the thermal evolutionary track is small and the effect of super-adiabatic term cannot change our conclusions. On the other hand, if the super-adiabatic term is larger than 0.01, the thermal evolution timescale becomes long and then that effect changes our conclusions. If the compositional gradient is formed by the condensation curve, $\delta\nabla = 0.07 - 0.14$. Guillot (1995) indicated that the moist convection in ice giant's atmosphere was prevented when the atmosphere possessed too much ice constituents due to the compositional gradient. However, determining the lapse rate of super-adiabatic condition is required the two- or three-dimensional atmospheric circulation calculation considering the condensation, but that problem is beyond our study (Sugiyama et al., 2011, 2014).

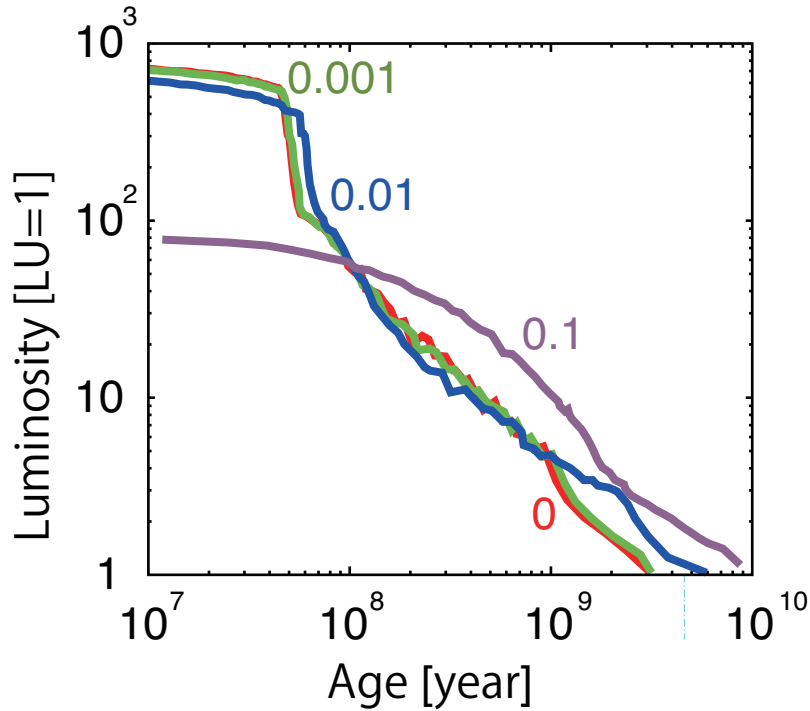


Figure 2.13: The time evolution of the planetary luminosity divided by the present luminosity of Uranus $LU = 5.6 \times 10^{22} \text{ erg s}^{-1}$. The red, green, blue, and purple lines are $\delta\nabla = 0, 0.001, 0.01,$ and 0.1 , respectively (see Eq. (2.58) for the definition of $\delta\nabla$). We set 70 mol % of H_2O , 9.45 mol % of NH_3 , and 3.97 mol % of CH_4 , respectively. We assume $Z_{\text{tot}} = 0.8$, $Z_0 = 0.3$, and $Z_w = 0.5$. The equilibrium temperature is 58.2 K.

2.5.2 Validity of the assumptions II: the effect of the cloud

In this study, we ignored the effect of clouds. When the condensation occurs in the atmosphere, clouds are also made but its radiative properties is quite uncertain. We evaluated the effect of clouds absorbing the infrared light. If the clouds absorb the infrared light, the atmosphere is warmed up. We evaluate the effect of clouds to multiple the infrared opacity by factor of 2 or 10. Fig. 2.14 shows the evolutionary track, considering enhanced infrared absorption. Uncertainties of clouds' radiative properties have non-negligible impact on the thermal evolution of ice giants. In this study, we only point out the importance of clouds, but more detailed studies would be required to understand the thermal evolution of ice giants.

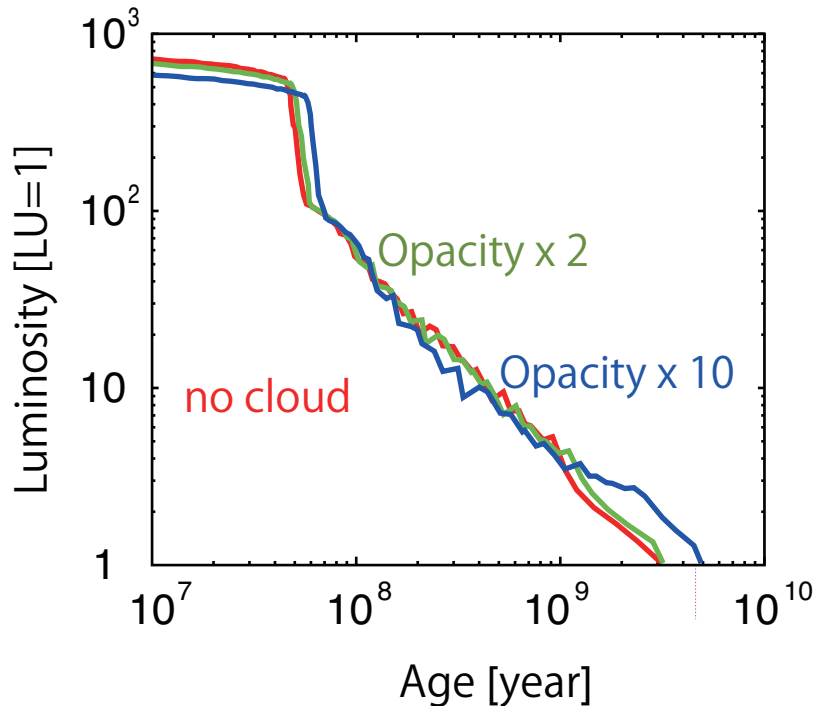


Figure 2.14: The time evolution of the planetary luminosity divided by the present luminosity of Uranus $LU = 5.6 \times 10^{22} \text{ erg s}^{-1}$. Line colors represent the difference of the effect of cloud. The red, green, blue, and purple lines are no cloud, $\kappa_{\text{th}} \times 2$, and $\kappa_{\text{th}} \times 10$, respectively, where κ_{th} is the infrared opacity of the atmosphere. We set 70 mol % of H_2O , 9.45 mol % of NH_3 , and 3.97 mol % of CH_4 , respectively. We assume $Z_{\text{tot}} = 0.8$, $Z_0 = 0.3$, and $Z_w = 0.5$. The equilibrium temperature is 58.2 K.

2.5.3 Validity of the assumptions III: comparison to the today's atmospheric compositions

The consistency between the theory and observations is important to discuss the validity of our study. We compare the results of atmospheric temperature-pressure structure when the planetary luminosity satisfies the present luminosity of Uranus. Fig. 2.15 shows the comparison between our calculation results and the observational data (Marley and McKay, 1999). We found that our results was consistent with the observation from 0.1 to several bars, which corresponded to the photosphere of infrared light. Since the temperature near the photosphere determines the outward flux from the top of the atmosphere, our assumption is valid enough to discuss the thermal evolution of the planet. The inconsistency of upper stratosphere is due to the photo-chemical reaction and multi-band effect, and that of deep troposphere is due to the abundance of methane.

2.5.4 Validity of the assumptions IV: the continuity between the interior and atmosphere

Above the results, there are inconsistency for the water content in the atmosphere and interior. Since we do not know the interaction between the atmosphere and interior clearly, we consider an assumption to take the consistency. Here we assumed for the consistency between planetary atmosphere and interior: The initial abundance of ice compositions in the atmosphere is determined by the initial abundance of water in the envelope. The abundance of water in the interior is determined by the initial abundance of water in the interior and the abundance is constant through the evolution. The initial abundance of water in the atmosphere is consistent with that in the interior and the abundance in the atmosphere changes through the evolution. This means that the mixing of condensable constituents in the envelope is strong enough to maintain the mass fraction for condensable constituents in the envelope during the evolution. The conversion relation between the mole fraction and mass fraction is

$$x_{\text{btm}} = \frac{Z_0}{\frac{\mu_W}{\mu_H}(1 - Z_0) + Z_0}, \quad (2.59)$$

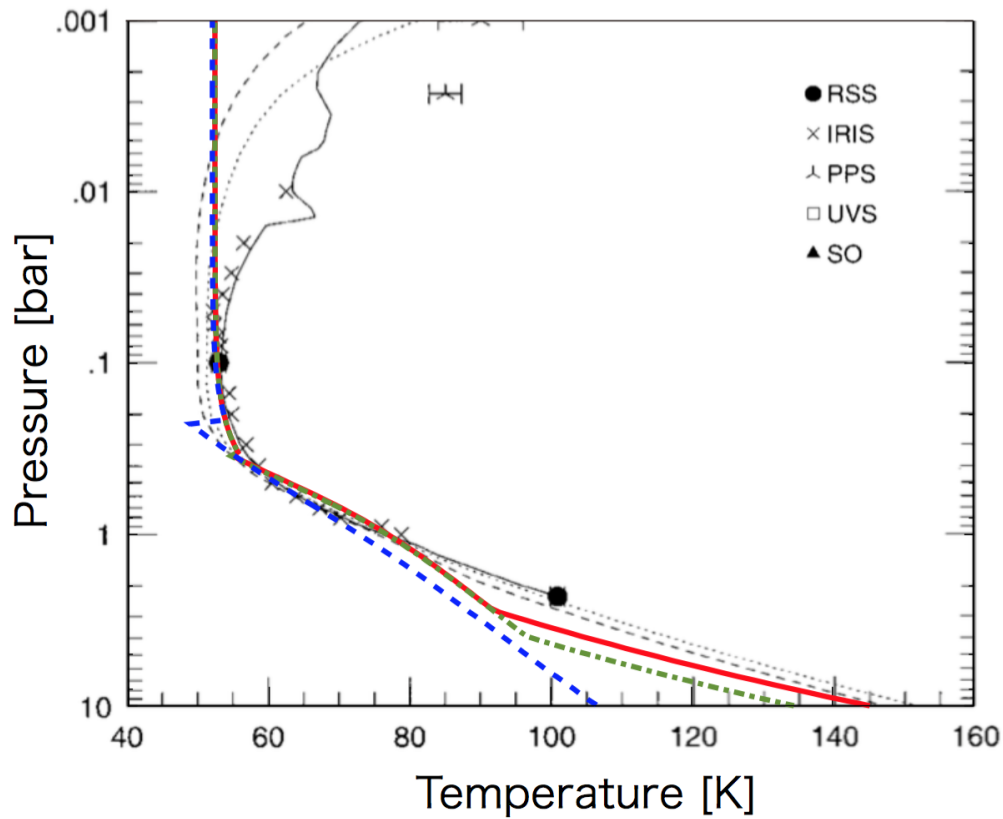


Figure 2.15: The temperature-pressure relation of atmosphere. Line colors represent the difference of the initial H_2O mole fraction. The red, green, and blue are 45 %, 50 %, and 55 %, respectively. The initial fraction of $\text{NH}_3/\text{H}_2\text{O}=0.05675$ and $\text{CH}_4/\text{H}_2\text{O}=0.135$. We assume $Z_{\text{tot}}=0.8$, $Z_0=0.3$, and $Z_w=0.5$. The equilibrium temperature is 58.2 K. The T-P profile and observational data are cited from Marley and McKay (1999).

where x_{btm} is the mole fraction of the ice (which includes H_2O , NH_3 , and CH_4), $\mu_W(= 18.0)$ is the molecular weight of the water, and $\mu_H(= 2.3)$ is the molecular weight of the hydrogen-helium, respectively. Table 2.5 shows the relationship between Z_0 and the mole fraction of ice x_{btm} . The abundance of water in the envelope is constant through the evolution. This assumption means that the mixing of condensable constituents in the envelope is strong enough to maintain the mass fraction of condensable constituents in the envelope through the evolution.

Z_0	0.023	0.05	0.1	0.2	0.3	0.4	0.5	0.6	0.7	0.8	0.9	0.95
x_{btm}	0.003	0.0067	0.013	0.03	0.05	0.078	0.11	0.16	0.23	0.34	0.53	0.71

Table 2.5: The relationship between the mass fraction of ice Z_0 and the mole fraction of ice x_{btm} .

Figure 2.16 shows the evolution of luminosity with the above values. The evolution of planetary radius is also showed in Fig. 2.17. We set parameters as Z_0 which represents the water mass fraction in the envelope. The initial total mole fraction of H_2O is also Z_0 . We set $Z_0 = 0.80, 0.85, 0.90, 0.95$ and $Z_w = 0.97$ (see also section 2.2.4). We assume $\text{CH}_4/\text{H}_2\text{O} = 0.458$ and $\text{NH}_3/\text{H}_2\text{O} = 0.135$, which is corresponding to the solar abundances. We cannot find the self consistent solution of both luminosity and radius of Uranus. When we want to keep a consistency with the present radius of Uranus, the atmosphere required too low initial mole fraction of volatiles to explain the present luminosity of Uranus.

To explain the present luminosity and radius of Uranus, $\text{CH}_4/\text{H}_2\text{O}$ and $\text{NH}_3/\text{H}_2\text{O}$ should be changed. We set $\text{CH}_4/\text{H}_2\text{O} = 0.05675$ and $\text{NH}_3/\text{H}_2\text{O} = 0.135$. We assume $Z_0 = 0.8, 0.85, 0.9, 0.95$ and $Z_w = 0.97$. Figure 2.18 shows the evolution of luminosity with these values. The evolution of planetary radius is also showed in Fig. 2.19. If we set $Z_0 \geq 0.95$, the planetary luminosity reached the present luminosity of Uranus within the age of the solar system. However, the planetary radius was smaller than the present radius of Uranus. Those results indicate that the transport of ice compositions in the planetary interior should be important as long as we assume the atmosphere of ice giants had a lot of ice compositions when it was formed. Our model required a large amount of condensable constituents in the envelope, The amount of condensable constituents in the envelope our model required was larger than that previous studies predicted. The mass fraction of heavy elements in the planet, was more than 0.85 (e.g. Nettelmann et al.

(2013); Helled et al. (2011)). However, the mass fraction of condensable constituents in the outer envelope should be smaller than the bulk mass fraction of heavy elements to explain the present radius of Uranus. During the evolution, condensable constituents in the atmosphere and envelope should be settle down and formed an ice mantle atop a solid core in the planet. That is, condensation of condensable constituents in the atmosphere and ice mantle formation in the deep interior of the planet occurred simultaneously. If the sedimentation of condensable constituents in the envelope occurred, the mean molecular weight of planetary envelope decreased and that affected the planetary radius. There are uncertainties of convective transport in the planetary interior and that will be important future work to reveal the origin and evolution of ice giants.

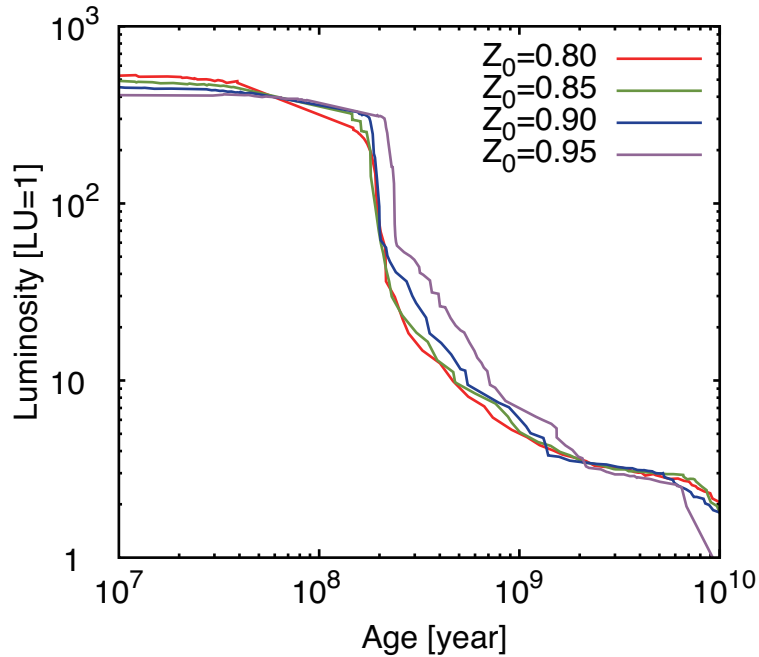


Figure 2.16: The time evolution of the planetary luminosity divided by the present luminosity of Uranus $LU = 5.6 \times 10^{22} \text{ erg s}^{-1}$. Line colors represent the initial mass fraction H_2O in the atmosphere and envelope. The initial fraction of $\text{NH}_3/\text{H}_2\text{O} = 0.458$ and $\text{CH}_4/\text{H}_2\text{O} = 0.135$. We assume $(Z_0, Z_{\text{tot}}) = (0.80, 0.81)$, $(0.85, 0.86)$, $(0.90, 0.91)$, and $(0.95, 0.96)$, respectively. We assume $Z_w = 0.97$ and Z_0 in the envelope is constant through the evolution. The equilibrium temperature is 58.2 K

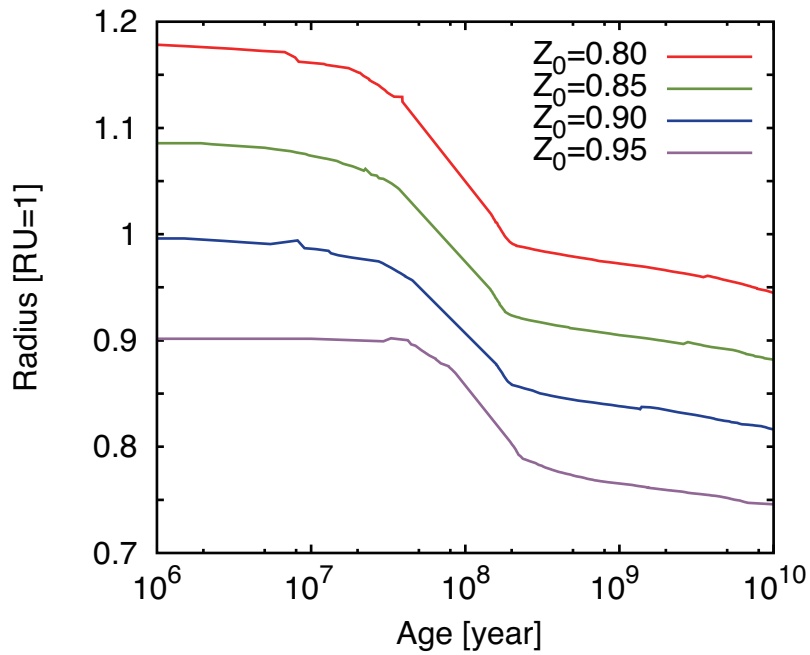


Figure 2.17: The time evolution of the planetary radius divided by the present radius of Uranus $RU = 4.01 R_{\oplus}$. Line colors represent the initial mass fraction H_2O in the atmosphere and envelope. The initial fraction of $NH_3/H_2O = 0.458$ and $CH_4/H_2O = 0.135$. We assume $(Z_0, Z_{tot}) = (0.80, 0.81)$, $(0.85, 0.86)$, $(0.90, 0.91)$, and $(0.95, 0.96)$, respectively. We assume $Z_w = 0.97$ and Z_0 in the envelope is constant through the evolution. The equilibrium temperature is 58.2 K.

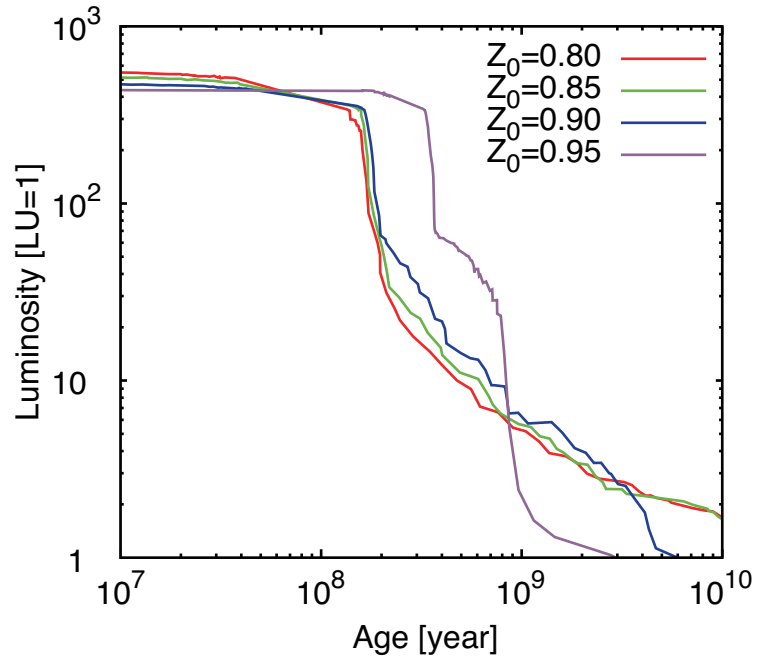


Figure 2.18: The time evolution of the planetary luminosity divided by the present luminosity of Uranus $LU = 5.6 \times 10^{22} \text{ erg s}^{-1}$. Line colors represent the initial mass fraction H_2O in the atmosphere and envelope. The initial fraction of $\text{NH}_3/\text{H}_2\text{O} = 0.05675$ and $\text{CH}_4/\text{H}_2\text{O} = 0.135$. We assume $(Z_0, Z_{\text{tot}}) = (0.80, 0.81)$, $(0.85, 0.86)$, $(0.90, 0.91)$, and $(0.95, 0.96)$, respectively. We assume $Z_w = 0.97$ and Z_0 in the envelope is constant through the evolution. The equilibrium temperature is 58.2 K.

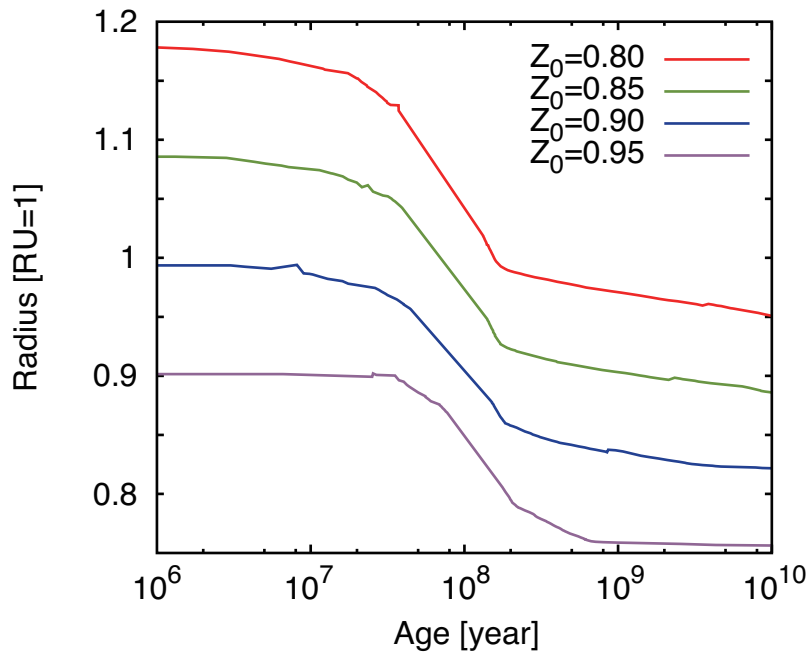


Figure 2.19: The time evolution of the planetary radius divided by the present radius of Uranus $RU = 4.01 R_{\oplus}$. Line colors represent the initial mass fraction H_2O in the atmosphere and envelope. The initial fraction of $NH_3/H_2O = 0.05675$ and $CH_4/H_2O = 0.135$. We assume $(Z_0, Z_{tot}) = (0.80, 0.81)$, $(0.85, 0.86)$, $(0.90, 0.91)$, and $(0.95, 0.96)$, respectively. We assume $Z_w = 0.97$ and Z_0 in the envelope is constant through the evolution. The equilibrium temperature is 58.2 K.

2.5.5 Validity of the assumptions V: the model of the atmosphere

The latent heat has dependence on temperature, but in this study we do not include that effect. The dependence on temperature of the latent heat, however, does not have significant effect on the thermal evolution qualitatively. Since the radiation from the top of the atmosphere is determined by the height where the optical thickness is unity, the non-ideal effect of the condensable constituents, which is important in the high pressure and high temperature region, is not important.

We also assumed that the bottom of the atmosphere is 100 bars. Below 100 bars, the condensable constituents behave as supercritical fluids. Since the critical pressures of water, ammonia, and methane are 217.6 bars, 111.3 bars, and 45.4 bars respectively (Reid et al., 1987), the assumption does not affect the result qualitatively for the same reason of the dependence on the temperature of the latent heat.

2.5.6 The evolution of Neptune

We show the thermal evolution of Neptune. We try to find the evolutionary pass of Neptune and discuss the difference between the Uranus and Neptune. The evolution of Neptune is also solved by Fortney et al. (2011) and Nettelmann et al. (2013).

We set the equilibrium temperature 46.6 K, the present luminosity of Neptune 5.3×10^{22} erg s⁻¹ (Pearl and Conrath, 1991), and planetary mass Neptune mass $M_N = 1.02 \times 10^{29}$ g. We assumed NH₃/H₂O= 0.135 and CH₃/H₂O= 0.458 which are equal to the solar value of N/O and C/O, respectively. We adjust Z_0, Z_{tot} and Z_w to satisfy the present radius of Neptune $R_N = 2.48 \times 10^9$ cm at the age of 5 giga years. We summarize the parameters as described in Table 2.6.

Temperature	Mass	Radius	NH ₃ /H ₂ O	CH ₃ /H ₂ O
46.6 K	M_N	R_N	0.135	0.458

Table 2.6: Parameter sets we assumed in the calculation.

Fig. 2.20 and Fig. 2.21 show the time evolution of the planetary radius and luminosity, respectively. We found that the too much Z_0 could not explain the present luminosity of

Neptune because of the condensation of methane. If we set $Z_0 = 0.7$, the mole fraction of methane at 5 giga years was larger than the that predicted by the observation of Neptune atmosphere (Bishop et al., 1995). Our model suggests that $Z_0 \leq 0.5$ is good agreement with the present luminosity and radius of Neptune. We conclude that the envelope of Neptune is less polluted by ice compositions compared to Uranus.

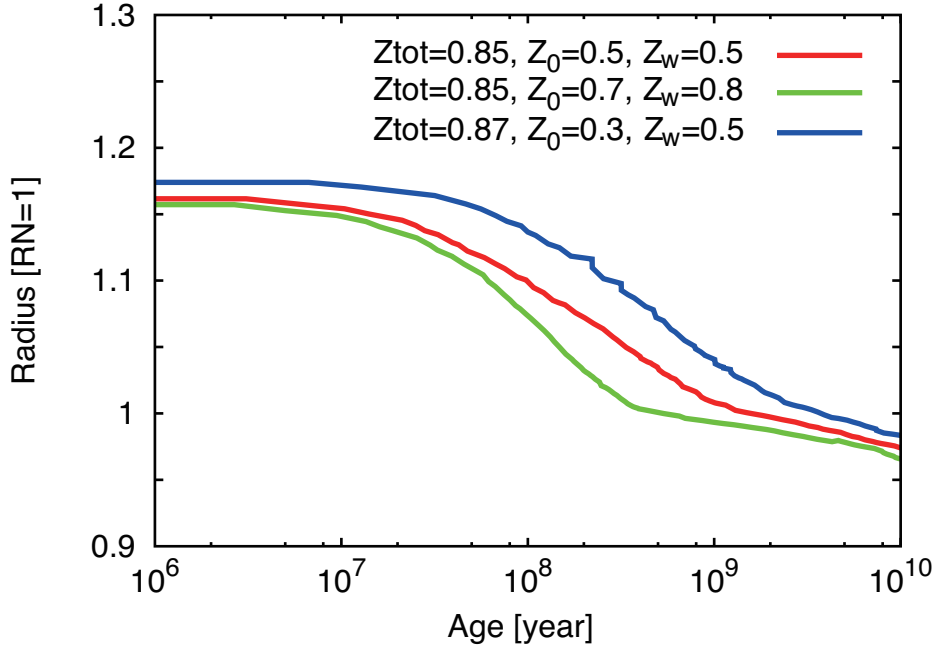


Figure 2.20: The time evolution of the planetary radius divided by the present radius of Neptune $RN = 3.89 R_{\oplus}$. The initial fraction of $\text{NH}_3/\text{H}_2\text{O} = 0.458$ and $\text{CH}_4/\text{H}_2\text{O} = 0.135$. Lines' colors represent the parameters of Z_0, Z_{tot} and Z_w . The red, green, and blue represent $(Z_0, Z_{\text{tot}}, Z_w) = (0.5, 0.85, 0.5)$, $(0.7, 0.85, 0.8)$, and $(0.3, 0.87, 0.5)$, respectively. We assume Z_0 in the envelope is constant through the evolution. The equilibrium temperature is 46.6 K.

2.5.7 Implications for the origin of Uranus

Our results suggest that the atmosphere of Uranus had been polluted by condensable constituents when it was formed to explain the present luminosity of Uranus. Here we compare ideas to explain the present luminosity of Uranus. Stevenson (1986) showed that the present luminosity of Uranus could be explained when the giant impact event provided the impact energy in the deep interior (hereafter the impact-heated model). Stevenson (1986) assumed that the deep interior of Uranus was stably stratified when Uranus was

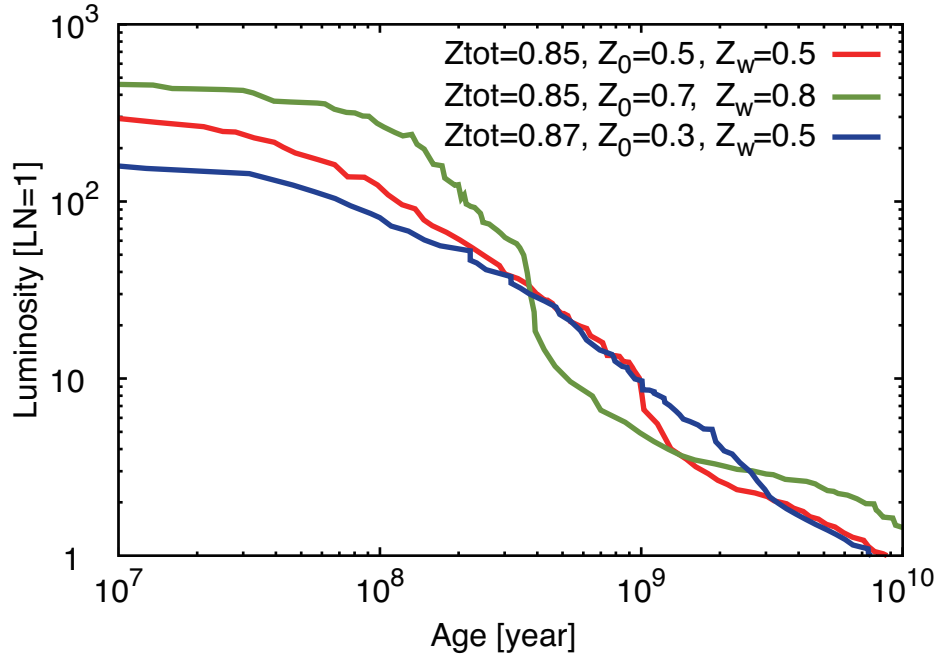


Figure 2.21: The time evolution of the planetary luminosity divided by the present luminosity of Neptune $LN = 5.3 \times 10^{22} \text{erg s}^{-1}$. The initial fraction of $\text{NH}_3/\text{H}_2\text{O} = 0.458$ and $\text{CH}_4/\text{H}_2\text{O} = 0.135$. Lines' colors represent the parameters of Z_0, Z_{tot} . The red, green, and blue represent $(Z_0, Z_{\text{tot}}, Z_w) = (0.5, 0.85, 0.5), (0.7, 0.85, 0.8),$ and $(0.3, 0.87, 0.5)$, respectively. We assume Z_0 in the envelope is constant through the evolution. The equilibrium temperature is 46.6 K.

formed gradually from small bodies. The interior of Uranus was difficult to sustain adiabatic, homogeneous interior because the compositionally stratified interior prevent the convective motion in the deep interior. Thus the idea required that one-thirds of the mass (i.e. outer region of Uranus) should significantly heated by the impact event (Stevenson, 1986). The giant impact event also affects the rotation axis of Uranus. Accordingly, this idea also explain the difference of not only the present luminosity but also the spin axes of Uranus and Neptune. To satisfy the condition, the oblique impact occurred when the Uranus was formed. However, this impact-heating model requires strict condition for the impact parameter. Morbidelli et al. (2012) suggested that one impact event could not explain the Uranus's tilted rotation axis. They argue that Uranus should have experienced at least two impact events. To satisfy that condition, the impact-heated model requires only oblique impacts. Moreover, the impact-heated model ignore the contribution of the inner region of Uranus on the thermal evolution. Thus, the thermal transport between the outer and inner regions should be prevented. This idea requires that the Uranus did not have fully convective interior but a stable stratified interior. During the accretion phase, the interior of the proto-uranus was fully convective (Bodenheimer and Pollack, 1986; Pollack et al., 1996). Thus, the initial condition of Uranus which this idea required is difficult to satisfy from the point of view of the formation scenario. To ignore the contribution of thermal transport from the deep interior, an inhibition of the convective transport due to a compositional gradient is realistic.

The effect of a composition gradient is important to discuss the efficiency of thermal transport via convection. Hydrodynamical simulations indicated that the layered convection occurred due to the compositional gradient (Radko, 2003; Rosenblum et al., 2011; Mirouh et al., 2012; Wood et al., 2013). The impact of the layered convection on the thermal evolution was calculated for gas giants (Vazan et al., 2015; Kurokawa and Inutsuka, 2015; Nettelmann et al., 2015) but not calculated for ice giants. The effect of the compositional gradient on the thermal evolution is also important to explain the present luminosity of Uranus. Nettelmann et al. (2013) showed that the contribution of 45 % of the mass of Uranus on thermal evolution needed to be ignored to explain the present luminosity of Uranus. Thus, the thermal transport between the outer and inner regions should be prevented. To prevent the thermal transport, the convective transport

between the inner and outer regions should be suppressed. This suggests that there are a compositional gradient between the inner and outer regions to suppress the convective transport (Podolak et al., 1991; Nettelmann et al., 2013). To verify this idea, we should discuss the thermal transport via convection considering a compositional gradient. However, the layered convection is unstable for the large-scale-overturning convection (Vazan et al., 2015; Kurokawa and Inutsuka, 2015). If the compositional inhomogeneity disappears, the planetary interior should be compositional homogeneity and the heat transport via convection is not prevented.

Our results show that to explain the current luminosity, the atmosphere of Uranus is required to have been polluted by water, ammonia, and methane when it was formed. Moreover, the atmosphere of Uranus immediately after the formation should have had both the C/O value lower than the solar composition and the N/O value higher than the solar composition. These are consistent with the observations of the current atmosphere of Uranus. Atmospheric observations (Orton et al., 2014a,b) indicated that the present atmosphere of Uranus is not polluted by H₂O or NH₃. This apparently seems inconsistent with our conclusions; nevertheless, these species should have been condensed and removed from the atmosphere. Thereby, the fact that the current atmosphere is not polluted by H₂O and NH₃ is consistent with our conclusions. Encrenaz et al. (2004) first detected CO molecule in the atmosphere of Uranus using the ISAAC imaging spectrometer at the VLT-UTI (ANTU) 8-m telescope of European Southern Observatory. Based on Herschel-HIFI observations, Orton et al. (2014b) constrain the CO content in the stratosphere of Uranus as $7.1 - 9.0 \times 10^{-9}$ in a mole fraction. They found that CO was of an internal origin because their thermochemical model showed an upper limit of a mole fraction of 2.1×10^{-9} . Their calculation results also suggested that C/H was 13-40 times the solar composition while O/H was 340-500 times the solar composition (Cavalié et al., 2014). Thus, the C/O value value of the present atmosphere of Uranus is estimated between 0.01 and 0.05, which is smaller than solar C/O value. Since our results show that the C/O value less than 0.05 is required to explain the current luminosity, our conclusions agree with the observation of the atmosphere. Our conclusions show that the atmosphere should contain less CH₄ compared with H₂O given the solar compositions. This in turn means that the major C-bearing molecule in the Uranus-forming region in the protoplanetary

disk would have been CO. If the disk temperature at the Uranus-forming region was low sufficient to condense CO into the solid phase (20 K or less; Alibert and Mousis (2007)), CO should have been present in the current atmosphere. The observations, however, show that the CO content is as low as $(7.1 - 9.0) \times 10^{-9}$ (Orton et al., 2014b). Thus, this imply that the disk temperature at the Uranus-forming region would have been higher than the condensation temperature of CO but allows H₂O, CH₄, and NH₃ to condense into the solid phase, namely 20-50 K (Alibert and Mousis, 2007).

If planet experienced a giant impact event, the planetary interior would be mixed due to the shock wave through the interior (Slattery, 1992). If the Uranus experienced the giant impact event, the atmosphere also mixed with ice compositions from the interior. Slattery (1992) calculated the giant impact of primitive Uranus using smooth particle hydrodynamical simulation. They suggested that the large obliquity of Uranus is due to the giant impact. Morbidelli et al. (2012) suggested that Uranus was not tilted from 0° to 98° in one shot. They indicated that Uranus experienced at least two giant collisions. The obliquity of Uranus cannot be explained due to the tidal interaction with the satellites. That is because the required mass of satellite becomes greater than the total mass of Uranian satellites to explain the large Uranian obliquity within the age of the solar system (Kubo-Oka and Nakazawa, 1995; Boué and Laskar, 2010). That is, giant impact events are consistent with the obliquity of Uranus. On the other hand, the thermal evolution of Neptune does not need the effect of condensation (Fortney et al., 2011; Nettelmann et al., 2013). We argue that giant impact events make the difference of present luminosities between Uranus and Neptune.

2.6 Conclusions

We calculated the thermal evolution of ice giant considering the effect of condensation of water, ammonia, and methane in the planetary atmosphere. We found that the thermal evolution timescale with the effect of condensation in the atmosphere was shortened compared to that without the effect because the latent heat due to the condensation in the atmosphere raised the atmospheric temperature and increased the outward flux from the top of the atmosphere F_{top} . We also found that the amount of condensable constituents

(water, ammonia, and methane in our calculation) in the atmosphere controlled the thermal evolution of the ice giants. If the ice giant has large amount of condensable species, the thermal evolution timescale is controlled by a radiation limit of water, ammonia, and methane. Then the thermal evolution timescale with condensation effect is shorter than that without the condensation. The initial fractions of $\text{NH}_3/\text{H}_2\text{O}$ and $\text{CH}_4/\text{H}_2\text{O}$ are also important. A large fraction of $\text{NH}_3/\text{H}_2\text{O}$ causes the rapid thermal evolution due to the effect of the condensation of NH_3 , while large fraction of $\text{CH}_4/\text{H}_2\text{O}$ prevents the cooling of Uranus. Our study indicated that large fraction $\text{NH}_3/\text{H}_2\text{O}$ and small fraction of $\text{CH}_4/\text{H}_2\text{O}$ is suitable to explain the present luminosity of Uranus. The present planetary luminosity and compositions imply the initial contents of condensable constituents in the atmosphere that reflects the formation history of the planet. Our result will be useful to connect the formation scenario and observations of the ice giants.

Chapter 3

Effect of photo-evaporative mass loss on masses and radii of ice giants

3.1 Introduction

Exoplanet transit photometry reveal the interior and atmosphere of exoplanets. The most important advantage of this technique would be that planetary radii are measured, while planetary masses are measured via other techniques such as the radial velocity method and the transit timing variation method. Relationships of measured mass and radius allow us to infer the interior structure and bulk composition of exoplanets theoretically, which brings crucial constraints to the formation and evolution processes of the planets. A growing number of exoplanets with radii of 1 to 2 Earth radius ($= 6.38 \times 10^8$ cm) has been identified, which are often called super-Earths (Batalha et al., 2013). We can thus discuss the compositions of such small planets in addition to gas giants by comparing theory with observation nowadays.

Transiting super-Earths detected so far show a large variation in radius, suggesting diversity in composition. There are many theoretical studies on mass-radius relationships for planets with various compositions and masses (Valencia et al., 2007; Fortney et al., 2007; Sotin et al., 2007; Seager et al., 2007; Grasset et al., 2009; Wagner et al., 2011; Swift et al., 2012). A recent important finding by comparison between theory and observation is that there are a significant number of low-density super-Earths that are larger in size than they would be if they were rocky. This implies that these transiting super-Earths have

components less dense than rock. From a viewpoint of planet formation, the possible components are hydrogen-rich (hereafter H-rich) gas and water which make an outer envelope. A small fraction of H-rich gas or water is known to be enough to account for observed radii of the low-density super-Earths (Adams et al., 2008; Valencia et al., 2010).

The stability of the envelopes are, however, to be investigated. Transiting planets are in general orbiting close to their host stars (typically $\lesssim 0.1$ AU), because detection probability of planetary transits is inversely proportional to the separation (e.g., Kane 2007). Such close-in planets are highly irradiated and exposed to intense X-ray and ultraviolet radiation (hereafter XUV) coming from their host stars. This causes the planetary envelope to escape hydrodynamically from the planet (e.g., Watson et al. 1981). This process is often called the photoevaporation of planetary envelopes. As for massive close-in planets, namely, hot Jupiters, the possibility of the photoevaporation and its outcome have been investigated well both theoretically and observationally (e.g., Yelle et al. 2008 and references therein).

While the photoevaporation may not affect the evolution and final composition of hot Jupiters significantly except for extremely irradiated or inflated hot Jupiters, its impact on small close-in planets in the sub/super-Earth mass range should be large, partly because their envelope masses are much smaller than those of hot Jupiters (Owen and Wu, 2013; Lopez and Fortney, 2013; Kurokawa and Nakamoto, 2014). For example, the structure and composition of the first transiting super-Earth CoRoT-7 b are investigated by Valencia et al. (2010). They discussed the sustainability of the possible hydrogen-helium (hereafter H+He) envelope with mass of less than 0.01 % of the total planetary mass. The envelope mass was consistent with its measured mass and radius. However, the estimated lifetime of the H+He envelope was only 1 million years, which was much shorter than the host star's age ($2 - 3 \times 10^9$ years). This suggests that CoRoT-7 b is unlikely to possess the H+He envelope at present.

Young main-sequence stars are known to be much more active, and emit stronger XUV than the current Sun (e.g., Ribas et al. 2005). Therefore, even if a super-Earth had a primordial atmosphere initially, it may lose the atmosphere completely during its history. Such discussions concerning the photo-evaporative loss of H+He envelopes were done for GJ 1214 b (Nettelmann et al., 2011; Valencia et al., 2013) and super-Earths orbiting

Kepler-11 (Lopez et al., 2012; Ikoma and Hori, 2012), in addition to CoRoT-7 b (Valencia et al., 2010). Systematic studies were also done by Rogers et al. (2011) and Lopez and Fortney (2013). Those studies demonstrated the large impact of the photoevaporation on the stability of H+He envelopes for super-Earths. In particular, Lopez and Fortney (2013) performed simulations of coupled thermal contraction and photo-evaporative mass loss of rocky super-Earths with H+He envelopes. They found that there were threshold values of planetary masses and radii, below which H+He envelopes were completely stripped off.

In this study, we focus on ice giants which are close to their host star. Planet formation theories predict that low-mass planets migrate toward their host star, which is strongly supported by the presence of many close-in ice giants, from cooler regions (e.g., Ward 1986), where they may have accreted a significant amount of water. This suggests that ice giants may also exist close to host stars. Therefore, similar discussions should be done for water envelopes of close-in super-Earths. However, there are just a few studies, which treat specific sub/super-Earths such as CoRoT-7 b (Valencia et al., 2010) and Kepler-11 b (Lopez et al., 2012). No systematic study is yet to be done for the stability of water envelopes.

The aim of this study is to examine the stability of primordial water envelopes of close-in ice giants against photo-evaporation. The thermal evolution of planets with significant fractions of water envelopes (i.e., water-worlds), incorporating the effect of stellar-XUV-driven photo-evaporative mass loss is simulated. The theoretical model is described in § 3.2. As for the atmosphere model, the details are described in Appendix F. In § 3.3, we show the evolutionary behavior of the water-rich planets. Then, we find threshold values of planetary masses and radii below which such water-rich planets are incapable of retaining primordial water envelopes for a period similar to ages of known exoplanet-host stars (i.e., 1–10 Gyr). In § 3.4, we compare the theoretical mass-radius distribution of water-rich planets with that of known transiting planets. Furthermore, we compare the threshold radius with sizes of Kepler objects of interest (KOIs) to suggest that KOIs include a significant number of rocky planets. Finally we summarize this chapter in § 3.5.

3.2 Numerical models

In this study, the evolution of the mass and radius of a planet which is composed of water and rock, including the mass loss due to photoevaporation is calculated. Figure 3.1 shows the interior model. We assumed that the planet consist of three layers in spherical symmetry and hydrostatic equilibrium; namely, from top to bottom, a water vapor atmosphere, a water envelope and a rocky core. At each interface, the pressure and temperature are continuous.

The assumptions and equations which determine the planet’s interior structure and thermal evolution are described in § 3.2.1 and § 3.2.2, respectively. The equations of state for the constituents in the three layers are summarized in § 3.2.3. The structure of the atmosphere and the photoevaporative mass loss, both of which govern the planet’s overall evolution, are described in § 3.2.4 (see also Appendix F) and § 3.2.5, respectively. Since a goal of this study is to compare our theoretical prediction with results from transit observations, we also calculate the transit radius, which is defined in § 3.2.6. Finally, we summarize our numerical procedure in § 3.2.7.

3.2.1 Interior structure

The interior structure of the planet is determined by the differential equations (e.g. Kippenhahn and Weigert 1990),

$$\frac{\partial P}{\partial M_r} = -\frac{GM_r}{4\pi r^4}, \quad (3.1)$$

$$\frac{\partial r}{\partial M_r} = \frac{1}{4\pi r^2 \rho}, \quad (3.2)$$

$$\frac{\partial T}{\partial M_r} = -\frac{GM_r T}{4\pi r^4 P} \nabla, \quad (3.3)$$

and the equation of state,

$$\rho = \rho(P, T), \quad (3.4)$$

where r is the planetocentric distance, M_r is the mass contained in the sphere with radius of r , P is the pressure, ρ is the density, T is the temperature and G ($= 6.67 \times$

$10^{-8} \text{ dyne cm}^2 \text{ g}^{-2}$) is the gravitational constant. The symbol ∇ is the temperature gradient with respect to pressure. We assume that the water envelope and rocky core are fully convective and the convection is vigorous enough that the entropy S is constant; namely,

$$\nabla = \left(\frac{\partial \ln T}{\partial \ln P} \right)_S. \quad (3.5)$$

Equations (3.1), (3.2) and (3.3) require three boundary conditions. Three boundary conditions are required by Eqs. (3.1), (3.2) and (3.3). We set the inner one $r = 0$ at $M_r = 0$. The outer boundary corresponds to the interface between the envelope and the atmosphere, which is called the tropopause. The tropopause pressure P_{ad} and temperature T_{ad} are determined from the atmospheric model, the details of which is described in § 3.2.4 and Appendix A. The atmospheric mass is negligible, relative to the planet total mass M_p . In our calculation, the atmospheric mass is less than 0.1 % of the planetary mass. Thus, the outer boundary conditions are given as

$$P = P_{\text{ad}} \quad \text{and} \quad T = T_{\text{ad}} \quad \text{at} \quad M_r = M_p. \quad (3.6)$$

As mentioned above, the pressure and temperature are also continuous at the interface between the water envelope and the rocky core.

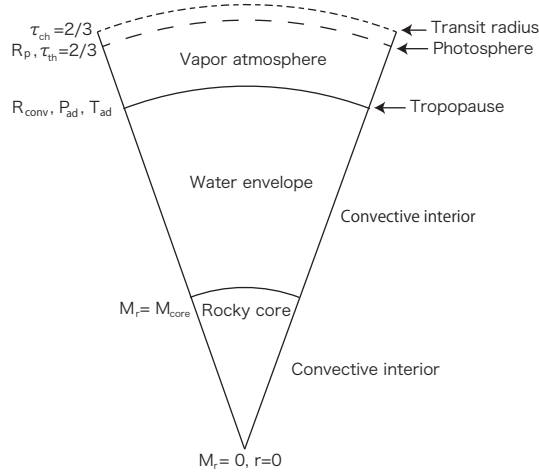


Figure 3.1: Model of the planetary structure in this study.

3.2.2 Thermal evolution

The thermal evolution of the planet without internal energy generation is described by (e.g., Kippenhahn and Weigert 1990)

$$\frac{\partial L}{\partial M_r} = -T \frac{\partial S}{\partial t}, \quad (3.7)$$

where L is the intrinsic energy flux passing through the spherical surface with radius of r , S is the specific entropy, and t is time. Since the entropy is constant in each layer, the integrated form of Eq. (3.7) is written as

$$-L_p = \frac{\partial \bar{S}_e}{\partial t} \int_{M_c}^{M_p} T dM_r + \frac{\partial \bar{S}_c}{\partial t} \int_0^{M_c} T dM_r, \quad (3.8)$$

where L_p is the total intrinsic luminosity of the planet and M_c is the mass of the rocky core, and \bar{S}_e and \bar{S}_c are the specific entropies in the water envelope and the rocky core, respectively. In integrating Eq. (3.7), we have assumed $L = 0$ at $M_r = 0$.

In the numerical calculations of this study, we use the intrinsic temperature T_{int} , instead of L_p , which is defined by

$$T_{\text{int}}^4 \equiv \frac{L_p}{4\pi R_p^2 \sigma}, \quad (3.9)$$

where R_p is the planet photospheric radius (see § 3.2.4 for the definition) and σ is the Stefan-Boltzmann constant ($= 5.67 \times 10^{-5} \text{ erg cm}^{-2} \text{ K}^{-4} \text{ s}^{-1}$).

3.2.3 Equation of state (EOS)

In the vapor atmosphere, the temperature and pressure are sufficiently high and low, respectively, so that the ideal gas approximation is valid. We thus adopt the ideal equation of state, incorporating the effects of dissociation of H_2O . In practice, we use the numerical code developed by Hori and Ikoma (2011), which calculate chemical equilibrium compositions among H_2O , H_2 , O_2 , H , O , H^+ , O^+ and e^- .

Since pressure due to molecular interaction is not negligible, the ideal gas approximation is not valid at high pressures in the water envelope. In this study, we use mainly the

ab initio EOS for H₂O, H₂O-REOS (French et al., 2009). H₂O-REOS covers a density range from 1.0×10^{-6} g cm⁻³ to 15 g cm⁻³ and a temperature range from 1.0×10^3 K to 2.4×10^4 K. For T and ρ outside the ranges that H₂O-REOS covers, we use SESAME 7150 (Lyon and Johnson, 1992).

The rocky core is assumed to be mineralogically the same in composition as the silicate Earth. We adopt a widely-used EOS, the Vinet EOS, and calculate thermodynamic quantities following Valencia et al. (2007).

3.2.4 Atmospheric model

As described above, we consider an irradiated, radiative-equilibrium atmosphere on top of the water envelope. The thermal properties of the atmosphere govern the internal structure and evolution of the planet. To integrate the atmospheric structure, we follow the prescription developed by Guillot (2010) basically, except for the treatment of the opacity. Namely, we consider a semi-grey, plane-parallel atmosphere in local thermal equilibrium. The wavelength domains of the incoming (stellar) and outgoing (planetary) radiations are assumed to be completely separated; the former is visible, while the latter is near or mid infrared.

We solve the equation of radiative transfer by integrating the two sets (for incoming and outgoing radiations) of the zeroth and first-order moment equations for radiation with the Eddington’s closure relation: the incoming and outgoing radiations are linked through the equation of radiative equilibrium (see Appendix F). Guillot (2010) derived an analytical, approximate solution which reproduced well the atmospheric structure from detailed numerical simulations of hot Jupiters (see also Hansen (2008)). The solution depends on the opacities in the visible and thermal wavelengths. Guillot (2010) also presented empirical formulae for the mean opacities of solar-composition (i.e., hydrogen-dominated) gas.

However, no empirical formula is available for opacities of water vapor of interest in this study. We take into account the dependence of the water-vapor opacity on temperature and pressure, and integrate the momentum equations numerically. The details about the mean opacities and momentum equations are described in Appendix E.

The bottom of the atmosphere is assumed to be the interface between the radiative

and convective zones. We use the Schwarzschild criterion (e.g., see Kippenhahn and Weigert 1990) to determine the interface. The pressure and temperature at the interface ($P_{\text{ad}}, T_{\text{ad}}$) are used as the outer boundary conditions for the structure of the convective water envelope.

The photospheric radius R_p used in Eq. (3.9) is the radius where the thermal optical depth measured from infinity, τ , is $2/3$, namely,

$$\tau = \int_{R_p}^{\infty} \kappa_{\text{th}}^r \rho dr = \frac{2}{3}, \quad (3.10)$$

where κ_{th}^r is the Rosseland mean opacity for the outgoing radiation (see Appendix A for the definition). This level is above the tropopause, the radius of which is written by R_{conv} (see Fig.3.1). We evaluate the atmospheric thickness z ($= R_p - R_{\text{conv}}$) by integrating the hydrostatic equation from $P = P_{\text{ad}}$ to $P = P_{\text{ph}}$, namely

$$z = - \int_{P_{\text{ad}}}^{P_{\text{ph}}} \frac{dP}{g\rho} = - \int_{P_{\text{ad}}}^{P_{\text{ph}}} \frac{\mathcal{R} T}{\mu g P} dP, \quad (3.11)$$

where g is the constant gravity, \mathcal{R} ($= 8.31 \times 10^7 \text{ erg K}^{-1} \text{ g}^{-1}$) is the gas constant and μ is the mean molecular weight. P_{ph} is the photospheric pressure that we calculate by integrating

$$\frac{dP}{d\tau} = \frac{g}{\kappa_{\text{th}}^r} \quad (3.12)$$

from $\tau = 0$ to $2/3$.

3.2.5 Mass loss

The mass loss is assumed to occur in an energy-limited fashion. Its rate, including the effect of the Roche lobe, is given by (Erkaev et al., 2007)

$$\dot{M} = - \frac{\varepsilon F_{\text{XUV}} R_p \pi R_{\text{XUV}}^2}{GM_p K_{\text{tide}}}, \quad (3.13)$$

where ε is the heating efficiency, defined as the ratio of the rate of heating that results in hydrodynamic escape to that of stellar energy absorption, F_{XUV} is the incident flux of X-ray and UV radiation from the host star, K_{tide} is the potential energy reduction

factor due to stellar tide and R_{XUV} is the effective radius at which the planet receives the incident XUV flux. In Eq. (3.13), we have assumed $R_{\text{XUV}} = R_p$, which is a good approximation for close-in planets of interest (Lammer et al., 2013). It is noted that Lammer et al. (2013) focused on the hydrogen-helium atmosphere. Since the scale height of the vapor atmosphere is smaller than that of a hydrogen-helium atmosphere with the same temperature, $R_{\text{XUV}} \simeq R_p$ is a good approximation also for the vapor atmosphere.

In this study, we assumed the host star to be a G-star. We adopt the empirical formula derived by Ribas et al. (2005) for F_{XUV} :

$$F_{\text{XUV}} = \begin{cases} 504 \left(\frac{a}{1\text{AU}}\right)^{-2} \text{ erg s}^{-1} \text{ cm}^{-2} & (t < 0.1\text{Gyr}) \\ 29.7 \left(\frac{t}{1\text{Gyr}}\right)^{-1.23} \left(\frac{a}{1\text{AU}}\right)^{-2} \text{ erg s}^{-1} \text{ cm}^{-2} & (t \geq 0.1\text{Gyr}). \end{cases} \quad (3.14)$$

We use the formula for K_{tide} derived by Erkaev et al. (2007)

$$K_{\text{tide}} = \frac{(\eta - 1)^2(2\eta + 1)}{2\eta^3}, \quad (3.15)$$

where η is the ratio of the Roche-lobe (or Hill) radius to the planetary radius, R_p .

Since minor gases such as CO_2 contribute to it via radiative cooling, the value of the heating efficiency is unknown. For photoevaporation of hot-Jupiters, ε is estimated to be of the order of 0.1 (Yelle et al. (2008) and reference therein). Thus, we adopt $\varepsilon = 0.1$ as a fiducial value, and investigate the sensitivity of our results to ε .

Adopting $\varepsilon = 0.1$ implies that the atmospheric escape occurs from a hydrogen-dominated photosphere. In this study, we assumed that oxygen atoms also escape from the atmosphere with hydrogen atoms. This is valid when oxygen is minor in the atmosphere, as we can estimate this based on the following equation of the crossover mass m_c ,

$$m_c = m_H + \frac{k_B T F_H}{n_H D_{H-O}} \quad (3.16)$$

where m_H is the mass of a hydrogen atom, F_H is the escape flux of hydrogen atoms, T is the temperature at the upper atmosphere, n_H is the number density of hydrogen, and D_{H-O} is the molecular diffusion coefficient, respectively. The relationship between the

escape flux F_H and the mass loss rate \dot{M} is

$$\dot{M} = 4\pi R_p^2 \frac{N_A}{m_H} F_H \quad (3.17)$$

where $N_A (= 6.02 \times 10^{23})$ is the Avogadro's number. With Eqs. (3.13), (3.16), and (3.17), we can obtain

$$m_c = m_H + 16.7 \frac{T}{n_H D_{H-O}} \left(\frac{a}{0.01 \text{ AU}} \right)^{-2} \left(\frac{\varepsilon}{0.1} \right) \left(\frac{R_p}{R_\oplus} \right) \left(\frac{M_p}{M_\oplus} \right)^{-1}. \quad (3.18)$$

If $\frac{T}{n_H D_{H-O}}$ is larger than unity, oxygen atoms can be escaped from the atmosphere. When we assume a typical Jovian middle atmosphere value, $\frac{T}{n_H D_{H-O}} \sim 10^{-17}$, oxygen atoms cannot be escaped from the atmosphere. However the planet we consider here is in much hotter circumstances than that of Jovian middle atmosphere. Moreover the exact values for T , n_H , and D_{H-O} at the upper atmosphere are unknown. In this study, we simply assume that $\frac{T}{n_H D_{H-O}}$ is large enough to satisfy $m_c > m_O$ where m_O is the mass of an oxygen atom.

We also estimate the escape parameter for a water-dominated atmosphere. We can find that

$$\lambda = \frac{GMm}{Rk_B T} \sim 68 \times \left(\frac{m}{m_{\text{H}_2\text{O}}} \right) \left(\frac{T}{2000 \text{ K}} \right)^{-1} \left(\frac{M}{M_\oplus} \right) \left(\frac{R}{R_\oplus} \right)^{-1}. \quad (3.19)$$

The escape parameter for a hydrogen atom for Earth is $\lambda \sim 25$. For a close-in planet we consider here, the upper atmosphere should be high temperature compared to that of Earth. In this study, we also simply assume that the upper atmosphere is high temperature environment enough to escape water molecules from the atmosphere.

Finally, we assume that the rocky core never evaporates. That is simply because we are interested in the stability of water envelopes in this study. Whether rocky cores evaporate or not is beyond the scope of this study.

3.2.6 Transit radius

The planetary radius measured by transit photometry is different from the photospheric radius defined in the preceding subsection. The former is the radius of the disk that blocks the stellar light ray that grazes the planetary atmosphere in the line of sight. This radius

is called the transit radius hereafter in this study. Below we derive the transit radius, basically following Guillot (2010). Note that Guillot (2010) assumed the plane-parallel atmosphere, while we consider spherically symmetric structure, because the atmospheric thickness is not negligibly small relative to the planetary radius in some cases in this study.

We introduce the chord optical depth, τ_{ch} (e.g. Guillot 2010), which is defined as

$$\tau_{\text{ch}}(r, \nu) = \int_{-\infty}^{+\infty} \rho \kappa_{\nu} ds, \quad (3.20)$$

where r is the planetocentric distance of the light of interest (see Fig.3.2), s is the distance along the line of sight measured from the point where the line is tangent to the sphere, and κ_{ν} is the monochromatic opacity at the frequency ν . Using τ_{ch} , we define the transit radius, R_{tr} , as

$$\tau_{\text{ch}}(R_{\text{tr}}) = \frac{2}{3}. \quad (3.21)$$

Let the altitude from the sphere of radius r be z_{tr} . Then $s^2 = (r + z_{\text{tr}})^2 - r^2$ (Fig.3.2). Eq.(3.20) is written as

$$\tau_{\text{ch}}(r, \nu) = 2 \int_0^{\infty} \rho \kappa_{\nu} \frac{z_{\text{tr}} + r}{\sqrt{z_{\text{tr}}^2 + 2rz_{\text{tr}}}} dz_{\text{tr}}. \quad (3.22)$$

Furthermore, we choose pressure P as the independent variable, instead of z_{tr} . Using the equation of hydrostatic equilibrium,

$$\frac{dP}{dz_{\text{tr}}} = -\frac{GM_p \rho}{(r + z_{\text{tr}})^2}, \quad (3.23)$$

one obtains

$$\tau_{\text{ch}}(\nu, r) = -\frac{2}{g_r} \int_{P_r}^0 \kappa_{\nu} \frac{(1 + z_{\text{tr}}/r)^2}{\sqrt{1 - (1 + z_{\text{tr}}/r)^{-2}}} dP, \quad (3.24)$$

where

$$g_r = \frac{GM}{r^2} \quad (3.25)$$

and P_r is the pressure at r . To integrate Eq.(3.24), we write z_{tr} as a function of P . To

do so, we integrate Eq.(3.23) and obtain

$$\int_0^{z_{\text{tr}}} \frac{dz'}{(r+z')^2} = - \int_{P_r}^{P_z} \frac{dP}{GM_p \rho}, \quad (3.26)$$

where P_z is the pressure at z_{tr} . Eq.(3.26) is integrated as

$$\begin{aligned} \frac{1}{r+z_{\text{tr}}} &= \frac{1}{r} - \frac{1}{r^2 g_r} \int_{P_z}^{P_r} \frac{dP}{\rho} \\ &= \frac{1}{r} - \frac{z_p(P_r, P_z)}{r^2}, \end{aligned} \quad (3.27)$$

where

$$z_p(P_r, P_z) \equiv \int_{P_z}^{P_r} \frac{P}{\rho g_r} d \ln P. \quad (3.28)$$

Thus, z is written as

$$z_{\text{tr}} = z_p \left(1 - \frac{z_p}{r}\right)^{-1}. \quad (3.29)$$

Note that z_p corresponds to the altitude in the case of a plane-parallel atmosphere, and $(1 - z_p/r)^{-1}$ is the correction for spherical symmetry.

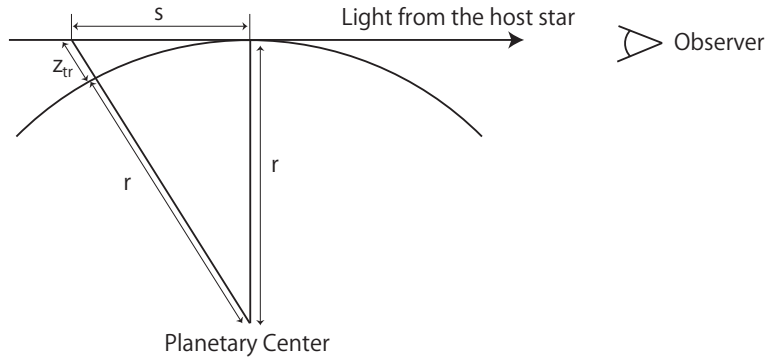


Figure 3.2: The figure of the chord optical depth.

3.2.7 Numerical procedure

To calculate the mass and radius evolution simultaneously, we integrate Eqs. (3.8) and (3.13) by the following procedure.

First we calculate two adiabatic interior models which are separated in time by the time interval Δt for the known $M_p(t)$ and an assumed $M_p(t + \Delta t)$. The two structures are

integrated for two different values of T_{int} . We integrate Eqs. (3.1)-(3.4) inward from the tropopause to the planetary center, using the fourth-order Runge-Kutta method. The inward integration is started with the outer boundary condition given by Eq. (3.6); P_{ad} and T_{ad} are calculated according to the atmospheric model described in § 3.2.4. We then look for the solution that fulfills the inner boundary condition (i.e., $r = 0$ at $M_r = 0$) in an iterative fashion. Note that determining P_{ad} and T_{ad} requires the gravity in the atmosphere (or R_{conv}), which is obtained after the interior structure is determined. Thus, we have to find the solution in which the interior and atmospheric structures are consistent with each other also in an iterative fashion.

Then we calculate Δt from the second-order difference equation for Eq. (3.8), which is written as

$$\Delta t = -\frac{[\bar{S}_e(t + \Delta t) - \bar{S}_e(t)][\Theta_e(t + \Delta t) + \Theta_e(t)] + [\bar{S}_c(t + \Delta t) - \bar{S}_c(t)][\Theta_c(t + \Delta t) + \Theta_c(t)]}{L_p(t + \Delta t) + L_p(t)}, \quad (3.30)$$

where

$$\Theta_e(t) \equiv \int_{M_c}^{M_p(t)} T(t) dM_r, \quad \Theta_c(t) \equiv \int_0^{M_c} T(t) dM_r. \quad (3.31)$$

Using this Δt , we integrate Eq. (3.13) to calculate $M_p(t + \Delta t)$ as

$$M_p(t + \Delta t) = M_p(t) + \dot{M} \Delta t. \quad (3.32)$$

The assumed value of $M_p(t + \Delta t)$ is not always equal to that obtained by Eq. (3.32). Therefore the entire procedure must be repeated until the $M_p(t + \Delta t)$ in Eq. (3.32) coincides with that assumed for calculating Eq. (3.30) with satisfactory accuracy, which is $\lesssim 0.1$ % in our calculations.

Once we obtain the interior and atmospheric structure, we calculate the transit radius by the procedure described in § 3.2.6. Finally we have confirmed that our numerical code reproduces well the mass and radius relationship for super-Earths presented by Valencia et al. (2010).

3.3 Mass evolution

In this section, we show our results of the mass evolution of a close-in ice giant. The evolution is controlled by the following five parameters: the initial total mass of the planet ($M_{p,0}$), the initial luminosity (L_0), the initial water mass fraction ($X_{\text{wt},0}$), the semi-major axis (a), and the heating efficiency (ε). Below we adopt $L_0 = 1 \times 10^{24}$ erg s $^{-1}$, $X_{\text{wt},0} = 75$ %, $a = 0.1$ AU, and $\varepsilon = 0.1$ as fiducial values unless otherwise noted. We also show how the five parameters affect the fate of a close-in water-rich planet.

3.3.1 Examples of mass evolution

Figure 3.3 shows examples of the mass evolution for water-rich planets with six different initial masses; $L_0 = 1 \times 10^{24}$ erg s $^{-1}$, $X_{\text{wt},0} = 50$ %, $a = 0.1$ AU, and $\varepsilon = 0.1$ in these simulations, as stated above. The smallest planet loses its water envelope completely in 1 Gyr (the dashed line), while more massive planets retain their water envelopes for 10 gigayears (solid lines). This means that a water-rich planet below a threshold mass ends up as a naked rocky planet.

The existence of the threshold mass is understood in the following way. Using Eq. (3.13), we define a characteristic timescale of the mass loss (τ_M) as

$$\tau_M = \left| \frac{X_{\text{wt}} M_p}{\dot{M}_p} \right| = \frac{4GK_{\text{tide}} X_{\text{wt}} M_p \rho_{\text{pl}}}{3\varepsilon F_{\text{XUV}}}, \quad (3.33)$$

where ρ_{pl} is the mean density of the planet. As the mass of the planet decreases, the timescale of mass loss becomes shorter. This trend is enhanced by the fact that the mean density decreases as M_p decreases, according to our numerical results.

In addition, the time-dependence of the stellar XUV flux (see Eq. [3.14]) is a crucial factor to cause a striking difference in behavior between the low-mass and high-mass planets. Using Eq. (3.14), we obtain the following relation for τ_M :

$$\tau_M \simeq \begin{cases} 3 \times 10^8 f \text{ yr}, & \text{for } t < 0.1 \text{ Gyr}, \\ 3 \times 10^8 \left(\frac{t}{0.1 \text{ Gyr}} \right)^{1.23} f \text{ yr}, & \text{for } t \geq 0.1 \text{ Gyr}, \end{cases} \quad (3.34)$$

where

$$f = 1 \left(\frac{a}{0.1\text{AU}} \right)^2 \left(\frac{X_{\text{wt}} M_p}{M_{\oplus}} \right) \left(\frac{\rho_{\text{pl}}}{0.1\text{g cm}^{-3}} \right) \left(\frac{K_{\text{tide}}}{0.9} \right) \left(\frac{\varepsilon}{0.1} \right)^{-1}. \quad (3.35)$$

Note that 0.1 g cm^{-3} is a typical value of ρ_{pl} in the case of sub-Earth-mass planets with age of 10^8 years, according to our calculations. As seen in Eq.(3.34), τ_M becomes longer rapidly with time. This implies that small planets that satisfy $\tau_M < 0.1$ gigayears experience a significant mass loss. In other words, massive planets that avoid significant mass loss in the early phase can retain their mass for 10 gigayears. Thus, there exists a threshold mass below which a planet never retains its water envelope for a long period. Our numerical calculations found that the threshold mass (hereafter M_{thrs}) is $0.16 M_{\oplus}$ for the fiducial parameter set, which is in good agreement with $M_p < 0.2 M_{\oplus}$ derived from Eq.(3.34).

A similar idea of threshold mass was proposed by Lopez and Fortney (2013) for the planet with the hydrogen-helium atmosphere. Hydrogen-rich planets are more vulnerable to the photoevaporative mass loss than water-rich planets. According to their study, the threshold mass of the hydrogen-rich planet at 0.1 AU is $\sim 5 M_{\oplus}$. That is, M_{thrs} for water-rich planets is smaller by a factor of ~ 10 than that of hydrogen-rich planets.

The ice giants for Neptune-mass should retain their water during their ages. Thus the ice giants for Neptune-mass planet can ignore the mass loss due to the photo-evaporation.

3.3.2 Dependence on the initial planet's luminosity

The evolution during the first 0.1 gigayears determines the fate of the ice giant, as shown above. Such a trend is also shown by Lopez and Fortney (2013) for H+He atmospheres of rocky planets. This suggests that the sensitivity of the planet's fate to the initial conditions must be checked. In particular, the initial intrinsic luminosity may affect the early evolution of the planet significantly, because the planetary radius, which has a great impact on the mass loss rate, is sensitive to the intrinsic luminosity; qualitatively a large L_0 enhances mass loss because of a large planetary radius. On the other hand, L_0 is rather uncertain, because it depends on how the planet forms (e.g. accretion processes of planetesimals, migration processes and giant impacts). However, as shown below, the fate of the planet is insensitive to choice of L_0

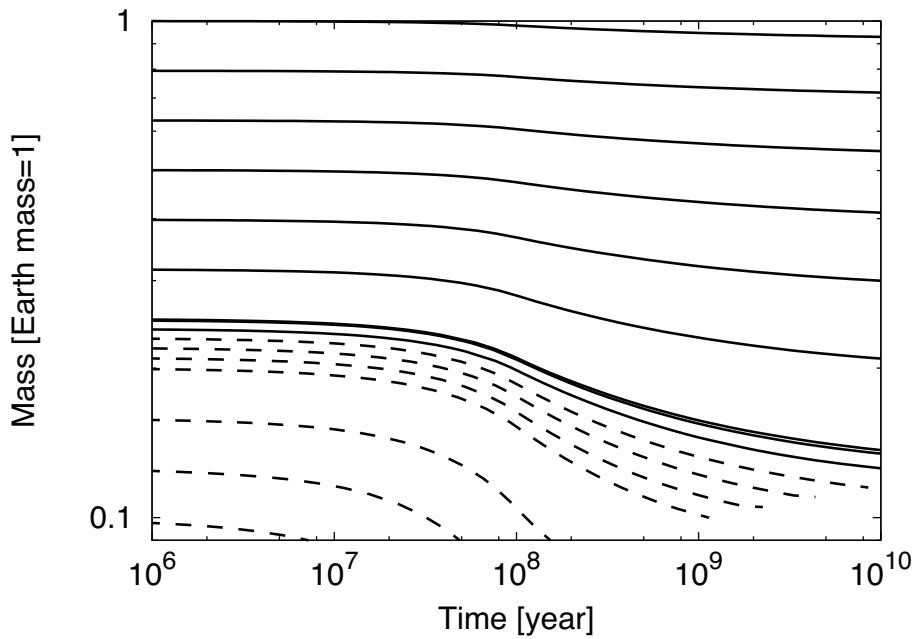


Figure 3.3: Mass evolution of close-in water-rich planets. The blue solid lines represent planets that retain their water envelopes for 10 gigayears. In contrast, the planet shown by the red dashed line loses its water envelope completely in 10 gigayears. We set $L_{p,0} = 1 \times 10^{24} \text{ erg s}^{-1}$, $X_{\text{wt},0} = 50\%$, $a = 0.1\text{AU}$, and $\varepsilon = 0.1$ for all the planets. In this model, we assume that the rocky core never evaporates.

Fig. 3.4 shows M_{thrs} as a function of L_0 for $a = 0.02, 0.03, 0.05$ and 0.1 AU. We have found that M_{thrs} is almost independent of L_0 . This is because an initially-luminous planet cools down rapidly, so that the integrated amount of water loss during the high-luminosity phase is negligible. This is confirmed by the following argument. The mass loss, ΔM , at the early stage can be estimated by

$$\Delta M \sim \dot{M} \tau_{\text{KH}}, \quad (3.36)$$

where τ_{KH} is the typical timescale of Kelvin-Helmholtz contraction,

$$\tau_{\text{KH}} \simeq \frac{GM_p^2}{2R_p L_p}. \quad (3.37)$$

With Eqs. (3.33) and (3.37) given, Eq.(3.36) can be written as

$$\Delta M \sim M_p \frac{\tau_{\text{KH}}}{\tau_M} = M_p \frac{\varepsilon}{2K_{\text{tide}}} \cdot \frac{\pi R_p^2 F_{\text{XUV}}}{L_p} \quad (3.38)$$

$$\begin{aligned} &\sim 3 \times 10^{-2} \left(\frac{F_{\text{XUV}}}{504 \text{ erg cm}^{-2} \text{ s}^{-1}} \right) \left(\frac{\varepsilon}{0.1} \right) \left(\frac{K_{\text{tide}}}{0.9} \right)^{-1} \\ &\quad \times \left(\frac{a}{0.1 \text{ AU}} \right)^{-2} \left(\frac{R_p}{3 R_{\oplus}} \right)^2 \left(\frac{L_p}{10^{24} \text{ erg s}^{-1}} \right)^{-1} M_p. \end{aligned} \quad (3.39)$$

Because F_{XUV} is constant in the early phase, ΔM decreases as L_p increases, i.e., the Kelvin-Helmholtz contraction proceeds more rapidly. Therefore, the choice of the value of L_0 has little effect on the total amount of water loss, as far as L_0 is larger than $10^{24} \text{ erg s}^{-1}$. For smaller L_0 , R_p is insensitive to L_0 . Thus, M_{thrs} is insensitive to L_0 .

3.3.3 Dependence on the initial water mass fraction

The fate of a water-rich planet also depends on the initial water mass fraction, $X_{\text{wt},0}$. Figure 3.5 shows $X_{\text{wt}}(t)$ at $t = 10$ gigayears as a function of the initial planet's mass, $M_{p,0}$, for four different values of $X_{\text{wt},0}$ (= 25 %, 50 %, 75 %, and 100 %). As $M_{p,0}$ decreases, $X_{\text{wt}}(10 \text{ gigayears})$ decreases. The pure water planet (solid line) with $M_{p,0} < 0.82 M_{\oplus}$ is completely evaporated in 10 Gyr, namely $X_{\text{wt}}(10 \text{ Gyr}) = 0$ %; otherwise $X_{\text{wt}}(10 \text{ Gyr}) = 100$ %. In other cases, we find that the threshold mass, M_{thrs} , below

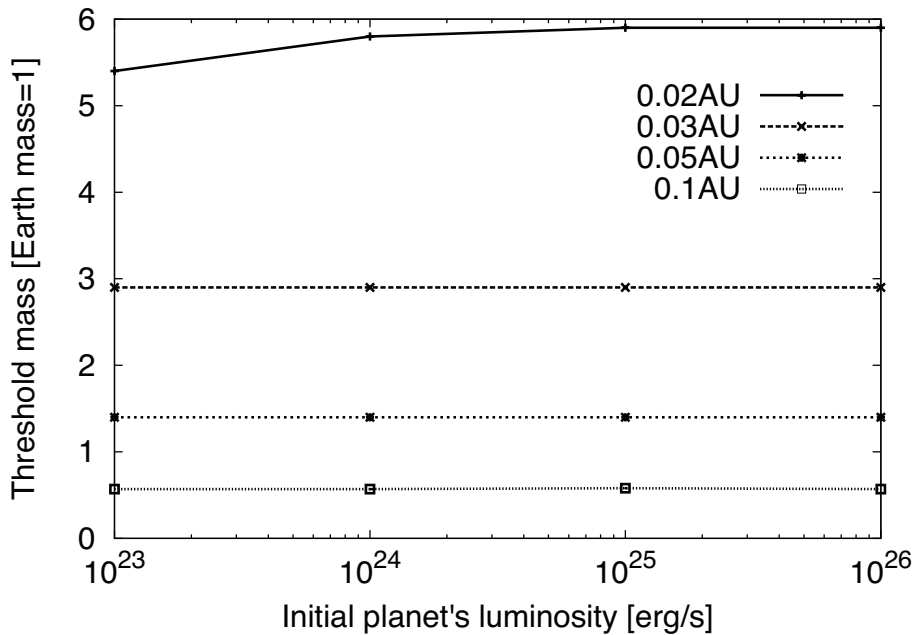


Figure 3.4: The threshold mass in M_{\oplus} as a function of the initial planet’s luminosity in erg s^{-1} for four choices of semimajor axes. The solid, dashed, dotted and dot-dashed represent $a = 0.02, 0.03, 0.05$ and 0.1 AU, respectively. We have assumed $X_{\text{wt}} = 75\%$ and $\varepsilon = 0.1$.

which $X_{\text{wt}}(10 \text{ Gyr}) = 0\%$, is $0.56 M_{\oplus}$ for $X_{\text{wt},0} = 75\%$, $0.44 M_{\oplus}$ for $X_{\text{wt},0} = 50\%$ and $0.44 M_{\oplus}$ for $X_{\text{wt},0} = 25\%$.

Figure 3.7 shows the relationship between $X_{\text{wt},0}$ and M_{thrs} for four different semi-major axes. M_{thrs} is found not to be a monotonous function of $X_{\text{wt},0}$. For $X_{\text{wt},0} < 25\%$, M_{thrs} decreases, as $X_{\text{wt},0}$ increases. This is explained as follows. According to Eq. (3.33), the mass loss timescale, τ_M , depends on the absolute amount of water, $X_{\text{wt}}M_p$, and the planetary bulk density, ρ_{pl} . When X_{wt} is sufficiently small, ρ_{pl} is equal to the rocky density and is therefore constant. Thus, τ_M is determined only by the absolute amount of water (i.e., $X_{\text{wt}}M_p$). This means that if $X_{\text{wt},0}$ is small, M_p must be larger for τ_M to be the same. As a consequence, M_{thrs} decreases with increasing $X_{\text{wt},0}$. More exactly, M_{thrs} changes with $X_{\text{wt},0}$ in such a way that $X_{\text{wt},0}M_{\text{thrs}}$ is constant. In contrast, when $X_{\text{wt},0}$ is large, not only X_{wt} and M_p , but also ρ_{pl} affect the mass loss timescale. For a given M_p , an increase in $X_{\text{wt},0}$ leads to a decrease in ρ_{pl} (or, an increase in radius), which enhances mass loss. As a result, M_{thrs} increases with $X_{\text{wt},0}$ for $X_{\text{wt},0} > 25\%$. Therefore, there is a minimum value of M_{thrs} , which is hereafter described by M_{thrs}^* .

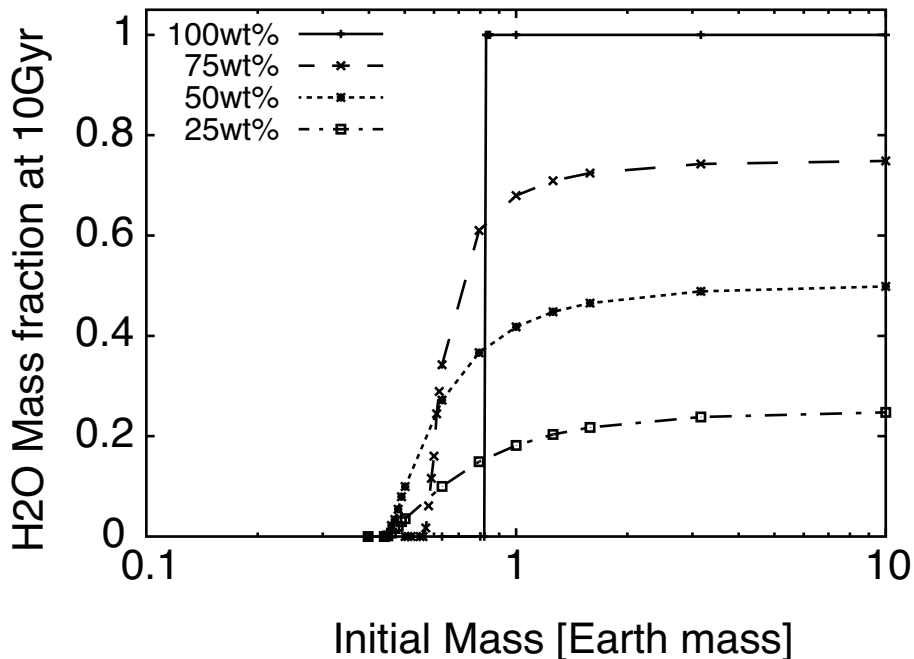


Figure 3.5: Relationship between the initial planetary mass and the fraction of the water envelope at 10 gigayears for four initial water mass fractions of $X_{\text{wt},0} = 100\%$ (solid), 75% (dashed), 50% (dotted), and 25% (dot-dashed). We have assumed $L_0 = 1 \times 10^{24} \text{ erg s}^{-1}$, $a = 0.1 \text{ AU}$ and $\varepsilon = 0.1$.

Similar trends can be seen in Figs. 3 and 4 of Lopez and Fortney (2013).

To compare our results for water-rich planets with those for hydrogen-rich rocky planets from Lopez and Fortney (2013) in a more straightforward way, we show the relationship between the initial total mass and the fraction of the initial water envelope that is lost via subsequent photo-evaporation in 5 gigayears in Fig. 3.6 (see Fig. 3c of Lopez and Fortney 2013). We set $L_0 = 1 \times 10^{24} \text{ erg s}^{-1}$, $a = 0.1 \text{ AU}$, $\varepsilon = 0.1$, and six initial water mass fractions of $X_{\text{wt},0} = 1\%$ (solid), 3% (long-dashed), 10% (dotted), 30% (dash-dotted), 50% (dot-dashed), and 60% (dashed), which are similar to those adopted by Lopez and Fortney (2013). As mentioned above, for the same fraction of the initial envelope to survive photo-evaporation, the initial total mass larger by a factor of ~ 10 is needed in the H+He case than in the water case. In addition, in the water case, the required initial total mass for $X_{\text{wt},0} < 10\%$ becomes significantly large. This behavior is also found in the case of the hydrogen-rich planets for $X_{\text{wt},0} = 1 - 3\%$. However, the trend is less noticeable in the H+He case. This is because the density effect described above is effective even for small H+He fractions.

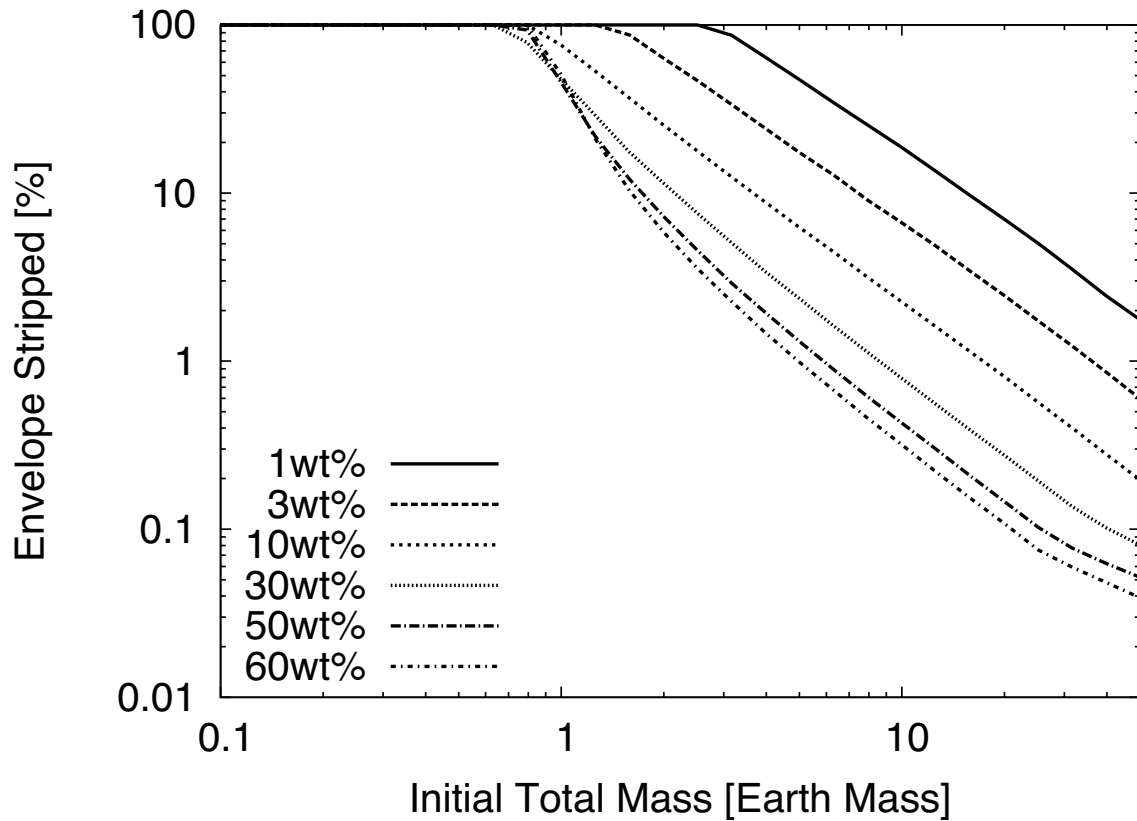


Figure 3.6: Relationship between the initial planetary mass and the fraction of the initial water envelope that is lost via photo-evaporation in 5 gigayears for six initial water mass fractions of $X_{\text{wt},0} = 1\%$ (solid), 3% (long-dashed), 10% (dotted), 30% (dash-dotted), 50% (dot-dashed) and 60% (dashed). We have assumed $L_0 = 1 \times 10^{24} \text{ erg s}^{-1}$, $a = 0.1 \text{ AU}$ and $\varepsilon = 0.1$.

3.3.4 Dependence on the semi-major axis

At small a , the incident stellar XUV flux becomes large. Thus, M_{thrs} increases, as a decreases. Certainly, the distance to the host star affects the equilibrium temperature T_{eq} which has an influence on ρ_{pl} : The higher T_{eq} is, the smaller ρ_{pl} is. However, its impact on M_{thrs} is small, relative to that of F_{XUV} . According to the planet's mass and mean density relationship, ρ_{pl} differs only by a factor of $\lesssim 1.5$ between 880 K and 2000 K. Therefore, increasing F_{XUV} has a much greater impact on the mass loss than decreasing ρ_{pl} . In Fig. 3.7, we find $M_{\text{thrs}}^* = 5.2 M_{\oplus}$ for $a = 0.02$ AU, $M_{\text{thrs}}^* = 2.5 M_{\oplus}$ for $a = 0.03$ AU, $M_{\text{thrs}}^* = 1.2 M_{\oplus}$ for $a = 0.05$ AU, and $M_{\text{thrs}}^* = 0.44 M_{\oplus}$ for $a = 0.1$ AU.

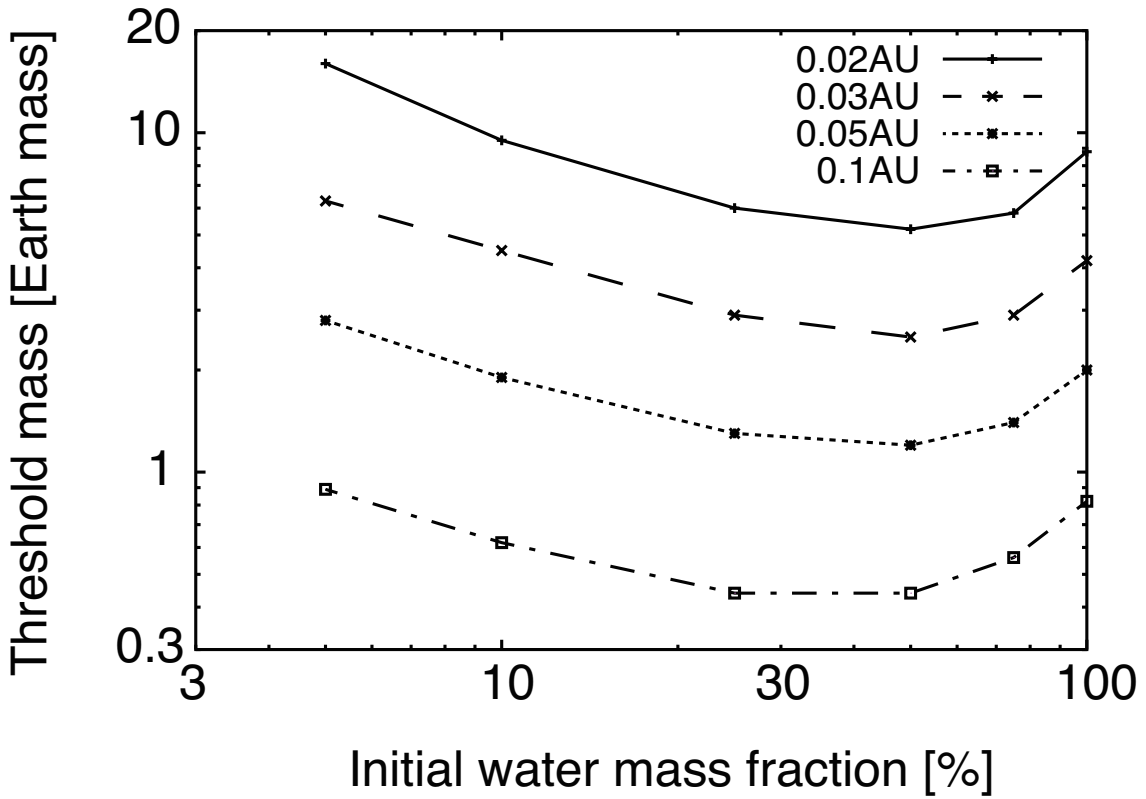


Figure 3.7: Relationship between the initial water mass fraction $X_{\text{wt},0}$ in % and the threshold mass M_{thrs} in M_{\oplus} for four choices of semi-major axes of 0.02 AU (solid), 0.03 AU (dashed), 0.05 AU (dotted) and 0.1 AU (dot-dashed). We have assumed $L_0 = 1 \times 10^{24}$ erg s^{-1} and $\varepsilon = 0.1$.

3.3.5 Expected Populations

Figure 3.8 shows the relationship between M_{thrs} (not M_{thrs}^*) and the radius that the planet with M_{thrs} would have at 10 Gyr without mass loss (solid line). We call this radius the threshold radius, R_{thrs} . We have calculated R_{thrs} for $X_{\text{wt},0} = 100\%$, 75% , 50% , 25% , 10% , 5% and 1% . In addition, the mass-radius relationships for rocky planets (dashed line) and pure-water planets (dotted line) at 0.1 AU are also drawn in Fig. 3.8. There are four characteristic regions in Fig. 3.8:

- I Planets must contain components less dense than water such as hydrogen/helium.
- II Planets with water envelopes and without hydrogen-helium can exist. The water envelopes survive photo-evaporative mass loss.
- III Primordial water envelopes experience significant photo-evaporative mass loss in 10 gigayears.
- IV Planets retain no water envelopes and are composed of rock and iron.

Only in the region II, the planet retains its primordial water envelope for 10 gigayears without significant loss. There are minimum values not only of M_{thrs} but also of R_{thrs} ; the latter is denoted by R_{thrs}^* hereafter. Note that R_{thrs}^* is not an initial radius. Those minimum values are helpful to discuss whether planets can possess water components or not, because the uncertainty in water mass fractions can be removed. Since M_{thrs} and R_{thrs} depend on semi-major axis, we also compare those threshold values with observed $M - a$ and $R - a$ relationships in the next section.

3.4 Implications for distributions of observed exoplanets

Figure 3.9 compares the relationship between the threshold mass, M_{thrs} , and threshold radius, R_{thrs} with measured masses and radii of super-Earths around G-type stars identified so far. Here we show three theoretical relationships for $a = 0.02$, 0.05 , and 0.1 AU. As discussed above, for a given a , only planets on the right side of the theoretical line

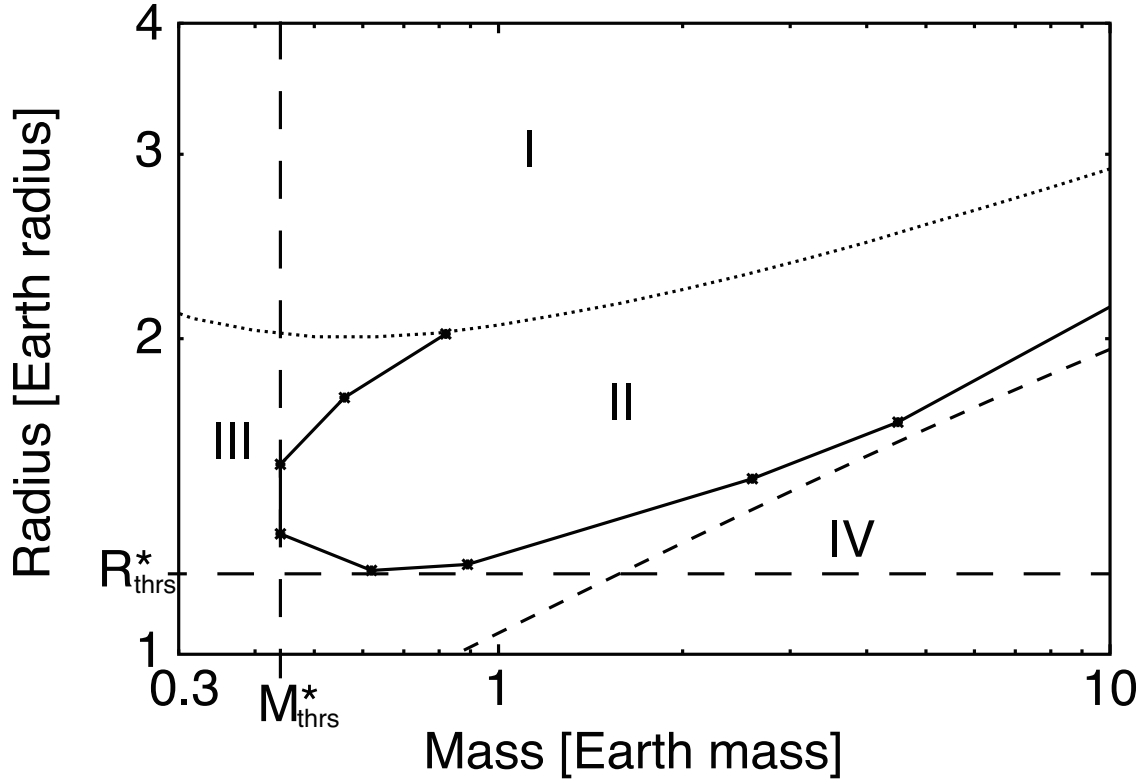


Figure 3.8: Relationship between the threshold mass and the threshold radius. The latter is defined by the radius that the planet with M_{thr} would have at 10 giga years without ever experiencing mass loss (denoted by R_{thr}). The squares, which are connected with a solid line, are M_{thr} and R_{thr} for 0.1 AU and seven different initial water mass fractions $X_{\text{wt},0} = 100\%$, 75% , 50% , 25% , 10% , 5% , 1% and 0.5% . The dashed and dotted lines represent mass-radius relationships, respectively, for rocky planets and pure-water planets at 0.1 AU. M_{thr}^* and R_{thr}^* represent the minimum values of M_{thr} and R_{thr} , respectively.

(i.e., in region II) are able to retain their water envelopes without significant loss for 10 gigayears.

For future characterizations, planets in region III would be of special interest, because our results suggest that planets should be rare in region III. Three out of the 14 planets, 55 Cnc e, Kepler-20 b, and CoRoT-7 b might be in region III, although errors and the uncertainty in ε (see also the lower panel of Figure 3.10 and 3.11 for the sensitivity of M_{thrs}^* to ε) are too large to conclude so. There are at least three possible scenarios for the origin of planets in region III. One is that those planets are halfway to complete evaporation of their water envelopes. Namely, some initial conditions happen to make planets in region III, although such conditions are rare. The second possible scenario is that those planets had formed far from and migrated toward their host stars recently. The third is that those planets are in balance between degassing from the rocky core and the atmospheric escape. Thus, deeper understanding of the properties of those super-Earths via future characterization will provide important constraints on their origins.

In this study, low-mass exoplanets whose masses are $\leq 20 M_{\oplus}$ and radii $\leq 4 R_{\oplus}$ are of special interest. (We call them super-Earths below.) While there are only 14 super-Earths whose masses and radii were both measured (see Fig. 3.9), the minimum masses ($M_p \sin i$), in addition to orbital periods, were measured for about 22 super-Earths around G-type stars (see Fig. 3.10 and 3.11). Also, over 1,000 sub/super-Earth-sized planet candidates have been identified by the Kepler space telescope (Batalha et al. 2013). The size and semi-major axis distribution of those objects is known. It is, thus, interesting to compare our theoretical prediction with the observed M_p - a and R_p - a distributions.

Before doing so, we demonstrate that M_{thrs}^* and R_{thrs}^* are good indicators for constraining the limits below which evolved planets cannot retain water envelopes. Figure 3.10 and 3.12 show the theoretical distributions of masses and radii of planets that evolved for 10 gigayears, starting with various initial water mass fractions and planetary masses (i.e., $X_{\text{wt},0} = 25, 50, 75$ and 100 % and $\log(M_{p,0}/M_{\oplus}) = -1 + 0.1j$ with $j = 0, 1, \dots, 21$). The crosses (red) and open squares (blue) represent the planets that lost their water envelopes completely (i.e., rocky planets) and those which survive significant loss of their water envelopes, respectively. As seen in these figures, two populations of rocky planets and water-rich planets are clearly separated by the M_{thrs}^* and R_{thrs}^* lines. Note that there

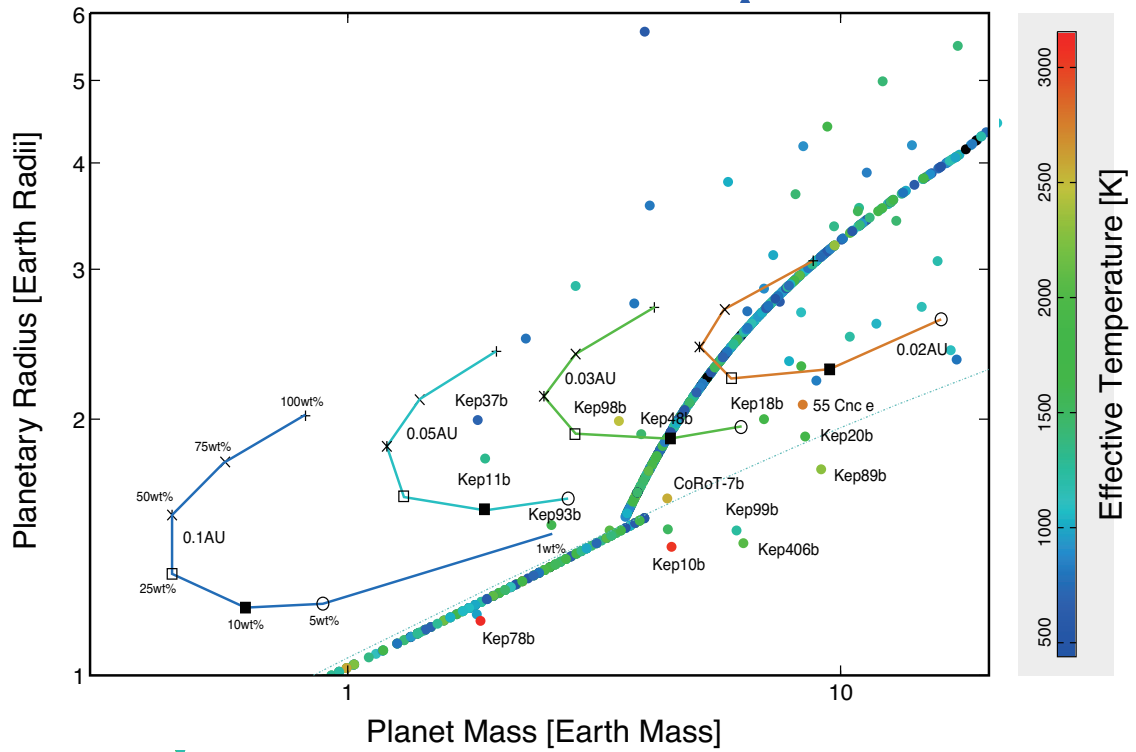


Figure 3.9: Relationship between the threshold mass M_{thrs} and radius R_{thrs} (lines; see text for definitions), compared with masses and radii of observed transiting super-Earths around G-type stars (points with error bars; exoplanets.org (Wright et al. 2011), as of June 29, 2013,). The solid, dashed and dotted represent the M_{thrs} and R_{thrs} relationships for orbital periods of 11 days (= 0.1 AU), 4 days (= 0.05 AU) and 1 day (= 0.02 AU), respectively. The dash-dotted line represents the planet composed of rocks. Note that black points represent planets whose orbital periods are longer than 11days. In those calculations, we have assumed the heating efficiency $\varepsilon = 0.1$ and the initial luminosity $L_0 = 1 \times 10^{24} \text{ erg s}^{-1}$. "CoR" are short for CoRoT and "Kep" are short for Kepler. Note that there are two lines. Planets on those lines are detected by only transit method. Planetary masses are estimated by the empirical formula derived by Weiss et al. (2013).

are some planets that retain water envelope below the threshold line. These planets just retain $\lesssim 1\%$ water mass fraction at 10 gigayears. However, such planets are found to be obviously rare.

In Fig. 3.11, we show the distribution of $M_p \sin i$ and a of low-mass exoplanets detected around G-type and K-type stars so far, compared with M_{thrs}^* for three choices of ε . Among them, Kepler-10 b and CoRoT-7 b are well below the M_{thrs}^* line for $\varepsilon = 0.1$. Thus, the two planets are likely to be rocky, provided $\varepsilon = 0.1$. However, the uncertainty in ε (and F_{XUV}) prevents us from deriving a robust conclusion. An order-of-magnitude difference in ε is found to change M_{thrs}^* by a factor of three. The aforementioned three planets are between the two M_{thrs}^* lines for $\varepsilon = 0.01$ and 0.1 . This demonstrates quantitatively how important determining ε and F_{XUV} more accurately is for understanding the composition of super-Earths only with measured masses. It would be worth mentioning that few planets are found between the lines for $\varepsilon = 0.1$ and $\varepsilon = 1$. Since all the planets in Fig. 3.11 were found by the radial-velocity method, the apparent gap would be unlikely to be due to observational bias. Thus, the gap might suggest that the actual M_{thrs}^* line lies between those two ones.

In Fig. 3.13, we show the distribution of R_p and a of KOIs, which is compared with R_{thrs}^* for three choices of ε . Many planets are found to be below the R_{thrs}^* lines. We are unable to constrain the fraction of rocky planets quantitatively, because of the uncertainty in ε . However, since there are many points below the R_{thrs}^* line for ε of as small as 0.01, it seems to be a rather robust conclusion that KOIs contain a significant number of rocky planets. Note that the distribution must include rocky planets that formed rocky without ever experiencing mass loss. This means there are more rocky planets in reality than we have predicted in this study.

As mentioned in Introduction, Lopez and Fortney (2013) performed a similar investigation of threshold mass and radius concerning H+He atmospheres on rocky super-Earths (see Figs. 8 and 9 of Lopez and Fortney (2013)). As the horizontal axis, they adopted the incident stellar flux, instead of semi-major axis. In Figs. 3.10 and 3.12, we have also indicated another scale of the incident flux calculated from the relationship between the

semi-major axis a and the incident flux F ,

$$F = \frac{L_{\text{star}}}{4\pi a^2} = F_{\text{Earth}} \left(\frac{L_{\text{star}}}{L_{\odot}} \right) \left(\frac{a}{1\text{AU}} \right)^{-2}, \quad (3.40)$$

where L_{star} is the luminosity of the host star and F_{Earth} is the current bolometric flux that the Earth receives from the Sun. Comparing with their results for the H+He envelope, we find that while a similar linear dependence is found, the threshold value of the initial mass (or incident flux) for H₂O is smaller by a factor of about 10 than that for H+He. For example, in the case of $F = 10^3 F_{\oplus}$, the threshold mass for H+He is $\sim 30M_{\oplus}$ (derived by Eq. (6) of Lopez and Fortney 2013), while that for H₂O is $\sim 2M_{\oplus}$.

Figure. 9 of Lopez and Fortney (2013) suggested that the frequency of planets with radii of $1.8 - 4.0 R_{\oplus}$ for $F_p \geq 100 F_{\oplus}$ (corresponding to $a \leq 0.1$ AU) should be low as a consequence of photo-evaporative mass loss. In contrast, our results suggest that water-rich planets with radii of $1.5 - 3.0 R_{\oplus}$ are relatively common, because they are able to sustain their water envelopes against photo-evaporation. Indeed, there are many KOIs found in such a domain in the R_p - a diagram shown in Fig. 3.12. Thus, those KOIs may be water-rich planets, although it is also possible that they are rocky planets without ever experiencing mass loss.

Finally, in this study, we deal with the thermal escape of the upper atmosphere due to stellar XUV irradiation. In addition, ion pick-up induced by stellar winds and coronal mass ejections may be effective in stripping off atmospheres of close-in planets, as discussed for close-in planets with hydrogen-rich atmospheres (e.g. Lammer et al. 2013). Such non-thermal effects lead to increase in M_{thrs}^* . This implies that the M_{thrs}^* obtained in this study is a lower limit on survival of water-rich planets.

3.5 Summary

In this study, we have investigated the impact of photo-evaporative mass loss on masses and radii of water-rich sub/super-Earths with short orbital periods around G-type stars. We simulated the interior structure and evolution of highly-irradiated sub/super-Earths that consist of a rocky core surrounded by a water envelope, including the effect of mass

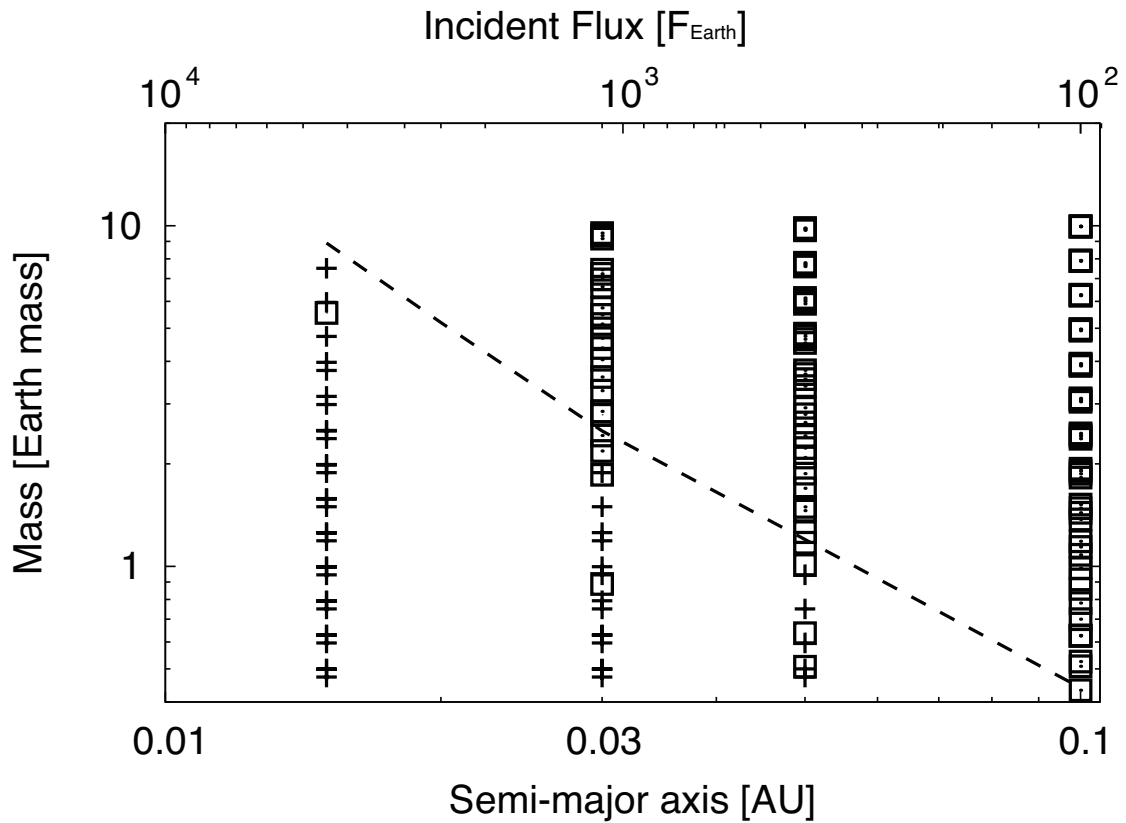


Figure 3.10: Theoretical distribution of masses and semi-major axes (or incident fluxes) of planets at 10 Gyr with various initial masses and water mass fractions. Cross points represent planets that lost their water envelopes completely in 10 giga years, while open squares represent planets that survive significant loss of the water envelopes via photo-evaporation. The green line is the minimum threshold masses, M_{thrs}^* . Here we have adopted $\varepsilon = 0.1$.

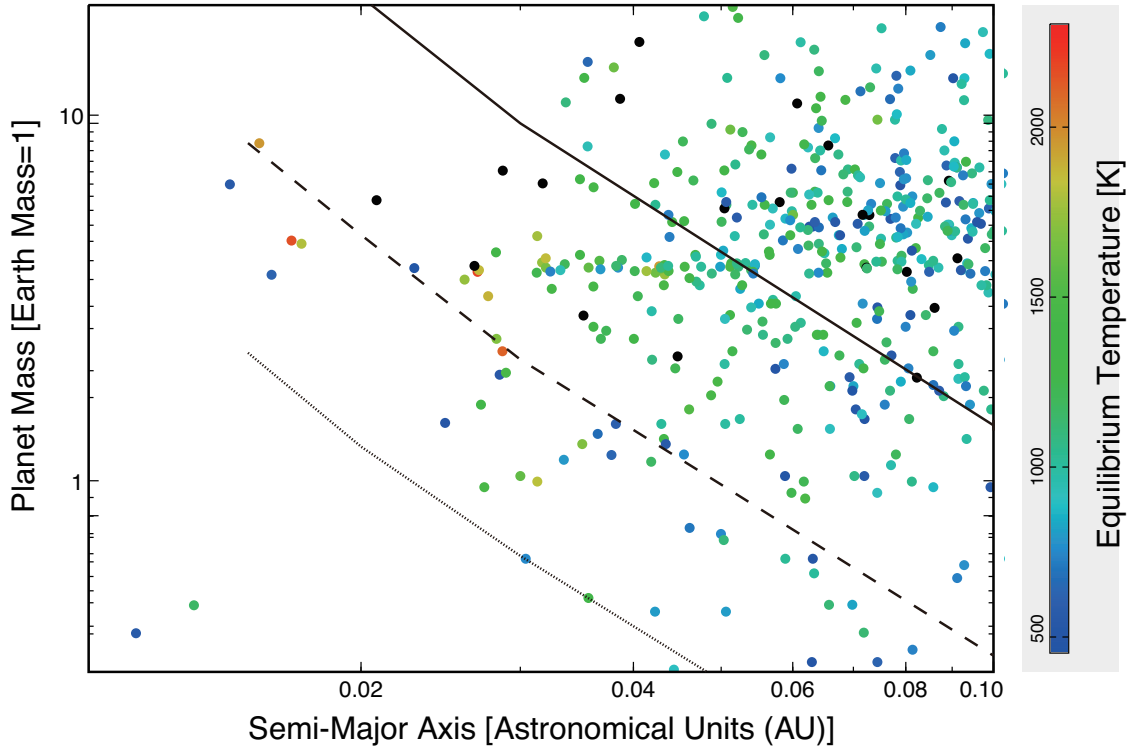


Figure 3.11: Distribution of masses and semimajor axes (or incident fluxes) of detected exoplanets compared with the minimum threshold mass, M_{thrs}^* , derived in this study (see § 3.3 for definition). We have shown three $M_{\text{thrs}}^* - a$ relationships for different heating efficiencies: $\varepsilon = 1$ (solid line), $\varepsilon = 0.1$ (dashed line) and $\varepsilon = 0.01$ (dotted line). Filled circles with error bars represent observational data (from <http://exoplanet.org> (Wright et al. 2011), as of February 12, 2016) for planets orbiting host stars with effective temperature of 5000-6000 K (relatively early K-type stars and G-type stars). Planets are colored according to their zero-albedo equilibrium temperatures in K. In the planet names, "CoR" and "Kep" stand for CoRoT and Kepler, respectively.

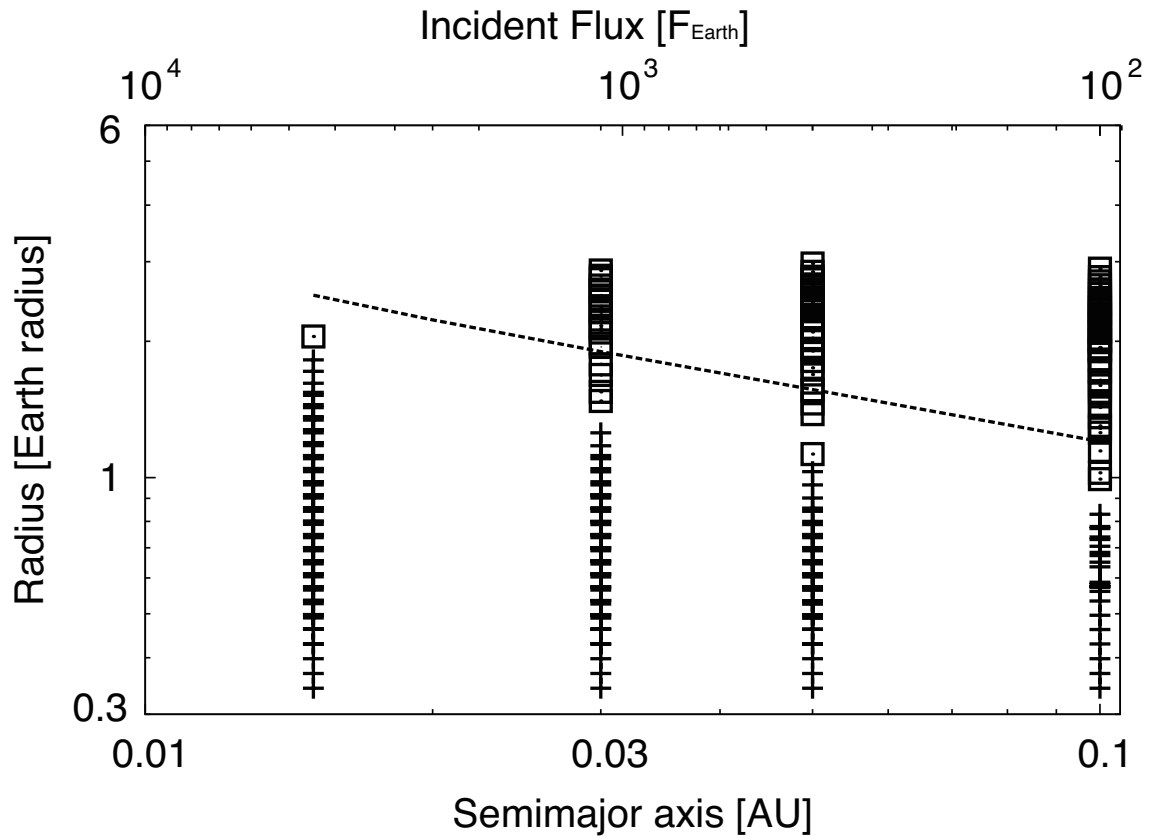


Figure 3.12: Theoretical distribution of radii and semi-major axes or incident fluxes of planets at 10 giga years with various initial masses and water mass fractions. Cross points represent planets that lost their water envelopes completely due to the photo-evaporation in 10 giga years, while open squares represent planets that survive significant loss of the water envelopes. The green line is the minimum threshold radii, R_{thrs}^* . Here we have adopted $\varepsilon = 0.1$.

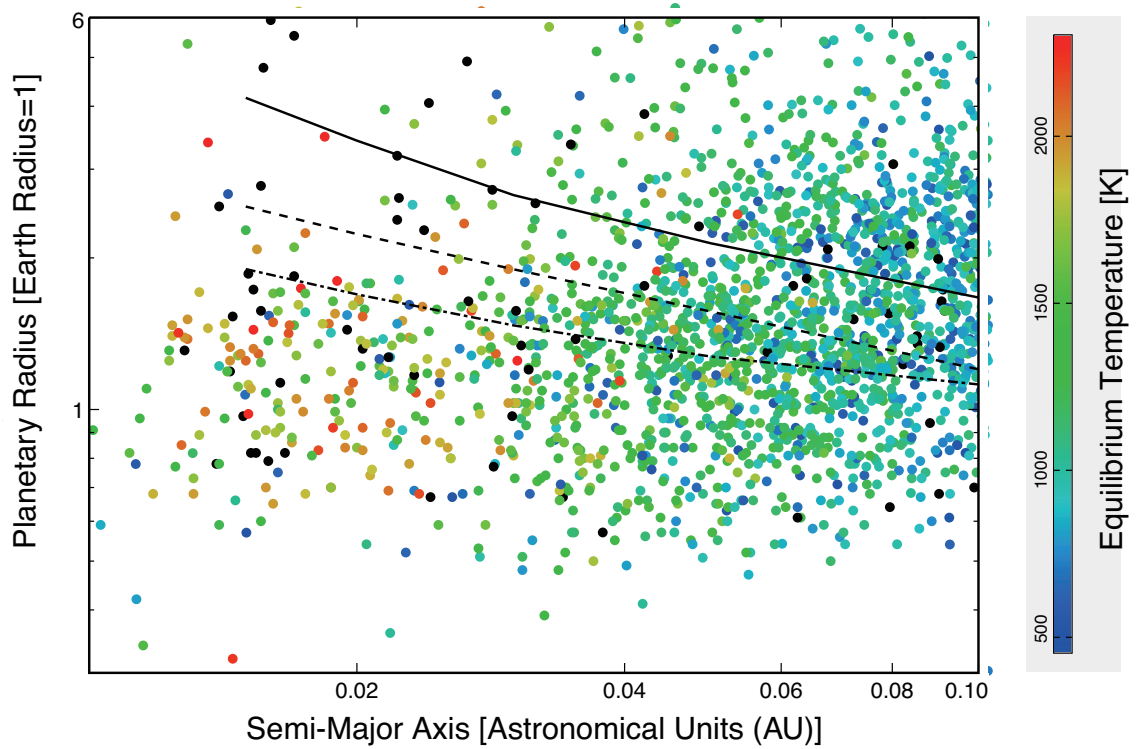


Figure 3.13: Distribution of radii and semi-major axes (or incident fluxes) of Kepler planetary candidates, compared with the threshold radius, R_{thrs}^* (see § 3.3 for definition). We have shown three $R_{\text{thrs}}^* - a$ relationships for different heating efficiencies: $\epsilon = 1$ (solid line), $\epsilon = 0.1$ (dashed line) and $\epsilon = 0.01$ (dotted line). Filled squares represent observational data (from <http://exoplanet.org> (Wright et al. 2011), as of February 12, 2016) for planets orbiting host stars with effective temperature of 5300-6000 K (G-type stars).

loss due to the stellar XUV-driven energy-limited hydrodynamic escape (see § 3.2).

Here we summarize this study below. In § 3.3, we have investigated the mass evolution of water-rich sub/super-Earths, and then found a threshold planet mass M_{thrs} , below which the planet has its water envelope stripped off in 1-10 Gyr (§ 3.3.1). The initial planet's luminosity has little impact on M_{thrs} (§ 3.3.2). We have found that there is a minimum value, M_{thrs}^* , for given a and ϵ (§ 3.3.4). Water-rich planets with initial masses smaller than M_{thrs}^* lose their water envelopes completely in 10 gigayears, independently of initial water mass fraction. The threshold radius, R_{thrs} , is defined as the radius that the planet of mass M_{thrs} would have at 10 gigayears if it evolved without undergoing mass loss. We also found that there is a minimum value of the threshold radius, R_{thrs}^* (§ 3.3.5). Finally, in § 3.4, we discussed the composition of observed low-mass exoplanets, by comparing the threshold values with measured masses and radii of the exoplanets. Then, we have confirmed quantitatively that more accurate determination of planet masses and radii, ϵ and F_{XUV} is needed for deriving robust prediction for planetary composition. Nevertheless, the comparison between R_{thrs}^* and radii of KOIs in the $R_p - a$ plane suggests that KOIs contain a significant number of rocky planets.

In this study, we demonstrated that photo-evaporative mass loss has a significant impact on the evolution of water envelopes of sub/super-Earths, especially with short orbital periods, as well as that of H+He envelopes of super-Earths. Since water envelopes are more stable against photo-evaporation than H+He envelopes, the stability limit for water envelopes gives more robust constraints on the detectability of rocky planets. Thus, the M_{thrs} and R_{thrs} will provide valuable information for future search for rocky Earth-like exoplanets.

Chapter 4

Conclusions

This dissertation investigates the impacts of the internal compositional distribution on the thermal evolution and the bulk composition's evolution of ice giants. Long-period ice giants experienced the thermal evolution and the condensation of water, ammonia, and methane in the atmosphere simultaneously. We propose one hypothesis to explain the present luminosity of Uranus. Our results suggest that the difference of the present luminosities between Uranus and Neptune have been related to their rotation axis that is made by giant impact events. Short-period ice giants, water-rich sub/super-Earths, have experienced the thermal evolution and mass loss simultaneously. We indicate that the bulk composition of ice giants would be different depending on when they were formed. We also show that the effect of mass loss of the vapor atmosphere would be essential to understand the origin of planetary system, together with the comparisons with observations. Condensation and mass loss remove the water or other ice compositions from the atmosphere. In this dissertation, we revealed that even though the present planetary atmosphere would have contained a small amount of ice constituents, the planetary evolution is totally quite different whether the planet possessed a lot of ice compositions when it was formed. These results will give insights into connecting theory and observations of planetary atmosphere, which is essential to understand the origins of the solar system and beyond.

Acknowledgment

My thanks go first to Dr. M. Ikoma. His advice, encouragement, and wisdom have guided this study properly. Without his guidance, the successful completion of this thesis would not be possible. Moreover, without his encouragement, I would have decided to leave the University.

I would like to thank Professor H. Nagahara, Professor E. Tajika, Associate Professor Y. Abe, Associate Professor Y. Sekine, and Assistant Professor H. Kawahara for their constructive comments of this thesis. I would like to thank Dr. Y. Hori. He kindly give me suggestion, comment and the equation of states and opacities data tables. I would like to thank Dr. K. Hamano, T. Kodama, S. Kadoya, Y. Takao, and other members of L-seminar for their fruitful discussions. Without their studies, suggestion, and discussions, the concept of Chapter 2 would not be born. I would like to thank Dr. N. Narita, Dr. A. Fukui, and other member of transit observation group for their constructive comments and discussions. I would like to thank Y. Ito, Y. Kawashima, Y. Aoyama, Y. Shirai, N. Hasegawa, and S. Hirose for fruitful discussions. I would like to thank M. Enomoto and for her kindly consultant and mental support. I would like to thank T. Taki, Y. Tanaka, Y. Chang, and M. Harada for their suggestions. I would like to thank Y. Suto, K. Masuda, S. Kamiaka and other lunch seminar group members for fruitful suggestions. Lastly, I would like to thank my family during the past days.

This dissertation was is supported by a grant for the Global COE Program, "From the Earth to "Earths"", of MEXT, Japan from April 1, 2013 to March 31, 2014, and Japan Society for the Promotion of Science(JSPS) Grant Number 26-11515 from April 1, 2014 to March 31, 2016.

Appendix A

Theory: Basic physics of the planetary interior structure and the thermal evolution

A.1 Interior structure for the polytropic model

I summarize the interior structure for the polytropic model and derive the mass-radius relationship for the polytropic model planet.

If I assume the relation between the pressure and the density as

$$P \equiv K\rho^{1+1/n}, \quad (\text{A.1})$$

the planetary interior structure can be solved, because the hydrostatic equations is closed.

I assume the planet is in spherical symmetric hydrostatic equilibrium;

$$\frac{dP}{dr} = -\rho \frac{d\Phi}{dr} \quad (\text{A.2})$$

where Φ is the gravitational potential which requires Poisson's equation;

$$\frac{1}{r^2} \frac{d}{dr} \left(r^2 \frac{d\Phi}{dr} \right) = 4\pi G\rho. \quad (\text{A.3})$$

With polytropic relation, A.2 can be written

$$\frac{d\Phi}{dr} = - \left(1 + \frac{1}{n}\right) K \rho^{-1+1/n} \frac{d\rho}{dr} \quad (\text{A.4})$$

where K is assumed to be constant. If $n \neq 0$, (A.4) can be integrated by r from center ($r = 0$) to surface ($r = R$, which means $\Phi(R) = 0$ at the surface $\rho(R) = 0$);

$$\rho = \left(\frac{-\Phi}{(n+1)K} \right)^n. \quad (\text{A.5})$$

Note that the interior of the planet $\Phi < 0$ gives there $\rho > 0$.

Here I derive the Lane-Emden equation. With (A.2) and (A.4), I obtain an ordinary differential equation for ρ :

$$\frac{d^2 \rho^{1/n}}{dr^2} + \frac{2}{r} \frac{d\rho^{1/n}}{dr} = - \frac{4\pi G}{(n+1)K} (\rho^{1/n})^n \quad (\text{A.6})$$

I now define dimensionless variables z, w by

$$z = Ar \quad (\text{A.7})$$

$$w = \left(\frac{\rho}{\rho_c} \right)^{1/n} \quad (\text{A.8})$$

where A is constant;

$$A^2 = \frac{4\pi G}{(n+1)K} \rho_c^{1-1/n}, \quad (\text{A.9})$$

and subscript "c" refers to the center; $\rho_c = \rho(r = 0)$. At the center I have $z = 0$ and $\rho = \rho_c$ and therefore $w = 1$. Then (A.9) can be written

$$\frac{d^2 w}{dz^2} + \frac{2}{z} \frac{dw}{dz} + w^n = 0 \quad (\text{A.10})$$

or

$$\frac{1}{z^2} \frac{d}{dz} \left(z^2 \frac{dw}{dz} \right) + w^n = 0. \quad (\text{A.11})$$

(A.10) is called Lane-Emden equation. (A.10) has analytical solutions for $n = 0, 1$ and 5 ;

$$n = 0 : w(z) = 1 - \frac{1}{6}z^2, \quad (\text{A.12})$$

$$n = 1 : w(z) = \frac{\sin z}{z}, \quad (\text{A.13})$$

$$n = 5 : w(z) = \frac{1}{\sqrt{1 + z^2/3}}, \quad (\text{A.14})$$

if I set boundary condition $w(z = 0) = 1$ and $w'(z = 0) = 0$. Note that w represents not only ρ but also Φ . With (A.5), w and A can be written

$$w = \frac{\Phi}{\Phi_c} \quad (\text{A.15})$$

$$A^2 = \frac{4\pi G}{(n+1)^n K^n} (-\Phi_c)^{n-1} \quad (\text{A.16})$$

where Φ_c is

$$\Phi_c = -(n+1)K\rho_c^{1/n}. \quad (\text{A.17})$$

I derive the mass-radius relationship of the polytropic planet. With (A.5) and (A.7), ρ can be written

$$\rho = \rho_c w^n \quad ; \quad \rho_c = \left(\frac{-\Phi_c}{(n+1)K} \right)^n. \quad (\text{A.18})$$

Then I can write the planetary mass

$$M_r = \int_0^r 4\pi r^2 \rho dr = \frac{4\pi \rho_c}{A^3} \int_0^z w^n x^2 dz. \quad (\text{A.19})$$

With (A.19), (A.11) and $A = z/r$, M_r can be written

$$M_r = 4\pi \rho_c r^3 \left(-\frac{1}{z} \frac{dw}{dz} \right). \quad (\text{A.20})$$

For the special case of the surface, I have

$$M_p = 4\pi \rho_c R_p^3 \left(-\frac{1}{z} \frac{dw}{dz} \right)_{z=z_n}, \quad (\text{A.21})$$

where M_p is planetary mass, R_p is planetary radius and z_n is the value which satisfy $R_p = Az_n$ at the surface of the planet. According to (A.9), if the polytropic constant K is constant through the planetary interior, I can find

$$\frac{1}{A^2} = \left(\frac{r}{z}\right)^2 = \left(\frac{R_p}{z_n}\right)^2 = \frac{(n+1)K}{4\pi G} \rho_c^{(1-n)/n}. \quad (\text{A.22})$$

With (A.21) and (A.22), I can find the relation ($n \neq 1$)

$$M_p = CR^{(3-n)/(1-n)} \quad (\text{A.23})$$

where

$$C = 4\pi \left(\frac{4\pi G}{(n+1)Kz_n^2}\right)^{n/(1-n)} \cdot \left(-\frac{1}{z} \frac{dw}{dz}\right)_{z=z_n} \quad (\text{A.24})$$

If $n = 1$, I can derive $z_n = \pi$ by (A.13) for $w = 0$ which means outer boundary condition $\rho(R_p) = 0$. Then I can find the relation

$$R_p = \sqrt{\frac{\pi K}{2G}} \quad (\text{A.25})$$

which is independent of planetary mass. (A.25) relation appears in the case of gas giants such as hot-Jupiters.

A.2 The Virial theorem

I summarize the virial theorem for the hydrostatic equilibrium planet and derive how to shrink by cooling.

The virial theorem provides the general relation between the kinetic energy and the stable system bounded by potential energy. In astrophysics, this theorem describe the relation between the gravitational potential energy and the kinetic or thermal energy. To apply to the planetary interior structure, I use the hydrostatic equilibrium equation. I multiple $v = 4\pi r^3/3$ and integrate over dM_r in the interval $[0, M]$, that is from center to

surface. Then, I can describe the $\partial P/\partial M_r$ as

$$\int_0^M \frac{4}{3} \pi r^3 \frac{\partial P}{\partial M_r} dM_r = \left[\frac{4}{3} \pi r^3 P \right]_0^M - \int_0^M 4\pi r^2 \frac{\partial r}{\partial M_r} P dM_r \quad (\text{A.26})$$

$$= P_s V_p - \int_0^{R_p} 4\pi r^2 P dr, \quad (\text{A.27})$$

where P_s is the surface pressure of the planet, V_p is the bulk volume of the planet and R_p is the radius of the planet ($r(M_p) = R_p$). The inner boundary condition is $P(M_r = 0) = 0$. If I assume the outer boundary condition as $P(R_p) = 0$, the external force's work term $P_s V_p = 0$. In the right-hand side, the first term means the external force's work and the second term the internal force's work. The term $4\pi r^2 P dr$ can be rewrite to $(P/\rho)dM_r$ due to the mass conservation.

As a result, the hydrostatic equilibrium equation can be rewrite to

$$- \int_0^M \frac{P}{\rho} dM_r = - \frac{1}{3} \int_0^M \frac{GM_r}{r} dM_r \quad (\text{A.28})$$

I define the gravitational energy E_g by

$$E_g := - \int_0^M \frac{GM_r}{r} dM_r. \quad (\text{A.29})$$

I also define the total internal energy E_i by

$$E_i := \int_0^M u \cdot dM_r \quad (\text{A.30})$$

where u is the internal energy per unit mass. For a general equation of state, I define a quantity ζ by

$$\zeta u := 3 \frac{P}{\rho} \quad (\text{A.31})$$

Then, the virial theorem is

$$\int_0^M u \cdot dM_r + E_g = 0. \quad (\text{A.32})$$

If ζ is constant throughout the planet, I can derive

$$\zeta E_i + E_g = 0. \quad (\text{A.33})$$

I now define the total energy W ;

$$W = E_i + E_g \quad (\text{A.34})$$

where for a gravitationally bound system $W < 0$. If I combine the virial theorem result and $W < 0$, I can find the condition;

$$W = (1 - \zeta)E_i = \frac{\zeta - 1}{\zeta}E_g < 0. \quad (\text{A.35})$$

In the case of $\zeta = 1$ the total energy vanishes.

In order to understanding ζ , I derive the ζ value for ideal gas. For ideal gas,

$$\frac{P}{\rho} = \frac{R_g}{\mu}T = (c_P - c_v)T = (\gamma - 1)c_vT, \quad (\text{A.36})$$

where c_P, c_v are the specific heats per unit mass, γ is heat capacity ratio

$$\gamma := \frac{c_P}{c_v} \quad (\text{A.37})$$

in this subsection, R_g is universal gas constant ($R_g = k_B/m_u$, where k_B is Boltzmann constant and m_u is the atomic mass unit). I can write $u = c_vT$ which means the internal energy per unit mass of the ideal gas. Therefore, (A.31) is written

$$\zeta u = 3(\gamma - 1)u \implies \zeta = 3(\gamma - 1). \quad (\text{A.38})$$

The heat capacity ratio γ is related to the degree of freedom f of a molecule. According to the kinetic theory of gasses, a molecule's energy is distributed to $k_B T/2$ per one degree of freedom. then molecule's internal energy per unit mass u is written

$$u = \frac{k_B T}{2} \cdot f \cdot \frac{1}{\mu m_u} = \frac{f}{2} \cdot \frac{R_g}{\mu} T. \quad (\text{A.39})$$

Due to $\frac{R_g}{\mu} = (\gamma - 1)c_v$ for ideal gas, I can derive the relation

$$\gamma = 1 + \frac{2}{f}. \quad (\text{A.40})$$

Note that I assume vibration degrees of freedom is ignored. For a monatomic gas, degrees of freedom $f = 3$, for a linear molecules gas $f = 5$ and non-linear molecules gas $f = 6$. For a monatomic gas $\gamma = 5/3$ and I can find $\zeta = 2$. For a diatomic gas $\gamma = 7/5$ and I can find $\zeta = 6/5 = 1.2$. And for a non-linear molecule gas, such as H_2O , $\gamma = 4/3$ and I can find $\zeta = 1$.

As an example, I give a general expression for the gravitational energy E_g of polytropes. From the definition (A.29) of E_g , I find

$$E_g := - \int_0^{M_p} \frac{GM_r}{r} dM_r = -\frac{GM_p^2}{2R_p} - \frac{G}{2} \int_0^{R_p} \frac{M_r^2}{r^2} dr. \quad (\text{A.41})$$

To derive (A.41), I make use of partial integration and the fact that M_r/r vanishes at the center. On the other hand, the gravitational potential Φ satisfies

$$F_{\text{grav}} = -\frac{GM_r}{r^2} = -\frac{d\Phi}{dr} \quad (\text{A.42})$$

and therefore (A.41) can be written

$$\begin{aligned} E_g &= -\frac{GM_p^2}{2R_p} - \frac{1}{2} \int_0^{R_p} M_r \frac{GM_r}{r^2} dr \\ &= -\frac{GM_p^2}{2R_p} + \frac{1}{2} \int_0^{M_p} \Phi dM_r \end{aligned} \quad (\text{A.43})$$

where I have integrated the second term of the left hand side partially;

$$\begin{aligned} -\frac{1}{2} \int_0^{R_p} M_r \frac{d\Phi}{dr} dr &= -\frac{1}{2} \int_0^{M_p} M_r \frac{d\Phi}{dM_r} dM_r \\ &= -\frac{1}{2} [M_r \Phi]_0^{M_p} + \frac{1}{2} \int_0^{M_p} \Phi dM_r \\ &= \frac{1}{2} \int_0^{M_p} \Phi dM_r, \end{aligned} \quad (\text{A.44})$$

considering the inner boundary condition $r \rightarrow 0 \Rightarrow M_r \Phi \rightarrow 0$ and outer boundary condition $r \rightarrow R_p \Rightarrow M_r \Phi \rightarrow 0$. Since the outer boundary condition is defined by $\rho = 0$, I put $\Phi(r = R_p) = 0$ according to the relation (A.18). With (A.1) and (A.18), I can write

$$\Phi = -(n+1)K\rho^{1/n} = -(n+1)\frac{P}{\rho} \quad (\text{A.45})$$

and then (A.43) can be written

$$E_g = -\frac{GM_p^2}{2R_p} - \frac{n+1}{2} \int_0^{M_p} \frac{P}{\rho} dM_r. \quad (\text{A.46})$$

According to (A.28) and (A.29), (A.46) can be written

$$E_g = -\frac{GM_p^2}{2R_p} + \frac{n+1}{6} E_g, \quad (\text{A.47})$$

and therefore

$$E_g = -\frac{3}{5-n} \frac{GM_p^2}{R_p}. \quad (\text{A.48})$$

According to the virial theorem (A.33), I can derive the total internal energy

$$E_i = -\frac{1}{\zeta} E_g = \frac{3}{\zeta(5-n)} \frac{GM_p^2}{R_p} \quad (\text{A.49})$$

Therefore the total energy (A.34) becomes

$$W = E_i + E_g = -\frac{3}{5-n} \left(1 - \frac{1}{\zeta}\right) \frac{GM_p^2}{R_p}. \quad (\text{A.50})$$

(A.50) indicates that the total energy W for a polytrope of finite radius vanishes when $\zeta = 1$. And W for a polytrope of finite radius also vanishes when $n \geq 5$.

A.3 The impact of the initial luminosity on the analytical thermal evolution of the planet

In general, W , E_g and E_i are coupled. As the planet release its energy by radiation, the planet's total energy W must decrease. I set L the luminosity of the planet, i.e. the total energy loss per unit time by radiation. Then conservation of energy requires

$$\frac{dW}{dt} + L = 0 \quad (\text{A.51})$$

Then I can derive

$$L = (\zeta - 1) \frac{dE_i}{dt} = -\frac{\zeta - 1}{\zeta} \frac{dE_g}{dt} \quad (\text{A.52})$$

(A.52) suggests that if the planet emits radiation and gets cool, the planet's total internal energy E_i increase and gravitational energy E_g decrease. If E_g decrease, the planet's radius gets shrink. And if E_i increase, the planet's interior temperature also increase.

I represent the gravitational energy

$$E_g = -\eta \frac{GM_p^2}{R_p} \quad (\text{A.53})$$

where η is a parameter. If I assume polytrope, $\eta = 3/(5 - n)$ according to (A.48). With (A.52) and (A.53), I can find

$$L = \frac{\zeta - 1}{\zeta} \frac{d}{dt} \left(\eta \frac{GM_p^2}{R_p} \right). \quad (\text{A.54})$$

Here I assume η is constant by time, (A.54) can be written

$$\frac{d}{dt} \left(\frac{1}{R_p} \right) = \frac{\zeta}{\zeta - 1} \cdot \frac{L}{\eta GM_p^2} \quad (\text{A.55})$$

(A.55) represents the shrinkage rate of the planetary radius. If The right hand side of (A.55) is positive, $1/R_p$ becomes large and then the planet's radius R_p becomes small.

I integrate (A.55) by time whose range is $[t_0, t]$. I assume the planet's luminosity $L = 4\pi\sigma T_{\text{int}}^4$ where T_{int} is intrinsic temperature and σ is Stefan-Boltzmann constant. Here I assume T_{int} is constant if $t = [t_0, t]$. Then (A.55) can be written

$$\left(\frac{1}{R_p(t)} \right)^3 = \left(\frac{1}{R_p(t_0)} \right)^3 + \frac{\zeta}{\zeta - 1} \cdot \frac{12\pi\sigma T_{\text{int}}^4}{\eta GM_p^2} \cdot (t - t_0) \quad (\text{A.56})$$

where $R_p(t)$ is the planet's radius at t . I define the Kelvin-Helmholtz timescale:

$$\tau_{\text{KH}} = \frac{|E_g|}{L} = \frac{\eta GM_p^2}{4\pi R_p^3 \sigma T_{\text{int}}^4}. \quad (\text{A.57})$$

With (A.56) and (A.57), I can find

$$R_p(t) = R_p(t_0) \left(1 + 3 \frac{\zeta}{\zeta - 1} \frac{\Delta t}{\tau_{\text{KH},0}} \right)^{-1/3} \quad (\text{A.58})$$

where $\Delta t = t - t_0$ and

$$\tau_{\text{KH},0} = \frac{\eta GM_p^2}{4\pi\sigma R_p^3(t_0)T_{\text{int}}^4(t_0)}. \quad (\text{A.59})$$

If $\tau_{\text{KH},0} \gg 3\zeta\Delta t/(\zeta - 1)$, (A.58) can be written approximately

$$R_p(t) \approx R_p(t_0) \left(1 - \frac{\zeta}{\zeta - 1} \cdot \frac{\Delta t}{\tau_{\text{KH},0}} \right). \quad (\text{A.60})$$

Therefore, the planet's cooling causes the shrinkage of planetary radius. However, ζ is not constant through the interior of the real planet because ζ probably change in the planetary interior, And τ_{KH} changes by time because the gravitational energy and planet's luminosity are not constant by time. I have to numerically integrate the interior structure of the planet to estimate the planet's shrinkage.

Here we explain the dependence of the initial luminosity on the thermal evolution of the planet. The basic theory is summarized by Hubbard (1977). We assume the atmospheric structure is described by

$$T = T(g, T, \rho) = A(g)T_{\text{eff}}^\beta \rho^\gamma, \quad (\text{A.61})$$

where $A(g)$ is a function of the surface gravity g , ρ is the density, T is the temperature, T_{eff} is the effective temperature, and γ is the Gruneisen parameter. β is determined by the atmospheric model. For example, $\beta = 0$ means the radiation limit regime which indicate that the outgoing flux from the top of atmosphere F_{top} is constant even though the bottom temperature of atmosphere is changed. $\beta = 1$ means the black body limit which indicate that the ground temperature denote the radiation field. The atmosphere grid calculated by Hubbard and Macfarlane (1980) indicated $\beta = 1.243$ while that calculated by Leconte and Chabrier (2013) indicated $\beta = 0.454 - 2.09$ for Jupiter and $\beta = 0.293 - 2.31$ for Saturn. Here we assume $0 < \beta < 4$. The thermal evolution of the planet is described by the energy conservation (see § 2.2.3). Using the thermodynamical relation $dS = \left(\frac{\partial S}{\partial T}\right)_\rho dT + \left(\frac{\partial S}{\partial \rho}\right)_T d\rho = C_v[dT - \left(\frac{\partial T}{\partial \rho}\right)_S d\rho]$, we can rewrite

$$4\pi\sigma R_p^2 T_{\text{eff}}^4 = \int dM_r C_v \left[\frac{dT}{dt} - \left(\frac{\partial T}{\partial \rho}\right)_S \frac{d\rho}{dt} \right], \quad (\text{A.62})$$

where R_p is the planetary radius, C_v is the heat capacity, and σ is the Stevan-Boltzmann constant. Here we assume R_p is constant and $\frac{d\rho}{dt} = 0$ for simplification, We can find that

$$dt = - \left[\frac{1}{4\pi\sigma R_p^2} \int C_v \frac{1}{T_{\text{eff}}^4} dM_r \right] dT \quad (\text{A.63})$$

$$= - \left[\frac{1}{4\pi\sigma R_p^2} \int C_v \left(\frac{\partial \ln T}{\partial \ln T_{\text{eff}}} \right) T dM_r \right] \frac{dT_{\text{eff}}}{T_{\text{eff}}^5} \quad (\text{A.64})$$

Here we substitute $\left(\frac{\partial \ln T}{\partial \ln T_{\text{eff}}} \right) = \beta$ and we set $\alpha = \frac{1}{4\pi\sigma R_p^2} \int C_v \beta A(g) \rho^\gamma dM_r$. Here we assume α and β are constant and then we can find

$$dt = -\alpha T_{\text{eff}}^{\beta-5} dT_{\text{eff}}. \quad (\text{A.65})$$

Then we obtain

$$t - t_0 = -\frac{\alpha}{\beta - 4} \left[T_{\text{eff}}^{\beta-4} - T_{\text{eff},0}^{\beta-4} \right], \quad (\text{A.66})$$

where $T_{\text{eff},0}$ is the initial effective temperature ($T_{\text{eff},0} = T_{\text{eff}}(t = t_0)$) and t_0 is the initial time ($t_0 = 0$). The we can rewrite

$$T_{\text{eff}} = \left[\frac{1}{\frac{4-\beta}{\alpha} t + \left(\frac{1}{T_{\text{eff},0}} \right)^{4-\beta}} \right]^{\frac{1}{4-\beta}}. \quad (\text{A.67})$$

α can be written as

$$\alpha = \frac{\beta T_{\text{eff},0}^{4-\beta}}{4\pi\sigma R_p^2 T_{\text{eff},0}^4} \int C_v T dM_r \quad (\text{A.68})$$

$$\sim \frac{E}{L_{p,0}} \beta T_{\text{eff},0}^{4-\beta} \sim \tau_{\text{KH},0} \beta T_{\text{eff},0}^{4-\beta}. \quad (\text{A.69})$$

We can find that

$$\left(\frac{T_{\text{eff}}}{T_{\text{eff},0}} \right)^{4-\beta} = \frac{1}{\frac{4-\beta}{\beta} \frac{t}{\tau_{\text{KH},0}} + 1}. \quad (\text{A.70})$$

This equation suggests the thermal evolution of the initial state. If $t > \tau_{\text{KH},0}$, the effective temperature is not affected by the initial effective temperature $T_{\text{eff},0}$. However, if $t < \tau_{\text{KH},0}$, the effective temperature is strongly affected by the initial effective temperature.

Appendix B

Derivation of K_{tide}

In this section, I summarize the derivation of the Roche lobe effect for the mass loss K_{tide} . The form of K_{tide} is derived by Erkaev et al. (2007).

I set the host star mass M_s , the planet's mass M_p and the distance between the two objects a . I consider the system of rotating axis and its center is the center of masses. I set a test particle whose distance from the planet r_a , the host star r_b and the center of the planet and the host star s respectively. In the rotating coordinate system, the energy per unit mass of a test particle in the ecliptic plane is written

$$\Phi = -\frac{GM_p}{r_a} - \frac{GM_s}{r_b} - \frac{G(M_p + M_s)s^2}{a^3} \quad (\text{B.1})$$

where G is the gravitational constant. I set dimensionless quantities in this section

$$\delta = \frac{M_p}{M_s}; \lambda = \frac{a}{R_p}; \eta = \frac{r_a}{R_p} \quad (\text{B.2})$$

where R_p is the planet's radius. I assume $a \gg R_p$. I consider a test particle is on the line which is drawn by the host star and the planet. Then r_b and s can be written

$$r_b = a - r_a, \quad (\text{B.3})$$

$$s = \frac{M_s}{M_s + M_p}a - r_a. \quad (\text{B.4})$$

Therefore (B.1) can be written

$$\Phi(\eta) = \Phi_0 \left[-\frac{1}{\eta} - \frac{1}{\delta(\lambda - \eta)} - \frac{\delta + 1}{\delta} \left(\frac{\lambda}{1 + \delta} - \eta \right)^2 \frac{1}{2\lambda^2} \right], \quad (\text{B.5})$$

$$\Phi_0 = \frac{GM_p}{R_p}. \quad (\text{B.6})$$

I consider the Roche lobe size as

$$r_{\text{RL}} \approx \left(\frac{\delta}{3} \right)^{1/3} a, \quad (\text{B.7})$$

which I assume the zero velocity curve surrounded by L_1 and L_2 is a circular shape. With (B.6) and (B.7), η on the boundary of the Roche lobe can be written

$$\eta = \left[\frac{M_s}{M_s + M_p} a - \left(\frac{\delta}{3} \right)^{1/3} a \right] / R_p = \left[\frac{1}{1 + \delta} - \left(\frac{\delta}{3} \right)^{1/3} \right] \lambda. \quad (\text{B.8})$$

The difference of the potential $\Delta\Phi$ between the planet's surface and the point whose distance from the planet's center r_a can be written

$$\begin{aligned} \Delta\Phi &= \Phi(\eta) - \Phi(\eta = 1) \\ &= \Phi_0 \cdot \frac{\eta - 1}{\eta} \left[1 - \frac{\eta}{\delta\lambda^2} \cdot \frac{\lambda(1 + \eta) - \eta}{(\lambda - 1)(\lambda - \eta)} - \frac{(1 + \delta)\eta(1 + \eta)}{2\delta\lambda^3} \right]. \end{aligned} \quad (\text{B.9})$$

Note that $\lambda = a/R_p \gg 1$ and $\delta = M_p/M_s \ll 1$, (B.10) can be written approximately

$$\Delta\Phi = \Phi_0 \frac{\eta - 1}{\eta} \left[1 - \frac{3}{2} \cdot \frac{\eta(1 + \eta)}{\delta\lambda^3} \right]. \quad (\text{B.10})$$

Provided that $r_a = r_{\text{RL}}$, (B.7) can be written

$$\eta = \frac{r_{\text{RL}}}{R_p} = \left(\frac{\delta}{3} \right)^{1/3} \frac{a}{R_p} \Leftrightarrow \lambda = \left(\frac{3}{\delta} \right)^{1/3} \eta. \quad (\text{B.11})$$

With (B.10) and (B.11), $\Delta\Phi$ can be written

$$\Delta\Phi = \Phi_0 \left(1 - \frac{3}{2} \cdot \frac{1}{\eta} + \frac{1}{2} \cdot \frac{1}{\eta^3} \right) = \frac{GM_p K_{\text{tide}}}{R_p} \quad (\text{B.12})$$

where

$$K_{\text{tide}} = 1 - \frac{3}{2} \cdot \frac{1}{\eta} + \frac{1}{2} \cdot \frac{1}{\eta^3}. \quad (\text{B.13})$$

I consider the mass loss by use of the energy conservation. I set the XUV energy flux I_{XUV} which drive the mass loss. Provided that I_{XUV} carries a gas particle from the planetary surface R_p to its Roche lobe radius r_{RL} , the mass loss per unit time \dot{M}_p can be written

$$\dot{M}_p \Delta\Phi = I_{\text{XUV}}. \quad (\text{B.14})$$

I_{XUV} can be written

$$I_{\text{XUV}} = \epsilon' F_{\text{XUV}} \cdot \pi R_{\text{XUV}}^2 \quad (\text{B.15})$$

where ϵ' is the mass loss efficiency which is related to the heat efficiency of the atmospheric molecules, F_{XUV} is the XUV flux per unit time and unit area and πR_{XUV}^2 is the fronted projected area against the XUV flux. Here I put $\epsilon' \cdot \pi R_{\text{XUV}}^2 = \epsilon \cdot \pi R_p^2$. With (B.12) and (B.15),

$$\dot{M}_p = \frac{\epsilon F_{\text{XUV}} \cdot \pi R_p^2}{\Delta\Phi} = \frac{\epsilon F_{\text{XUV}} \cdot \pi R_p^3}{GM_p K_{\text{tide}}} = \frac{3\epsilon F_{\text{XUV}}}{4G\bar{\rho} K_{\text{tide}}} \quad (\text{B.16})$$

where $\bar{\rho}$ is the planet's mean density; $\bar{\rho} = 4\pi R_p^3/(3M_p)$. Provided that $\eta \rightarrow 1$ which means $R_p \rightarrow r_{\text{RL}}$, I can find $K_{\text{tide}} \rightarrow 0$. That is, $\dot{M}_p \rightarrow \infty$ because Φ at the surface of the planet become 0 if the planet's radius is equal to its Roche lobe radius.

Appendix C

EOS data table

Below I describe how to interoperate the EOS data table. One input the pressure P_0 and the temperature T_0 and derive thermodynamical values, such as the density ρ and the entropy S . We find the data table values $(\hat{P}_1, \hat{P}_2, \hat{T}_1, \hat{T}_2)$ which satisfies

$$\hat{P}_1 < P_0 < \hat{P}_2, \quad (\text{C.1})$$

$$\hat{T}_1 < T_0 < \hat{T}_2. \quad (\text{C.2})$$

and then we also derive from the table

$$(\hat{P}_1, \hat{T}_1) \rightarrow \hat{S}_{11}, \hat{\rho}_{11}, \quad (\text{C.3})$$

$$(\hat{P}_1, \hat{T}_2) \rightarrow \hat{S}_{12}, \hat{\rho}_{12}, \quad (\text{C.4})$$

$$(\hat{P}_2, \hat{T}_1) \rightarrow \hat{S}_{21}, \hat{\rho}_{21}, \quad (\text{C.5})$$

$$(\hat{P}_2, \hat{T}_2) \rightarrow \hat{S}_{22}, \hat{\rho}_{22}. \quad (\text{C.6})$$

To derive the thermodynamical value $\rho(P_0, T_0)$ and $S(P_0, T_0)$, I interpolate (C.3)-(C.6) by the plane

$$\ln \rho(P_0, T_0) = A_\rho + B_\rho \cdot (\ln P_0) + C_\rho \cdot (\ln T_0) + D_\rho (\ln P_0) \cdot (\ln T_0) \quad (\text{C.7})$$

and

$$S(P_0, T_0) = A_S + B_S \cdot (\ln P_0) + C_S \cdot (\ln T_0) + D_S (\ln P_0) \cdot (\ln T_0) \quad (\text{C.8})$$

To determine coefficients $(A_\rho, B_\rho, C_\rho, D_\rho)$ and (A_S, B_S, C_S, D_S) , one solve simultaneous equations;

$$\begin{pmatrix} 1 & \ln \hat{P}_1 & \ln \hat{T}_1 & \ln \hat{P}_1 \cdot \ln \hat{T}_1 \\ 1 & \ln \hat{P}_1 & \ln \hat{T}_2 & \ln \hat{P}_1 \cdot \ln \hat{T}_2 \\ 1 & \ln \hat{P}_2 & \ln \hat{T}_1 & \ln \hat{P}_2 \cdot \ln \hat{T}_1 \\ 1 & \ln \hat{P}_2 & \ln \hat{T}_2 & \ln \hat{P}_2 \cdot \ln \hat{T}_2 \end{pmatrix} \cdot \begin{pmatrix} A_\rho \\ B_\rho \\ C_\rho \\ D_\rho \end{pmatrix} = \begin{pmatrix} \ln \hat{\rho}_{11} \\ \ln \hat{\rho}_{12} \\ \ln \hat{\rho}_{21} \\ \ln \hat{\rho}_{22} \end{pmatrix}, \quad (\text{C.9})$$

and

$$\begin{pmatrix} 1 & \ln \hat{P}_1 & \ln \hat{T}_1 & \ln \hat{P}_1 \cdot \ln \hat{T}_1 \\ 1 & \ln \hat{P}_1 & \ln \hat{T}_2 & \ln \hat{P}_1 \cdot \ln \hat{T}_2 \\ 1 & \ln \hat{P}_2 & \ln \hat{T}_1 & \ln \hat{P}_2 \cdot \ln \hat{T}_1 \\ 1 & \ln \hat{P}_2 & \ln \hat{T}_2 & \ln \hat{P}_2 \cdot \ln \hat{T}_2 \end{pmatrix} \cdot \begin{pmatrix} A_S \\ B_S \\ C_S \\ D_S \end{pmatrix} = \begin{pmatrix} \hat{S}_{11} \\ \hat{S}_{12} \\ \hat{S}_{21} \\ \hat{S}_{22} \end{pmatrix}. \quad (\text{C.10})$$

We can also derive adiabatic temperature $T(P, S)$ from the EOS data table. This is resemble to how to derive $\rho(P, T)$ and $S(P, T)$ One input the pressure P_0 and the specific entropy \bar{S} and derive the temperature $T(P_0, \bar{S})$ We search the data table values $(\hat{P}_1, \hat{P}_2, \hat{S}_{11}, \hat{S}_{12}, \hat{S}_{21}, \hat{S}_{22})$ which satisfies

$$\hat{P}_1 < P_0 < \hat{P}_2, \quad (\text{C.11})$$

$$\hat{S}_{\min} < \bar{S} < \hat{S}_{\max}. \quad (\text{C.12})$$

where $\hat{S}_{\min} = \min(\hat{S}_{11}, \hat{S}_{12}, \hat{S}_{21}, \hat{S}_{22})$ and $\hat{S}_{\max} = \max(\hat{S}_{11}, \hat{S}_{12}, \hat{S}_{21}, \hat{S}_{22})$. Then we also derive from the table

$$(\hat{P}_1, \hat{S}_{11}) \rightarrow \hat{T}_{11}, \quad (\text{C.13})$$

$$(\hat{P}_1, \hat{S}_{12}) \rightarrow \hat{T}_{12}, \quad (\text{C.14})$$

$$(\hat{P}_2, \hat{S}_{21}) \rightarrow \hat{T}_{21}, \quad (\text{C.15})$$

$$(\hat{P}_2, \hat{S}_{22}) \rightarrow \hat{T}_{22}. \quad (\text{C.16})$$

I interpolate (C.13)-(C.16) by the plane;

$$\ln T(P_0, \bar{S}) = A_T + B_T \cdot (\ln P_0) + C_T \cdot \bar{S} + D_T (\ln P_0) \cdot \bar{S}. \quad (\text{C.17})$$

To determine coefficients (A_T, B_T, C_T, D_T) , one solve simultaneous equations;

$$\begin{pmatrix} 1 & \ln \hat{P}_1 & \bar{S}_{11} & \ln \hat{P}_1 \cdot \bar{S}_{11} \\ 1 & \ln \hat{P}_1 & \hat{S}_{12} & \ln \hat{P}_1 \cdot \bar{S}_{12} \\ 1 & \ln \hat{P}_2 & \bar{S}_{21} & \ln \hat{P}_2 \cdot \bar{S}_{21} \\ 1 & \ln \hat{P}_2 & \bar{S}_{22} & \ln \hat{P}_2 \cdot \bar{S}_{22} \end{pmatrix} \cdot \begin{pmatrix} A_T \\ B_T \\ C_T \\ D_T \end{pmatrix} = \begin{pmatrix} \ln \hat{T}_{11} \\ \ln \hat{T}_{12} \\ \ln \hat{T}_{21} \\ \ln \hat{T}_{22} \end{pmatrix}, \quad (\text{C.18})$$

I use Gaussian elimination method to solve Eqs.(C.9), (C.10) and (C.18).

Appendix D

Analytical formula for the chord optical depth of the isothermal plane-parallel atmosphere

I assume the atmosphere is plain parallel structure;

$$\frac{dP}{dz} = -g\rho \quad (\text{D.1})$$

where g is the planet's gravity and ρ is the density. I assume g is constant through the atmosphere. If I assume the temperature of the atmosphere is constant, (3.28) can be written

$$z(P_r, P_z) = \frac{\mathcal{R}T}{\mu g} \ln \frac{P_r}{P_z} = H \ln \frac{P_r}{P_z} \quad (\text{D.2})$$

where H is the scale height $H := P/|dP/dz| = \mathcal{R}T/(\mu g)$.

Here I describe the analytical solution of the transit radius. The chord optical depth can be written

$$\tau_{\text{ch}} = 2 \int_0^\infty \kappa_\nu \rho \frac{z+r}{\sqrt{z^2+2zr}} dz \quad (\text{D.3})$$

I assume κ_ν is constant for simplicity. With (D.1), (D.3) can be written

$$\tau_{\text{ch}} = -\frac{2\kappa}{g} \int_{P_r}^0 \frac{1+z/r}{\sqrt{(z/r)^2+2z/r}} dP. \quad (\text{D.4})$$

With (D.2), (D.4) can be written by use of change of variables from P to z ,

$$\tau_{\text{ch}} = -\frac{2\kappa}{g} \int_0^\infty \frac{1+z/r}{\sqrt{(1+z/r)^2-1}} \cdot \left(\frac{-P_r}{H} e^{-z/H} \right) dz. \quad (\text{D.5})$$

Therefore (D.3) can be written

$$\tau_{\text{ch}} = 2\kappa_\nu \rho_r \int_0^\infty \frac{1+z/r}{\sqrt{(1+z/r)^2-1}} e^{-z/H} dz \quad (\text{D.6})$$

where $\rho_r = \frac{\mu P_r}{RT}$, which I assume the ideal gas. To evaluate (D.6), I change of variables from $1+z/r$ to X of the integral part of (D.6). Then I can find

$$\tau_{\text{ch}} = 2\kappa_\nu \rho_r r \int_1^\infty \frac{X}{\sqrt{X^2-1}} e^{-r(X-1)/H} dz. \quad (\text{D.7})$$

By use of partial integral, (D.7) can be written

$$\begin{aligned} \tau_{\text{ch}} &= 2\kappa_\nu \rho_r r \left\{ \left[\sqrt{X^2-1} e^{-r(X-1)/H} \right]_1^\infty \right. \\ &\quad \left. - \int_1^\infty \frac{-r}{H} \sqrt{X^2-1} e^{-r(X-1)/H} dz \right\}, \\ &= 2\kappa_\nu \rho_r \frac{r^2}{H} \int_1^\infty \sqrt{X^2-1} e^{-r(X-1)/H} dz \\ &= 2\kappa_\nu \rho_r \frac{r^2}{H} \int_0^\infty \sqrt{t^2+2t} e^{-(r/H)t} dt, \end{aligned} \quad (\text{D.8})$$

where $X-1=t$. (D.8) has finite value. I make use of Laplace transform to evaluate the integral part of (D.8);

$$\int_0^\infty \sqrt{t^2+2t} e^{-(r/H)t} dt = \int_0^\infty f(t) e^{-pt} dt \quad (\text{D.9})$$

where $p=r/H$ and $f(t) = \sqrt{t^2+2t}$. Then we can derive

$$\int_0^\infty (t^2+2at)^\alpha e^{-pt} dt = \frac{\Gamma(\alpha+1)}{\sqrt{\pi}} \left(\frac{2a}{p} \right)^{\alpha+1/2} e^{ap} K_{\alpha+1/2}(ap) \quad (\text{D.10})$$

where Γ is the gamma function and K_α is the modified Bessel function. In general, the

modified Bessel function is

$$K_\alpha(x) = \frac{\pi I_{-\alpha}(x) - I_\alpha(x)}{2 \sin \alpha\pi}, \quad (\text{D.11})$$

$$I_\alpha(x) = \sum_{n=0}^{\infty} \frac{(x/2)^{\alpha+2n}}{n! \Gamma(\alpha + n + 1)}. \quad (\text{D.12})$$

In the case of (D.9), $\alpha = 1/2$ and $a = 1$. $K_1(x)$ can be written

$$K_1(x) = I_1(x) \left(\log \frac{x}{2} + \gamma \right) - \frac{1}{2} \sum_{k=0}^{\infty} \frac{(x/2)^{1+2k}}{k!(n+k)!} \left[\sum_{m=1}^k \frac{1}{m} + \sum_{m=1}^{k+n} \frac{1}{m} \right] \quad (\text{D.13})$$

where γ is Euler's constant. Therefore I can derive

$$\begin{aligned} \int_0^{\infty} (t^2 + 2t)^{1/2} e^{-(r/H)t} dt &= \frac{\Gamma(1/2 + 1)}{\sqrt{\pi}} \left(\frac{2H}{r} \right)^{1/2+1/2} e^{r/H} K_{1/2+1/2}(r/H) \\ &= \frac{H}{r} e^{r/H} K_1 \left(\frac{r}{H} \right) \end{aligned} \quad (\text{D.14})$$

With (D.8) and (D.14),

$$\tau_{\text{ch}} = 2\kappa_\nu \rho_r r e^{r/H} K_1 \left(\frac{r}{H} \right). \quad (\text{D.15})$$

The asymptotic expansion of the modified Bessel function $K_\alpha(x)$ can be written

$$\begin{aligned} K_\alpha(x) &\approx \sqrt{\frac{\pi}{2x}} e^{-x} \sum_{n=0}^{\infty} \frac{\Gamma(\alpha + n + 1/2)}{n! \Gamma(\alpha - n + 1/2)} \frac{1}{(2x)^n} \\ &\approx \sqrt{\frac{\pi}{2x}} e^{-x} \left(1 + \frac{4\alpha^2 - 1}{8x} + \frac{(4\alpha^2 - 1)(4\alpha^2 - 9)}{2!(8x)^2} \right. \\ &\quad \left. + \frac{(4\alpha^2 - 1)(4\alpha^2 - 9)(4\alpha^2 - 25)}{3!(8x)^3} + \dots \right) \end{aligned} \quad (\text{D.16})$$

when x is large enough. Therefore

$$K_1 \left(\frac{r}{H} \right) \approx \sqrt{\frac{\pi H}{2r}} e^{-(r/H)} \left\{ 1 + \frac{3}{8} \left(\frac{H}{r} \right) - \frac{15}{128} \left(\frac{H}{r} \right)^2 + \frac{105}{1024} \left(\frac{H}{r} \right)^3 + \dots \right\} \quad (\text{D.17})$$

With (D.15) and (D.17),

$$\tau_{\text{ch}} \approx \sqrt{2\pi} \kappa_\nu \rho_r \sqrt{rH} \left\{ 1 + \frac{3}{8} \left(\frac{H}{r} \right) - \frac{15}{128} \left(\frac{H}{r} \right)^2 + \frac{105}{1024} \left(\frac{H}{r} \right)^3 + \dots \right\}. \quad (\text{D.18})$$

Appendix E

Analytical formula for the chord optical depth of the isothermal spheric symmetric atmosphere

Here I describe the analytical formula of the chord optical depth for the isothermal spheric symmetric atmosphere.

According to (3.2.6) The spheric symmetric atmosphere is

$$\tau_{\text{ch}}(\nu, r) = -\frac{2}{g} \int_{P_r}^0 \kappa_\nu \frac{(1 + z/r)^2}{\sqrt{1 - (1 + z/r)^{-2}}} dP. \quad (\text{E.1})$$

$$z = z_p \left(1 - \frac{z_p}{r}\right)^{-1}, \quad (\text{E.2})$$

and

$$z_p(P_r, P) = -\frac{\mathcal{R}}{\mu g} \int_{P_r}^P \frac{T}{P} dP. \quad (\text{E.3})$$

I assume the planet's atmosphere is isothermal. Then (E.3) can be written

$$z_p(P_r, P) = \frac{\mathcal{R}T}{\mu g} \ln \frac{P_r}{P} = H \ln \frac{P_r}{P}. \quad (\text{E.4})$$

where $H = \frac{\mathcal{R}T}{\mu g}$. Here I assume κ_ν is constant for the simplicity. With (E.3), (E.4), I can find

$$\frac{dP}{dz} = -\frac{P_r \exp\left(-\frac{r}{H} \frac{z}{r+z}\right)}{H (1 + z/r)^2} \quad (\text{E.5})$$

Then (E.1) can be written

$$\tau_{\text{ch}} = \frac{2\kappa_\nu P_r}{gH} \int_0^\infty \frac{1 + z/r)^2}{\sqrt{(1 + z/r)^2 - 1}} \exp\left(-\frac{r}{H} \frac{z}{r + z}\right) dz. \quad (\text{E.6})$$

where $\rho_r = P_r/(gH) = (\mu P_r)/(\mathcal{R}T)$ I make use of change variables and consequently find

$$\tau_{\text{ch}} = 2\kappa_\nu \rho_r \frac{r^2}{H} e^{-r/H} \int_1^\infty \frac{\sqrt{X^2 - 1}}{X^2} \exp\left(\frac{r}{H} \frac{1}{x}\right) dX. \quad (\text{E.7})$$

Appendix F

Atmospheric model for Chapter 3

We demonstrate the opacity models for the water vapor atmosphere. We define the Planck (κ^P) and the Rosseland mean opacities (κ^r) as

$$\kappa_v^P = \int_{\text{visible}} \kappa_\nu B_\nu(T_\star) d\nu \bigg/ \int_{\text{visible}} B_\nu(T_\star) d\nu, \quad (\text{F.1})$$

$$\frac{1}{\kappa_v^r} = \int_{\text{visible}} \frac{1}{\kappa_\nu} \frac{dB_\nu(T_\star)}{dT} d\nu \bigg/ \int_{\text{visible}} \frac{dB_\nu(T_\star)}{dT} d\nu, \quad (\text{F.2})$$

$$\kappa_{\text{th}}^P = \int_{\text{thermal}} \kappa_\nu B_\nu(T_{\text{atm}}) d\nu \bigg/ \int_{\text{thermal}} B_\nu(T_{\text{atm}}) d\nu, \quad (\text{F.3})$$

$$\frac{1}{\kappa_{\text{th}}^r} = \int_{\text{thermal}} \frac{1}{\kappa_\nu} \frac{dB_\nu(T_{\text{atm}})}{dT} d\nu \bigg/ \int_{\text{thermal}} \frac{dB_\nu(T_{\text{atm}})}{dT} d\nu, \quad (\text{F.4})$$

where ν is the frequency, κ_ν the monochromatic opacity at a given ν , T_\star the stellar effective temperature, T_{atm} the atmospheric temperature of the planet, and B_ν the Planck function. The subscripts, "th" and "v", mean opacities in the thermal and visible wavelengths, respectively. In this study, we assume $T_\star = 5780$ K. We use HITRAN line profile data for water (Rothman et al., 2009) and calculate mean opacities for 1000 K, 2000 K, and 3000 K at 1, 10, 100 bar. The mean opacities are fitted to power-law functions of P and

T , using the least squares method;

$$\kappa_{\text{v}}^{\text{p}} = 1.94 \times 10^4 \left(\frac{P}{1\text{bar}} \right)^{0.01} \left(\frac{T}{1000\text{K}} \right)^{1.0} \text{ cm}^2 \text{ g}^{-1}, \quad (\text{F.5})$$

$$\kappa_{\text{v}}^{\text{r}} = 2.20 \left(\frac{P}{1\text{bar}} \right)^{1.0} \left(\frac{T}{1000\text{K}} \right)^{-0.4} \text{ cm}^2 \text{ g}^{-1}, \quad (\text{F.6})$$

$$\kappa_{\text{th}}^{\text{p}} = 4.15 \times 10^5 \left(\frac{P}{1\text{bar}} \right)^{0.01} \left(\frac{T}{1000\text{K}} \right)^{-1.1} \text{ cm}^2 \text{ g}^{-1}, \quad (\text{F.7})$$

$$\kappa_{\text{th}}^{\text{r}} = 3.07 \times 10^2 \left(\frac{P}{1\text{bar}} \right)^{0.9} \left(\frac{T}{1000\text{K}} \right)^{-4.0} \text{ cm}^2 \text{ g}^{-1}, \quad (\text{F.8})$$

where P is the pressure and T the temperature.

In this study, we follow the prescription developed by Guillot (2010) basically, except for the treatment of the opacity. We consider a static, plane-parallel atmosphere in local thermodynamic equilibrium. We assume that the atmosphere is in radiative equilibrium between an incoming visible flux from the star and an outgoing infrared flux from the planet. Thus, the radiation energy equation and radiation momentum equation are written as

$$\frac{dH_{\text{v}}}{dm} = \kappa_{\text{v}}^{\text{p}} J_{\text{v}}, \quad (\text{F.9})$$

$$\frac{dK_{\text{v}}}{dm} = \kappa_{\text{v}}^{\text{r}} H_{\text{v}}, \quad (\text{F.10})$$

$$\frac{dH_{\text{th}}}{dm} = \kappa_{\text{th}}^{\text{p}} (J_{\text{th}} - B), \quad (\text{F.11})$$

$$\frac{dK_{\text{th}}}{dm} = \kappa_{\text{th}}^{\text{r}} H_{\text{th}}, \quad (\text{F.12})$$

and the atmosphere in radiative equilibrium satisfies

$$\kappa_{\text{v}}^{\text{p}} J_{\text{v}} + \kappa_{\text{th}}^{\text{p}} (J_{\text{th}} - B) = 0, \quad (\text{F.13})$$

where J_{v} (J_{th}), H_{v} (H_{th}), and K_{v} (K_{th}) are, respectively, the zeroth, first, and second-order moments of radiation intensity in the visible (thermal) wavelengths, m the atmospheric mass coordinate, $dm = \rho dz$, where z is the altitude from the bottom of the

atmosphere and ρ the density, and B the frequency-integrated Planck function,

$$B \equiv \int_{\text{thermal}} B_\nu d\nu \sim \frac{\sigma}{\pi} T^4, \quad (\text{F.14})$$

where σ is the Stefan-Boltzmann constant. We here assume that thermal emission from the atmosphere at visible wavelengths are negligible, so that $B_\nu \sim 0$ in the visible region. The six moments of the radiation field are defined as

$$(J_v, H_v, K_v) \equiv \int_{\text{visible}} (J_\nu, H_\nu, K_\nu) d\nu, \quad (\text{F.15})$$

$$(J_{\text{th}}, H_{\text{th}}, K_{\text{th}}) \equiv \int_{\text{thermal}} (J_\nu, H_\nu, K_\nu) d\nu, \quad (\text{F.16})$$

where J_ν is the mean intensity, $4\pi H_\nu$ the radiation flux, and $4\pi K_\nu/c$ the radiation pressure (c is the speed of light).

We integrate three moments of specific intensity, J_ν , H_ν and K_ν , over all the frequencies:

$$J \equiv \int_0^\infty J_\nu d\nu = \frac{1}{2} \int_0^\infty d\nu \int_{-1}^1 d\mu I_{\nu,\mu} = J_v + J_{\text{th}}, \quad (\text{F.17})$$

$$H \equiv \int_0^\infty H_\nu d\nu = \frac{1}{2} \int_0^\infty d\nu \int_{-1}^1 d\mu I_{\nu,\mu} \mu = H_v + H_{\text{th}}, \quad (\text{F.18})$$

$$K \equiv \int_0^\infty K_\nu d\nu = \frac{1}{2} \int_0^\infty d\nu \int_{-1}^1 d\mu I_{\nu,\mu} \mu^2 = K_v + K_{\text{th}}, \quad (\text{F.19})$$

where $I_{\nu,\mu}$ is the specific intensity and θ the angle of a intensity with respect to the z -axis, $\mu = \cos \theta$. The energy conservation of the total flux implies

$$H = H_v + H_{\text{th}} = \frac{1}{4\pi} \sigma T_{\text{int}}^4, \quad (\text{F.20})$$

where T_{irr} is the irradiation temperature given by

$$T_{\text{irr}} = T_\star \sqrt{\frac{R_\star}{a}}, \quad (\text{F.21})$$

where R_\star is the radius of the host star and a the semimajor axis.

For the closure relations, we use the Eddington approximation (e.g. Chandrasekhar

1960), namely,

$$K_v = \frac{1}{3}J_v, \quad (\text{F.22})$$

$$K_{\text{th}} = \frac{1}{3}J_{\text{th}}. \quad (\text{F.23})$$

For an isotropic case of both the incoming and outgoing radiation fields, we find boundary conditions of the moment equations as follows (see also Guillot 2010 for details);

$$H_v(m=0) = -\frac{1}{\sqrt{3}}\frac{1}{4\pi}\sigma T_{\text{irr}}^4, \quad (\text{F.24})$$

$$H_v(m=0) = -\frac{1}{\sqrt{3}}J_v(m=0), \quad (\text{F.25})$$

$$H_{\text{th}}(m=0) = \frac{1}{2}J_{\text{th}}(m=0). \quad (\text{F.26})$$

Thus, we integrate Eqs.(F.9)-(F.13) over m numerically, using mean opacities of (F.5)-(F.8) and boundary conditions of (F.24)-(F.26), and then determine a T-P profile of the water vapor atmosphere. We assume that the boundary is at $P_0 = 1 \times 10^{-5}$ bar. The choice of P_0 ($\leq 1 \times 10^{-5}$ bar) has little effect on the atmospheric temperature-pressure structure. T_0 is determined in an iterative fashion, until $\text{abs}(T_0 - [\pi B(m=0, P_0, T_0)/\sigma]^{1/4}) \leq 0.01$ is fulfilled. Then we integrate Eqs. (F.9)-(F.13) over m by the 4th-order Runge-Kutta method, until we find the point where $d \ln T/d \ln P \geq \nabla_{\text{ad}}$. The pressure and temperature, P_{ad} and T_{ad} , are the boundary conditions for the convective-interior structure (see §3.2.1).

In Fig. F.1, we show the P - T profile for the solar-composition atmosphere with $g = 980 \text{ cm s}^{-2}$, $T_{\text{int}} = 300 \text{ K}$ and $T_{\text{irr}} = 1500 \text{ K}$ (dotted line). In this calculation, we take κ_{th}^r and κ_{th}^p as functions of P and T from Freedman et al. (2008) and calculate κ_v^p and κ_v^r , for $P = 1 \times 10^{-3}, 0.1, 1, 10 \text{ bar}$ and $T = 1500 \text{ K}$ from HITRAN and HITEMP data that include H_2 , He, H_2O , CO, CH_4 , Na and K for the solar abundance respectively as

$$\kappa_v = \begin{cases} 1.51 \times 10^{-5} \text{ cm}^2 \cdot \text{g}^{-1} & (10^{-3} \leq P[\text{bar}], \\ 3.88 \times 10^{-4} \text{ cm}^2 \cdot \text{g}^{-1} & (10^{-3} < P[\text{bar}] \leq 10^{-1}), \\ 3.05 \times 10^{-3} \text{ cm}^2 \cdot \text{g}^{-1} & (10^{-1} < P[\text{bar}] \leq 1), \\ 2.65 \times 10^{-2} \text{ cm}^2 \cdot \text{g}^{-1} & (1 > P[\text{bar}]), \end{cases} \quad (\text{F.27})$$

by use of (F.2). The thin and thick parts of the solid line represent the radiative and convective zones, respectively.

In addition, to test our atmosphere model, we compare it with the P - T profile derived by Guillot (2010) with $\gamma = \kappa_v/\kappa_{th} = 0.4$ (solid line), which reproduces more detailed atmosphere models by Fortney et al. (2005) and Iro et al. (2005) (see Fig. 6 of Guillot (2010)). As seen in Fig. F.1, our atmospheric model yields a P - T profile similar to that from Guillot (2010). In our model, temperatures are relatively low compared with the Guillot (2010) model at $P \lesssim 40$ bar, which is due to difference in opacity. In our model, deep regions of $P \gtrsim 40$ bar are convective, while there is no convective region in the Guillot (2010) model, because of constant opacity. We have compare our P - T profile with the Fortney et al. (2005)'s and Iro et al. (2005)'s profiles, which are shown in Fig. 6 of Guillot (2010) and confirmed that our P - T profile in the convective region is almost equal to their profiles. Of special interest in this study is the entropy at the radiative/convective boundary, because it governs the thermal evolution of the planet. In this sense, it is fair to say that our atmospheric model yields appropriate boundary conditions for the structure of the convective interior.

We show an analytical expression for our atmospheric model. κ_v^p and κ_v^r are constant throughout the atmosphere. We differentiate (F.9) and (F.10) by m and obtain

$$\frac{d^2 J_v}{dm^2} = \mu^2 H_v \frac{d\kappa_v^r}{dm} + \frac{\kappa_v^r \kappa_v^p}{\mu^2} J_v, \quad (\text{F.28})$$

$$\frac{d^2 H_v}{dm^2} = J_v \frac{d\kappa_v^p}{dm} + \frac{\kappa_v^r \kappa_v^p}{\mu^2} H_v, \quad (\text{F.29})$$

where $\mu^2 = K_v/J_v$. As Heng et al. (2012) mentioned, it would be a challenging task without assumption of constant κ_v^p and κ_v^r to obtain analytical solutions for J_v and H_v . Assuming $J_v = H_v = 0$ as $m \rightarrow \infty$, we obtain

$$(J_v, H_v) = (J_{v,0}, H_{v,0}) \exp\left(-\frac{\bar{\kappa}_v}{\mu} m\right), \quad (\text{F.30})$$

where $\bar{\kappa}_v = \sqrt{\kappa_v^p \kappa_v^r}$ and $J_{v,0}$ and $H_{v,0}$ are the values of J_v and H_v evaluated at $m = 0$ respectively. In general, the heat transportation such as circulation produces a specific luminosity of heat. Heng et al. (2012) introduced the specific luminosity as Q which has

units of $\text{erg s}^{-1} \text{g}^{-1}$. Q can be related to the moments of the specific intensity and we obtain

$$\kappa_{\text{th}}^{\text{p}} (J_{\text{th}} - B) + \kappa_{\text{v}}^{\text{p}} J_{\text{v}} = Q. \quad (\text{F.31})$$

We integrate Eq. (F.31) and obtain

$$H = H_{\infty} - \tilde{Q}(m, \infty), \quad (\text{F.32})$$

where H_{∞} is the value of H evaluated at $m \rightarrow \infty$ and

$$\tilde{Q}(m_1, m_2) = \int_{m_1}^{m_2} Q(m', \mu, \phi) dm'. \quad (\text{F.33})$$

To obtain H_{th} and J_{th} , we substitute Eq. (F.31) in Eqs. (F.11) and (F.12) and integrate by m . Then we obtain,

$$H_{\text{th}} = H_{\infty} - H_{\text{v},0} \exp\left(-\frac{\bar{\kappa}_{\text{v}}}{\mu} m\right) - \tilde{Q}(m, \infty) \quad (\text{F.34})$$

$$\begin{aligned} J_{\text{th}} &= J_{\text{th},0} - \frac{H_{\text{v},0}}{f_{K\text{th}}} \int_0^m \kappa_{\text{th}}^{\text{r}} \exp\left(-\frac{\bar{\kappa}_{\text{v}}}{\mu} m'\right) dm' \\ &\quad + \frac{1}{f_{K\text{th}}} \int_0^m \kappa_{\text{th}}^{\text{r}} \left\{ H_{\infty} - \tilde{Q}(m', \infty) \right\} dm', \end{aligned} \quad (\text{F.35})$$

where $f_{K\text{th}} = K_{\text{th}}/J_{\text{th}}$, $f_{H\text{th}} = H_{\text{th}}/J_{\text{th}}$ and

$$J_{\text{th},0} = \frac{1}{f_{H\text{th}}} \left\{ H_{\infty} - H_{\text{v},0} - \tilde{Q}(0, \infty) \right\}. \quad (\text{F.36})$$

That is, we obtain

$$\begin{aligned} B &= H_{\infty} \left[\frac{1}{f_{H\text{th}}} + \frac{1}{f_{K\text{th}}} \tau_{\text{th}}(m) \right] \\ &\quad - H_{\text{v},0} \left[\frac{1}{f_{H\text{th}}} + \frac{\bar{\kappa}_{\text{v}}}{\mu \kappa_{\text{th}}^{\text{p}}} + \frac{1}{f_{K\text{th}}} \tau_{\text{ext}}(m) \right] + E(m) \end{aligned} \quad (\text{F.37})$$

where

$$\tau_{\text{th}}(m) = \int_0^m \kappa_{\text{th}}^r dm', \quad (\text{F.38})$$

$$\tau_{\text{ext}}(m) = \int_0^m \left(\bar{\kappa}_{\text{th}}^{-2} - \frac{f_{K\text{th}}}{\mu^2} \bar{\kappa}_{\text{v}}^{-2} \right) \frac{1}{\kappa_{\text{th}}^p} \exp\left(-\frac{\bar{\kappa}_{\text{v}}}{\mu} m'\right) dm', \quad (\text{F.39})$$

$$E(m) = - \left[\frac{Q}{\kappa_{\text{th}}^p} + \frac{1}{f_{K\text{th}}} \int_0^m \kappa_{\text{th}}^r \tilde{Q}(m', \infty) dm' + \frac{\tilde{Q}(0, \infty)}{f_{H\text{th}}} \right] \quad (\text{F.40})$$

and $\bar{\kappa}_{\text{th}} = \sqrt{\kappa_{\text{th}}^p \kappa_{\text{th}}^r}$. In our conditions, we assume $\mu = 1/\sqrt{3}$, $f_{K\text{th}} = 1/3$, $f_{H\text{th}} = 1/2$ and $Q = 0$. Consequently, we obtain the temperature profile as

$$T^4 = \frac{3}{4} T_{\text{int}}^4 \left[\frac{2}{3} + \tau_{\text{th}}(m) \right] + \frac{\sqrt{3}}{4} T_{\text{irr}}^4 \left[\frac{2}{3} + \frac{\bar{\kappa}_{\text{v}}}{\sqrt{3} \kappa_{\text{th}}^p} + \tau_{\text{ext}}(m) \right] \quad (\text{F.41})$$

where

$$\tau_{\text{ext}}(m) = \int_0^m \frac{\bar{\kappa}_{\text{th}}^{-2} - \bar{\kappa}_{\text{v}}^{-2}}{\kappa_{\text{th}}^p} \exp\left(-\sqrt{3} \bar{\kappa}_{\text{v}} m'\right) dm'. \quad (\text{F.42})$$

If we assume $\kappa_{\text{th}}^p = \kappa_{\text{th}}^v$ and $\kappa_{\text{v}}^p = \kappa_{\text{v}}^v$, Eq. (F.41) agrees with Eq. (27) of Heng et al. (2012).

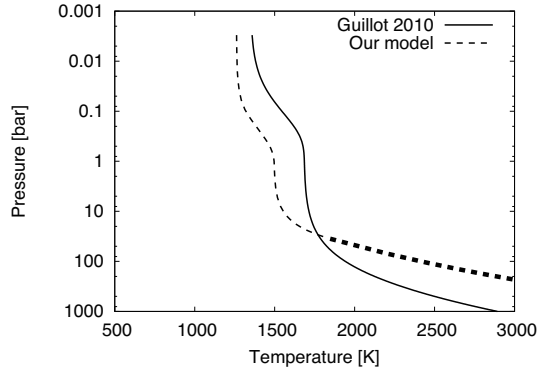


Figure F.1: Temperature-pressure profiles for a solar-composition atmosphere (see the details in text). The solid and dotted lines represent the $\gamma = 0.4$ (Guillot, 2010) and our models, respectively. The thin and thick parts of the lines represent the radiative and convective regions, respectively. We assumed $g = 980 \text{ cm s}^{-2}$, $T_{\text{int}} = 300 \text{ K}$ and $T_{\text{irr}} = 1500 \text{ K}$.

References

- Y. Abe and T. Matsui. Evolution of an Impact-Generated H₂O-CO₂ Atmosphere and Formation of a Hot Proto-Ocean on Earth. *Journal of Atmospheric Sciences*, 45:3081–3101, November 1988. doi: 10.1175/1520-0469(1988)045<3081:EOAIGH>2.0.CO;2.
- E. R. Adams, S. Seager, and L. Elkins-Tanton. Ocean Planet or Thick Atmosphere: On the Mass-Radius Relationship for Solid Exoplanets with Massive Atmospheres. *ApJ*, 673:1160–1164, February 2008. doi: 10.1086/524925.
- Y. Alibert and O. Mousis. Formation of Titan in Saturn’s subnebula: constraints from Huygens probe measurements. *A&A*, 465:1051–1060, April 2007. doi: 10.1051/0004-6361:20066402.
- S. K. Atreya. *Atmospheres and Ionospheres of the Outer Planets and their Satellites*. 1986.
- N. M. Batalha, J. F. Rowe, S. T. Bryson, T. Barclay, C. J. Burke, D. A. Caldwell, J. L. Christiansen, F. Mullally, S. E. Thompson, T. M. Brown, A. K. Dupree, D. C. Fabrycky, E. B. Ford, J. J. Fortney, R. L. Gilliland, H. Isaacson, D. W. Latham, G. W. Marcy, S. N. Quinn, D. Ragozzine, A. Shporer, W. J. Borucki, D. R. Ciardi, T. N. Gautier, III, M. R. Haas, J. M. Jenkins, D. G. Koch, J. J. Lissauer, W. Rapin, G. S. Basri, A. P. Boss, L. A. Buchhave, J. A. Carter, D. Charbonneau, J. Christensen-Dalsgaard, B. D. Clarke, W. D. Cochran, B.-O. Demory, J.-M. Desert, E. Devore, L. R. Doyle, G. A. Esquerdo, M. Everett, F. Fressin, J. C. Geary, F. R. Girouard, A. Gould, J. R. Hall, M. J. Holman, A. W. Howard, S. B. Howell, K. A. Ibrahim, K. Kinemuchi, H. Kjeldsen, T. C. Klaus, J. Li, P. W. Lucas, S. Meibom, R. L. Morris, A. Prša, E. Quintana, D. T. Sanderfer, D. Sasselov, S. E. Seader, J. C. Smith, J. H.

- Steffen, M. Still, M. C. Stumpe, J. C. Tarter, P. Tenenbaum, G. Torres, J. D. Twicken, K. Uddin, J. Van Cleve, L. Walkowicz, and W. F. Welsh. Planetary Candidates Observed by Kepler. III. Analysis of the First 16 Months of Data. *ApJS*, 204:24, February 2013. doi: 10.1088/0067-0049/204/2/24.
- J. Bishop, S. K. Atreya, P. N. Romani, G. S. Orton, B. R. Sandel, and R. V. Yelle. The middle and upper atmosphere of Neptune. In D. P. Cruikshank, M. S. Matthews, and A. M. Schumann, editors, *Neptune and Triton*, pages 427–487, 1995.
- P. Bodenheimer and J. B. Pollack. Calculations of the accretion and evolution of giant planets The effects of solid cores. *Icarus*, 67:391–408, September 1986. doi: 10.1016/0019-1035(86)90122-3.
- E. Böhm-Vitense. Über die Wasserstoffkonvektionszone in Sternen verschiedener Effektivtemperaturen und Leuchtkräfte. Mit 5 Textabbildungen. *ZAp*, 46:108, 1958.
- G. Boué and J. Laskar. A Collisionless Scenario for Uranus Tilting. *ApJ*, 712:L44–L47, March 2010. doi: 10.1088/2041-8205/712/1/L44.
- T. Cavalié, R. Moreno, E. Lellouch, P. Hartogh, O. Venot, G. S. Orton, C. Jarchow, T. Encrenaz, F. Selsis, F. Hersant, and L. N. Fletcher. The first submillimeter observation of CO in the stratosphere of Uranus. *A&A*, 562:A33, February 2014. doi: 10.1051/0004-6361/201322297.
- S. Chandrasekhar. *Radiative transfer*. New York: Dover, 1960, 1960.
- T. Encrenaz, E. Lellouch, P. Drossart, H. Feuchtgruber, G. S. Orton, and S. K. Atreya. First detection of CO in Uranus. *A&A*, 413:L5–L9, January 2004. doi: 10.1051/0004-6361:20034637.
- N. V. Erkaev, Y. N. Kulikov, H. Lammer, F. Selsis, D. Langmayr, G. F. Jaritz, and H. K. Biernat. Roche lobe effects on the atmospheric loss from “Hot Jupiters”. *A&A*, 472: 329–334, September 2007. doi: 10.1051/0004-6361:20066929.
- B. Fegley, Jr., D. Gautier, T. Owen, and R. G. Prinn. *Spectroscopy and chemistry of the atmosphere of Uranus*, pages 147–203. IN: Uranus (A92-18701 05-91). Tucson, AZ, University of Arizona Press, 1991.

- J. Fischer, R. R. Gamache, A. Goldman, L. S. Rothman, and A. Perrin. Total internal partition sums for molecular species in the 2000 edition of the HITRAN database. *J. Quant. Spec. Radiat. Transf.*, 82:401–412, November 2003. doi: 10.1016/S0022-4073(03)00166-3.
- J. J. Fortney and W. B. Hubbard. Phase separation in giant planets: inhomogeneous evolution of Saturn. *Icarus*, 164:228–243, July 2003. doi: 10.1016/S0019-1035(03)00130-1.
- J. J. Fortney, M. S. Marley, K. Lodders, D. Saumon, and R. Freedman. Comparative Planetary Atmospheres: Models of TrES-1 and HD 209458b. *ApJ*, 627:L69–L72, July 2005. doi: 10.1086/431952.
- J. J. Fortney, M. S. Marley, and J. W. Barnes. Planetary Radii across Five Orders of Magnitude in Mass and Stellar Insolation: Application to Transits. *ApJ*, 659:1661–1672, April 2007. doi: 10.1086/512120.
- J. J. Fortney, M. Ikoma, N. Nettelmann, T. Guillot, and M. S. Marley. Self-consistent Model Atmospheres and the Cooling of the Solar System’s Giant Planets. *ApJ*, 729:32, March 2011. doi: 10.1088/0004-637X/729/1/32.
- R. S. Freedman, M. S. Marley, and K. Lodders. Line and Mean Opacities for Ultracool Dwarfs and Extrasolar Planets. *ApJS*, 174:504–513, February 2008. doi: 10.1086/521793.
- M. French, T. R. Mattsson, N. Nettelmann, and R. Redmer. Equation of state and phase diagram of water at ultrahigh pressures as in planetary interiors. *Phys. Rev. B*, 79(5):054107, February 2009. doi: 10.1103/PhysRevB.79.054107.
- D. O. Gough and N. O. Weiss. The calibration of stellar convection theories. *MNRAS*, 176:589–607, September 1976. doi: 10.1093/mnras/176.3.589.
- H. C. Graboske, Jr., R. J. Olness, J. B. Pollack, and A. S. Grossman. The structure and evolution of Jupiter - The fluid contraction stage. *ApJ*, 199:265–281, July 1975. doi: 10.1086/153689.

- O. Grasset, J. Schneider, and C. Sotin. A Study of the Accuracy of Mass-Radius Relationships for Silicate-Rich and Ice-Rich Planets up to 100 Earth Masses. *ApJ*, 693: 722–733, March 2009. doi: 10.1088/0004-637X/693/1/722.
- A. S. Grossman, H. Graboske, J. Pollack, R. Reynolds, and A. Summers. An evolutionary calculation of Jupiter. *Physics of the Earth and Planetary Interiors*, 6:91–98, 1972. doi: 10.1016/0031-9201(72)90038-6.
- T. Guillot. Condensation of Methane, Ammonia, and Water and the Inhibition of Convection in Giant Planets. *Science*, 269:1697–1699, September 1995. doi: 10.1126/science.7569896.
- T. Guillot. On the radiative equilibrium of irradiated planetary atmospheres. *A&A*, 520: A27, September 2010. doi: 10.1051/0004-6361/200913396.
- T. Guillot, G. Chabrier, D. Gautier, and P. Morel. Effect of Radiative Transport on the Evolution of Jupiter and Saturn. *ApJ*, 450:463, September 1995. doi: 10.1086/176156.
- K. E. Haisch, Jr., E. A. Lada, and C. J. Lada. Disk Frequencies and Lifetimes in Young Clusters. *ApJ*, 553:L153–L156, June 2001. doi: 10.1086/320685.
- R. Hanel, B. Conrath, F. M. Flasar, V. Kunde, W. Maguire, J. C. Pearl, J. Pirraglia, R. Samuelson, L. Herath, M. Allison, D. P. Cruikshank, D. Gautier, P. J. Gierasch, L. Horn, R. Koppany, and C. Ponnampertuma. Infrared observations of the Saturnian system from Voyager 1. *Science*, 212:192–200, April 1981. doi: 10.1126/science.212.4491.192.
- B. M. S. Hansen. On the Absorption and Redistribution of Energy in Irradiated Planets. *ApJS*, 179:484–508, December 2008. doi: 10.1086/591964.
- R. Helled, J. D. Anderson, M. Podolak, and G. Schubert. Interior Models of Uranus and Neptune. *ApJ*, 726:15, January 2011. doi: 10.1088/0004-637X/726/1/15.
- K. Heng, W. Hayek, F. Pont, and D. K. Sing. On the effects of clouds and hazes in the atmospheres of hot Jupiters: semi-analytical temperature-pressure profiles. *MNRAS*, 420:20–36, February 2012. doi: 10.1111/j.1365-2966.2011.19943.x.

- J. Hernández, L. Hartmann, T. Megeath, R. Gutermuth, J. Muzerolle, N. Calvet, A. K. Vivas, C. Briceño, L. Allen, J. Stauffer, E. Young, and G. Fazio. A Spitzer Space Telescope Study of Disks in the Young σ Orionis Cluster. *ApJ*, 662:1067–1081, June 2007. doi: 10.1086/513735.
- M. Herschel and D. Watson. Account of a Comet. By Mr. Herschel, F. R. S.; Communicated by Dr. Watson, Jun. of Bath, F. R. S. *Philosophical Transactions of the Royal Society of London Series I*, 71:492–501, 1781.
- Y. Hori and M. Ikoma. Gas giant formation with small cores triggered by envelope pollution by icy planetesimals. *MNRAS*, 416:1419–1429, September 2011. doi: 10.1111/j.1365-2966.2011.19140.x.
- W. B. Hubbard. The Jovian surface condition and cooling rate. *Icarus*, 30:305–310, February 1977. doi: 10.1016/0019-1035(77)90164-6.
- W. B. Hubbard. Comparative thermal evolution of Uranus and Neptune. *Icarus*, 35:177–181, August 1978. doi: 10.1016/0019-1035(78)90002-7.
- W. B. Hubbard and J. J. Macfarlane. Structure and evolution of Uranus and Neptune. *J. Geophys. Res.*, 85:225–234, January 1980. doi: 10.1029/JB085iB01p00225.
- W. B. Hubbard, M. Podolak, and D. J. Stevenson. The interior of Neptune. In D. P. Cruikshank, M. S. Matthews, and A. M. Schumann, editors, *Neptune and Triton*, pages 109–138, 1995.
- M. Ikoma and Y. Hori. In Situ Accretion of Hydrogen-rich Atmospheres on Short-period Super-Earths: Implications for the Kepler-11 Planets. *ApJ*, 753:66, July 2012. doi: 10.1088/0004-637X/753/1/66.
- M. Ikoma, K. Nakazawa, and H. Emori. Formation of Giant Planets: Dependences on Core Accretion Rate and Grain Opacity. *ApJ*, 537:1013–1025, July 2000. doi: 10.1086/309050.
- A. P. Ingersoll. The Runaway Greenhouse: A History of Water on Venus. *Journal of Atmospheric Sciences*, 26:1191–1198, November 1969. doi: 10.1175/1520-0469(1969)026<1191:TRGAHO>2.0.CO;2.

- N. Iro, B. Bézard, and T. Guillot. A time-dependent radiative model of HD 209458b. *A&A*, 436:719–727, June 2005. doi: 10.1051/0004-6361:20048344.
- S. R. Kane. Detectability of exoplanetary transits from radial velocity surveys. *MNRAS*, 380:1488–1496, October 2007. doi: 10.1111/j.1365-2966.2007.12144.x.
- R. Kippenhahn and A. Weigert. *Stellar Structure and Evolution*. Springer-Verlag Berlin Heidelberg New York. Also Astronomy and Astrophysics Library, 1990.
- H Komabayasi. Discrete equilibrium temperatures of a hypothetical planet with the atmosphere and the hydrosphere of one-component two-phase system under constant solar radiation. *METEOROLOGICAL SOCIETY OF JAPAN*, 45:137–139, February 1967.
- T. Kubo-Oka and K. Nakazawa. Gradual increase in the obliquity of Uranus due to tidal interaction with a hypothetical retrograde satellite. *Icarus*, 114:21–32, March 1995. doi: 10.1006/icar.1995.1040.
- M Kuntz. A new implementation of the humlicek algorithm for the calculation of the voigt profile function. *Journal of Quantitative Spectroscopy and Radiative Transfer*, 57(6):819–824, 1997.
- H. Kurokawa and S.-i. Inutsuka. On the Radius Anomaly of Hot Jupiters: Reexamination of the Possibility and Impact of Layered Convection. *ArXiv e-prints*, November 2015.
- H. Kurokawa and T. Nakamoto. Mass-loss Evolution of Close-in Exoplanets: Evaporation of Hot Jupiters and the Effect on Population. *ApJ*, 783:54, March 2014. doi: 10.1088/0004-637X/783/1/54.
- H. Lammer, N. V. Erkaev, P. Odert, K. G. Kislyakova, M. Leitzinger, and M. L. Khodachenko. Probing the blow-off criteria of hydrogen-rich ‘super-Earths’. *MNRAS*, 430:1247–1256, April 2013. doi: 10.1093/mnras/sts705.
- U. J. Le Verrier. Recherches sur les mouvements d’Uranus par U. J. Le Verrier (Beschluß). *Astronomische Nachrichten*, 25:85, November 1846.

- J. Leconte and G. Chabrier. Layered convection as the origin of Saturn's luminosity anomaly. *Nature Geoscience*, 6:347–350, May 2013. doi: 10.1038/ngeo1791.
- E. D. Lopez and J. J. Fortney. The Role of Core Mass in Controlling Evaporation: The Kepler Radius Distribution and the Kepler-36 Density Dichotomy. *ApJ*, 776:2, October 2013. doi: 10.1088/0004-637X/776/1/2.
- E. D. Lopez, J. J. Fortney, and N. Miller. How Thermal Evolution and Mass-loss Sculpt Populations of Super-Earths and Sub-Neptunes: Application to the Kepler-11 System and Beyond. *ApJ*, 761:59, December 2012. doi: 10.1088/0004-637X/761/1/59.
- S. P. Lyon and J. D. Johnson. Sesame: the los alamos national laboratory equation of state database. *Los Alamos National Laboratory, Los Alamos, NM, LA-UR-92-3407*, 1992.
- M. S. Marley and C. P. McKay. Thermal Structure of Uranus' Atmosphere. *Icarus*, 138: 268–286, April 1999. doi: 10.1006/icar.1998.6071.
- T. Matsui and Y. Abe. Impact-induced atmospheres and oceans on earth and Venus. *Nature*, 322:526–528, August 1986. doi: 10.1038/322526a0.
- M. Mayor and D. Queloz. A Jupiter-mass companion to a solar-type star. *Nature*, 378: 355–359, November 1995. doi: 10.1038/378355a0.
- G. M. Mirouh, P. Garaud, S. Stellmach, A. L. Traxler, and T. S. Wood. A New Model for Mixing by Double-diffusive Convection (Semi-convection). I. The Conditions for Layer Formation. *ApJ*, 750:61, May 2012. doi: 10.1088/0004-637X/750/1/61.
- A. Morbidelli, K. Tsiganis, K. Batygin, A. Crida, and R. Gomes. Explaining why the uranian satellites have equatorial prograde orbits despite the large planetary obliquity. *Icarus*, 219:737–740, June 2012. doi: 10.1016/j.icarus.2012.03.025.
- S. Nakajima, Y.-Y. Hayashi, and Y. Abe. A study on the 'runaway greenhouse effect' with a one-dimensional radiative-convective equilibrium model. *Journal of Atmospheric Sciences*, 49:2256–2266, December 1992. doi: 10.1175/1520-0469(1992)049<2256:ASOTGE>2.0.CO;2.

- W. J. Nellis, D. C. Hamilton, N. C. Holmes, H. B. Radousky, F. H. Ree, A. C. Mitchell, and M. Nicol. The nature of the interior of Uranus based on studies of planetary ices at high dynamic pressure. *Science*, 240:779–781, May 1988. doi: 10.1126/science.240.4853.779.
- N. Nettelmann, J. J. Fortney, U. Kramm, and R. Redmer. Thermal Evolution and Structure Models of the Transiting Super-Earth GJ 1214b. *ApJ*, 733:2, May 2011. doi: 10.1088/0004-637X/733/1/2.
- N. Nettelmann, R. Helled, J. J. Fortney, and R. Redmer. New indication for a dichotomy in the interior structure of Uranus and Neptune from the application of modified shape and rotation data. *Planet. Space Sci.*, 77:143–151, March 2013. doi: 10.1016/j.pss.2012.06.019.
- N. Nettelmann, J. J. Fortney, K. Moore, and C. Mankovich. An exploration of double diffusive convection in Jupiter as a result of hydrogen-helium phase separation. *MNRAS*, 447:3422–3441, March 2015. doi: 10.1093/mnras/stu2634.
- G. S. Orton, L. N. Fletcher, J. I. Moses, A. K. Mainzer, D. Hines, H. B. Hammel, F. J. Martin-Torres, M. Burgdorf, C. Merlet, and M. R. Line. Mid-infrared spectroscopy of Uranus from the Spitzer Infrared Spectrometer: 1. Determination of the mean temperature structure of the upper troposphere and stratosphere. *Icarus*, 243:494–513, November 2014a. doi: 10.1016/j.icarus.2014.07.010.
- G. S. Orton, J. I. Moses, L. N. Fletcher, A. K. Mainzer, D. Hines, H. B. Hammel, J. Martin-Torres, M. Burgdorf, C. Merlet, and M. R. Line. Mid-infrared spectroscopy of Uranus from the Spitzer infrared spectrometer: 2. Determination of the mean composition of the upper troposphere and stratosphere. *Icarus*, 243:471–493, November 2014b. doi: 10.1016/j.icarus.2014.07.012.
- J. E. Owen and Y. Wu. Kepler Planets: A Tale of Evaporation. *ApJ*, 775:105, October 2013. doi: 10.1088/0004-637X/775/2/105.
- J. C. Pearl and B. J. Conrath. The albedo, effective temperature, and energy balance of Neptune, as determined from Voyager data. *J. Geophys. Res.*, 96:18921, October 1991.

- M. Podolak and A. G. W. Cameron. Models of the Giant Planets. *Icarus*, 22:123–148, June 1974. doi: 10.1016/0019-1035(74)90113-4.
- M. Podolak, W. B. Hubbard, and D. J. Stevenson. *Model of Uranus' interior and magnetic field*, pages 29–61. IN: Uranus (A92-18701 05-91). Tucson, AZ, University of Arizona Press, 1991.
- J. B. Pollack, A. S. Grossman, R. Moore, and H. C. Graboske, Jr. A calculation of Saturn's gravitational contraction history. *Icarus*, 30:111–128, January 1977. doi: 10.1016/0019-1035(77)90126-9.
- J. B. Pollack, O. Hubickyj, P. Bodenheimer, J. J. Lissauer, M. Podolak, and Y. Greenzweig. Formation of the Giant Planets by Concurrent Accretion of Solids and Gas. *Icarus*, 124:62–85, November 1996. doi: 10.1006/icar.1996.0190.
- T. Radko. A mechanism for layer formation in a double-diffusive fluid. *Journal of Fluid Mechanics*, 497:365–380, December 2003. doi: 10.1017/S0022112003006785.
- Robert C Reid, John M Prausnitz, and Bruce E Poling. The properties of gases and liquids. 1987.
- I. Ribas, E. F. Guinan, M. Güdel, and M. Audard. Evolution of the Solar Activity over Time and Effects on Planetary Atmospheres. I. High-Energy Irradiances (1-1700 Å). *ApJ*, 622:680–694, March 2005. doi: 10.1086/427977.
- L. A. Rogers, P. Bodenheimer, J. J. Lissauer, and S. Seager. Formation and Structure of Low-density exo-Neptunes. *ApJ*, 738:59, September 2011. doi: 10.1088/0004-637X/738/1/59.
- E. Rosenblum, P. Garaud, A. Traxler, and S. Stellmach. Turbulent Mixing and Layer Formation in Double-diffusive Convection: Three-dimensional Numerical Simulations and Theory. *ApJ*, 731:66, April 2011. doi: 10.1088/0004-637X/731/1/66.
- L. S. Rothman, C. P. Rinsland, A. Goldman, S. T. Massie, D. P. Edwards, J.-M. Flaud, A. Perrin, C. Camy-Peyret, V. Dana, J.-Y. Mandin, J. Schroeder, A. McCann, R. R.

- Gamache, R. B. Wattson, K. Yoshino, K. Chance, K. Jucks, L. R. Brown, V. Nemtchinov, and P. Varanasi. The HITRAN Molecular Spectroscopic Database and HAWKS (HITRAN Atmospheric Workstation): 1996 Edition. *J. Quant. Spec. Radiat. Transf.*, 60:665–710, November 1998. doi: 10.1016/S0022-4073(98)00078-8.
- L. S. Rothman, I. E. Gordon, A. Barbe, D. C. Benner, P. F. Bernath, M. Birk, V. Boudon, L. R. Brown, A. Campargue, J.-P. Champion, K. Chance, L. H. Coudert, V. Dana, V. M. Devi, S. Fally, J.-M. Flaud, R. R. Gamache, A. Goldman, D. Jacquemart, I. Kleiner, N. Lacome, W. J. Lafferty, J.-Y. Mandin, S. T. Massie, S. N. Mikhailenko, C. E. Miller, N. Moazzen-Ahmadi, O. V. Naumenko, A. V. Nikitin, J. Orphal, V. I. Perevalov, A. Perrin, A. Predoi-Cross, C. P. Rinsland, M. Rotger, M. Šimečková, M. A. H. Smith, K. Sung, S. A. Tashkun, J. Tennyson, R. A. Toth, A. C. Vandaele, and J. Vander Auwera. The HITRAN 2008 molecular spectroscopic database. *J. Quant. Spec. Radiat. Transf.*, 110:533–572, June 2009. doi: 10.1016/j.jqsrt.2009.02.013.
- L. S. Rothman, I. E. Gordon, Y. Babikov, A. Barbe, D. Chris Benner, P. F. Bernath, M. Birk, L. Bizzocchi, V. Boudon, L. R. Brown, A. Campargue, K. Chance, E. A. Cohen, L. H. Coudert, V. M. Devi, B. J. Drouin, A. Fayt, J.-M. Flaud, R. R. Gamache, J. J. Harrison, J.-M. Hartmann, C. Hill, J. T. Hodges, D. Jacquemart, A. Jolly, J. Lamouroux, R. J. Le Roy, G. Li, D. A. Long, O. M. Lyulin, C. J. Mackie, S. T. Massie, S. Mikhailenko, H. S. P. Müller, O. V. Naumenko, A. V. Nikitin, J. Orphal, V. Perevalov, A. Perrin, E. R. Polovtseva, C. Richard, M. A. H. Smith, E. Starikova, K. Sung, S. Tashkun, J. Tennyson, G. C. Toon, V. G. Tyuterev, and G. Wagner. The HITRAN2012 molecular spectroscopic database. *J. Quant. Spec. Radiat. Transf.*, 130:4–50, November 2013. doi: 10.1016/j.jqsrt.2013.07.002.
- E. E. Salpeter and H. S. Zapolsky. Theoretical High-Pressure Equations of State including Correlation Energy. *Physical Review*, 158:876–886, June 1967. doi: 10.1103/PhysRev.158.876.
- A. Sánchez-Lavega, S. Pérez-Hoyos, and R. Hueso. Clouds in planetary atmospheres: A

- useful application of the Clausius-Clapeyron equation. *American Journal of Physics*, 72:767–774, June 2004. doi: 10.1119/1.1645279.
- D. Saumon, G. Chabrier, and H. M. van Horn. An Equation of State for Low-Mass Stars and Giant Planets. *ApJS*, 99:713, August 1995. doi: 10.1086/192204.
- S. Seager, M. Kuchner, C. A. Hier-Majumder, and B. Militzer. Mass-Radius Relationships for Solid Exoplanets. *ApJ*, 669:1279–1297, November 2007. doi: 10.1086/521346.
- W. L. Slattery. Giant impacts on a primitive Uranus. *Icarus*, 99:167–174, September 1992. doi: 10.1016/0019-1035(92)90180-F.
- C. Sotin, O. Grasset, and A. Mocquet. Mass radius curve for extrasolar Earth-like planets and ocean planets. *Icarus*, 191:337–351, November 2007. doi: 10.1016/j.icarus.2007.04.006.
- F. Soubiran and B. Militzer. Miscibility Calculations for Water and Hydrogen in Giant Planets. *ApJ*, 806:228, June 2015. doi: 10.1088/0004-637X/806/2/228.
- D. J. Stevenson. Interiors of the giant planets. *Annual Review of Earth and Planetary Sciences*, 10:257–295, 1982. doi: 10.1146/annurev.ea.10.050182.001353.
- D. J. Stevenson. The Uranus-Neptune Dichotomy: the Role of Giant Impacts. In *Lunar and Planetary Science Conference*, volume 17 of *Lunar and Planetary Science Conference*, pages 1011–1012, March 1986.
- O. Struve. Proposal for a project of high-precision stellar radial velocity work. *The Observatory*, 72:199–200, October 1952.
- K. Sugiyama, K. Nakajima, M. Odaka, M. Ishiwatari, K. Kuramoto, Y. Morikawa, S. Nishizawa, Y. O. Takahashi, and Y.-Y. Hayashi. Intermittent cumulonimbus activity breaking the three-layer cloud structure of Jupiter. *Geophys. Res. Lett.*, 38:L13201, July 2011. doi: 10.1029/2011GL047878.
- K. Sugiyama, K. Nakajima, M. Odaka, K. Kuramoto, and Y.-Y. Hayashi. Numerical simulations of Jupiter’s moist convection layer: Structure and dynamics in statistically steady states. *Icarus*, 229:71–91, February 2014. doi: 10.1016/j.icarus.2013.10.016.

- D. C. Swift, J. H. Eggert, D. G. Hicks, S. Hamel, K. Caspersen, E. Schwegler, G. W. Collins, N. Nettelmann, and G. J. Ackland. Mass-Radius Relationships for Exoplanets. *ApJ*, 744:59, January 2012. doi: 10.1088/0004-637X/744/1/59.
- D. Valencia, D. D. Sasselov, and R. J. O’Connell. Radius and Structure Models of the First Super-Earth Planet. *ApJ*, 656:545–551, February 2007. doi: 10.1086/509800.
- D. Valencia, M. Ikoma, T. Guillot, and N. Nettelmann. Composition and fate of short-period super-Earths. The case of CoRoT-7b. *A&A*, 516:A20, June 2010. doi: 10.1051/0004-6361/200912839.
- D. Valencia, T. Guillot, V. Parmentier, and R. S. Freedman. Bulk Composition of GJ 1214b and Other Sub-Neptune Exoplanets. *ApJ*, 775:10, September 2013. doi: 10.1088/0004-637X/775/1/10.
- A. Vazan, R. Helled, A. Kovetz, and M. Podolak. Convection and Mixing in Giant Planet Evolution. *ApJ*, 803:32, April 2015. doi: 10.1088/0004-637X/803/1/32.
- A. Vidal-Madjar, A. Lecavelier des Etangs, J.-M. Désert, G. E. Ballester, R. Ferlet, G. Hébrard, and M. Mayor. An extended upper atmosphere around the extrasolar planet HD209458b. *Nature*, 422:143–146, March 2003. doi: 10.1038/nature01448.
- P. Vinet, J. Ferrante, J. H. Rose, and J. R. Smith. Compressibility of solids. *J. Geophys. Res.*, 92:9319–9325, August 1987. doi: 10.1029/JB092iB09p09319.
- F. W. Wagner, F. Sohl, H. Hussmann, M. Grott, and H. Rauer. Interior structure models of solid exoplanets using material laws in the infinite pressure limit. *Icarus*, 214:366–376, August 2011. doi: 10.1016/j.icarus.2011.05.027.
- W. R. Ward. Density waves in the solar nebula - Differential Lindblad torque. *Icarus*, 67:164–180, July 1986. doi: 10.1016/0019-1035(86)90182-X.
- A. J. Watson, T. M. Donahue, and J. C. G. Walker. The dynamics of a rapidly escaping atmosphere - Applications to the evolution of earth and Venus. *Icarus*, 48:150–166, November 1981. doi: 10.1016/0019-1035(81)90101-9.

- L. M. Weiss, G. W. Marcy, J. F. Rowe, A. W. Howard, H. Isaacson, J. J. Fortney, N. Miller, B.-O. Demory, D. A. Fischer, E. R. Adams, A. K. Dupree, S. B. Howell, R. Kolbl, J. A. Johnson, E. P. Horch, M. E. Everett, D. C. Fabrycky, and S. Seager. The Mass of KOI-94d and a Relation for Planet Radius, Mass, and Incident Flux. *ApJ*, 768:14, May 2013. doi: 10.1088/0004-637X/768/1/14.
- H. F. Wilson and B. Militzer. Solubility of Water Ice in Metallic Hydrogen: Consequences for Core Erosion in Gas Giant Planets. *ApJ*, 745:54, January 2012. doi: 10.1088/0004-637X/745/1/54.
- T. S. Wood, P. Garaud, and S. Stellmach. A New Model for Mixing by Double-diffusive Convection (Semi-convection). II. The Transport of Heat and Composition through Layers. *ApJ*, 768:157, May 2013. doi: 10.1088/0004-637X/768/2/157.
- J. T. Wright, O. Fakhouri, G. W. Marcy, E. Han, Y. Feng, J. A. Johnson, A. W. Howard, D. A. Fischer, J. A. Valenti, J. Anderson, and N. Piskunov. The Exoplanet Orbit Database. *PASP*, 123:412–422, April 2011. doi: 10.1086/659427.
- R. Yelle, H. Lammer, and W.-H. Ip. Aeronomy of Extra-Solar Giant Planets. *Space Sci. Rev.*, 139:437–451, August 2008. doi: 10.1007/s11214-008-9420-6.
- H. S. Zepolsky and E. E. Salpeter. The Mass-Radius Relation for Cold Spheres of Low Mass. *ApJ*, 158:809, November 1969. doi: 10.1086/150240.